공학박사 학위논문

Improvement of Low Energy Beam Transport in High Intensity Proton Injector

고출력 양성자 입사기에서 저에너지 빔 수송 향상에 관한 연구

2021년 8월

서울대학교 대학원

에너지시스템공학부

김 동 환

Improvement of Low Energy Beam Transport in High Intensity Proton Injector

지도 교수 황 용 석

이 논문을 공학박사 학위논문으로 제출함
2021년 8월

서울대학교 대학원
에너지시스템공학부
김 동 환

김동환의 공학박사 학위논문을 인준함
2021년 8월

위 원 장 정 경 재

부위원장 황 용 석

위 원 나 용 수

위 원 김 기 현

위 원 김 한 성

Abstract

Improvement of Low Energy Beam Transport in High Intensity Proton Injector

Dong-Hwan Kim

Department of Energy System Engineering

The Graduate School

Seoul National University

A proton injector is the key element of a high current beam and high-performance fast neutron sources for basic science and future energy resources. The proton injector in the study transports a high-current and low-energy proton beam with minimum loss and makes the beam parameters matched to a subsequent accelerator such as radio-frequency quadrupole.

A high-current proton beam contains strong space charge effect and non-linear electric field, increasing beam size and emittance during transport. To reduce the beam size, solenoid focusing lens is used, which rather causes spherical aberration and another emittance growth. In addition, the presence of such an electromagnetic element gives rise to alignment error. Solenoid magnet makes it difficult to control a position of beam centroid since it has characteristics of rotating and coupling the beam in the transverse plane.

This study has established a proton injector test stand and introduced novel techniques to improve the low energy beam transport in a high-intensity proton injector. Proton injector test stand includes transverse beam profile monitor, which is composed of a scintillation screen and a CCD camera, to measure the position, size, and emittance of the beam. Two key factors for improving low-energy beam transport are low beam emittance and a fast and accurate beam tuning method. For this purpose, a residual gas molecule analysis method and an artificial neural network (ANN) model are introduced.

As a first result, low beam emittance was measured by preventing beam emittance from growing through an inert gas injection technique based on numerical analysis on steady-state pressure in high vacuum condition. A space charge potential increases beam emittance, not preserving the intrinsic emittance at the beam extraction region. One of the natural processes to cancel space charge force is that proton beam collides with residual gases mainly composed of hydrogen molecules flowing out of ion source and air molecules, causing some ionization. It is a self-neutralization that the generated electrons are trapped in the space charge potential of the beam. It is known to be more effective as the number of residual gas molecules in the transport pipe increases and the heavier inert gas molecules are involved since they generally have larger collisional cross-section. Suppression of emittance growth is achieved and beam emittance is decreased up to 23% through the residual gas injection.

Artificial neural network (ANN) model can greatly reduce time and increase accuracy in low energy beam tuning. There are unknowns such as alignment errors that are difficult to measure between elements involved in the beam transport process, such as beam extraction, focusing, and

deflection. To correct for these errors, steering magnets control the beam centroid in the transverse plane. In order to optimize the beam transport, it is necessary to observe the change of beam centroid and size for various magnet settings. Multi-layer perceptron model is utilized to interpret this nonlinear relationship and to control the beam properly based on the measured data. Extensive beam dynamics simulations are performed to verify the efficient training and the practicality of the predictive model. The output results of calculating the beam size and beam position at a specific location are obtained according to various sources of errors and unknowns that may occur in the LEBT. It is confirmed that the predictive model with high accuracy can be derived from sufficient measurement data, and it is applied to actual beam diagnosis and beam control experiments. The ANN model developed in this study shows more accurate prediction at a speed 49 times faster than the existing scan method.

This study contributed to the suppression of the beam emittance growth and the development of a fast and accurate beam transport control technique in high intensity proton injector. This can be applied to the evaluation and improvement of beam emittance in beamlines under various conditions by increasing the utility of beam diagnostic data. In addition, there is a possibility to greatly improve beam tuning efficiency to higher energy sections and beamlines that have more control variables and are more complex than low-energy beam transport systems. Ultimately, the study can be developed as a base technology for autonomous operation of accelerator with minimum human intervention.

Keywords: Proton Injector, Low Energy Beam Transport, Beam Emittance, Self-Neutralization, Beam Tuning, Artificial Neural Network

Student Number:2015-21312

Contents

List of Tables

List of Figures

Chapter 1. Introduction

1.1. High Intensity Proton Injector

Over the last decade, the interest of the international scientific community for high power light ion accelerators increased significantly. Especially, a high-power proton accelerator is considered as a good driver for a high-performance neutron source based on well-established technology and continuous operability [1]. A proton injector is an important foundation to obtain high current beam. Proton injector in the low energy section consists of an ion source, electrodes for a beam formation, and a low energy beam transport (LEBT) before the subsequent accelerator – generally a radio frequency quadrupole (RFQ). It is necessary to optimize beam transport that satisfies the beam parameters that a RFQ requires, by controlling the size and trajectories of the beam. Microwave ion source is the most commonly used because it has an advantage in lifespan due to its cathode-less characteristic. As the beam formation or beam extraction part, a three-electrode system with an acceleration-deceleration electric field structure is used. In KOMAC, since 50 kV beam is extracted with fixed the electric field distribution, the plasma properties in the ion extraction region should be optimized to satisfy the best beam optics. The low energy beam transport (LEBT) part is responsible for beam transport after the extraction system, and consists of a beam focusing lens and a steerer that deflects the path of the beam. In order to control the beam transport in the LEBT, useful diagnostics and tuning method are essential. Beam diagnostic system consists of a beam current monitor that can measure the beam intensity in real time, and a beam profile monitor that measures the center coordinate and size of the beam. Beam emittance can be calculated by solenoid scan and lens approximation based on the solenoid magnet and the beam profile

monitor.

In a high current accelerator, a space charge has a great effect on beam transport characteristics in proportion to a beam current density. The space charge effect is more significant in low energy region than in relativistic energy region, where the increased magnetic attraction partially compensates the electric repulsion between charges in the beam. In the magnetostatic low ene0072gy beam transport system that uses only magnetic focusing elements, space charge is naturally neutralized by a beam-to-neutral ionizing collision. It is well known that higher gas pressure more increases the extent of neutralization and typical residual gas injection scheme has been widely applied. Remarkable works are dedicated to calculate space charge potential using particle-in-cell code such as CARTAGO and SolMaxP [2, 3]. However, this space charge potential map is generally difficult to obtain and to compare with experiments. This study pays attention to the fact that the self-neutralization is essentially originated from the residual gases. In high vacuum condition, residual gases behave in molecular flow, which is close to random motion. The Monte-Carlo analysis is numerical method to simulate random motion of each particle. To analyze gas molecules and optimize the injection, residual gas molecules are numerically simulated to produce three-dimensional distribution of gas pressure which is corrected by measured pressures in multiple points of the beamline. This approach helps to understand residual gas injection and to improve beam transport by mitigating emittance growth caused by space charge effect.

Beam transport can also be largely affected by a misalignment and surface condition of ion source, especially after long term interruption of the operation for regular maintenance or repair of the ion source. This non-linear complex system requires frequent tuning and optimization of the operating parameters, which can be time-consuming and tedious process.

Therefore, it is necessary to study the beam dynamics for the control of beam transport with a beam diagnostics data. Artificial neural networks (ANN) are suited to deal with a myriad of complex and time-varying data - such as control variables and diagnostics data - produced in an accelerator [4].

Proton injector test stand has been built to experimentally study and to ultimately improve low energy beam transport in the two major aspects; mitigation of beam emittance growth based on numerical analysis of gas molecules and fast beam tuning based on artificial neural network model as machine learning technique. The injector consists of a microwave discharge ion source, low energy beam transport (LEBT) system, and beam diagnostics. The ion source extraction system can generate 50-keV proton beam with maximum current of 30 mA. The LEBT section is composed of a dipole magnet for a 90° bending with edge focusing, two solenoid magnets for the beam focusing, and two steering magnets for the beam orbit correction. Focusing lenses are utilized to prevent a beam from striking a wall and to make matched beam parameters downstream. In addition, several steerers are used to correct alignment errors that inevitably exist between the beam-line components involved in the transport process. Beam diagnostics system includes two beam current monitors, a faraday cup, a beam profile monitor based on a scintillator. These devices are used to evaluate a transmission through a beamline and to measure center position and size of beam at certain longitudinal location. This study presents the numerical analysis and experimental evidence to comprehend and improve the low energy beam transport.

1.2. Applications of High Intensity Proton Injector

High intensity proton injector serves as the starting point for a high-power proton accelerator and a neutron source. High-intensity neutron source is mainly based on nuclear spallation reaction between proton beam and heavy metal target. One existing application is fundamental sciences and technologies using neutron scattering which quite requires high intensity. Another promising application is a development of subcritical system. This accelerator-driven subcritical system has the advantage of inherent safety among future nuclear energy system, and is of great research value because it can dramatically reduce the amount of long-lived actinides that cause safety risks at the disposal of nuclear waste.

High-intensity neutron source can specifically be based on nuclear fusion reaction to study fusion materials that remain technical challenges in the field of nuclear fusion. This neutron source requires relatively lower beam energy than the one based on spallation reaction. Instead, deuteron or triton which is isotope of proton, is chosen as a source of particle beam for preferred nuclear reaction.

Finally, high intensity proton injector can be used in testing facilities to evaluate radiation-induced impact, such as soft single event effects, on semiconductors by cosmic radiation.

1.2.1. High-intensity neutron source

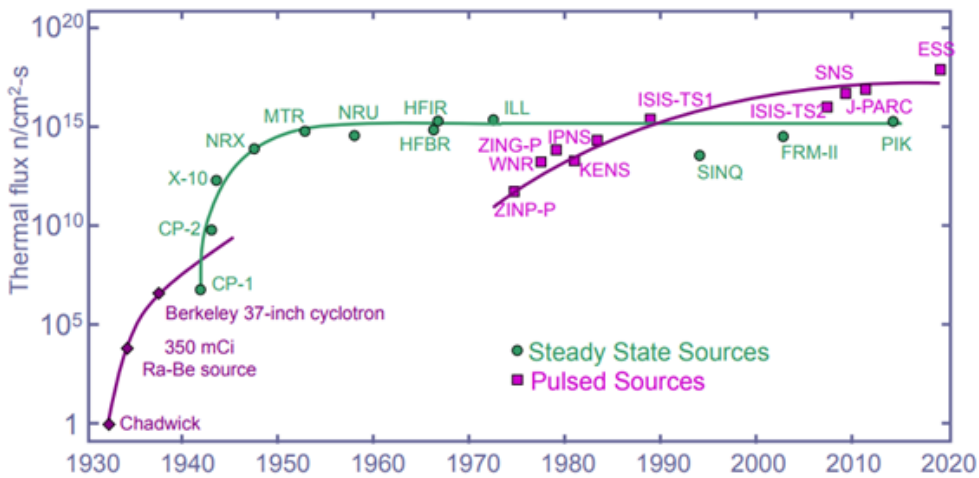

Figure 1. 1. Development history of worldwide neutron sources.

Existing high-intensity spallation neutron source facilities include SNS in the US, J-PARC in Japan. Spallation Neutron Source (SNS) of Oak Ridge National Laboratory (ORNL), the largest source of spallation neutrons in existence, has a maximum proton beam power of 1.44 MW. It has a target structure that circulates liquid mercury in an iron container for cooling efficiency. The second largest scale is a joint project of Japan's KEK and JAEA, which is a J-PARC facility operated in the Tokai area. The J-PARC combines a 400 MeV linear accelerator with Rapid Cycling Synchrotron (RCS), a type of 3 GeV synchrotron, to show a maximum power of 0.5 MW as a spallation neutron source.

The concept of an accelerated-driven subcritical reactor (ADSR) was proposed by Lawrence in the 1960s. The European Technical Working Group in Europe evaluated the ADS technology and recommendations for experiments using ADS [1]. In 2002, based on this, OECD/NEA published a report entitled “Accelerator Driven Systems (ADS) and Fast Reactors (FR) in Advanced Nuclear Fuel Cycles”. And in Europe, like ATW in the United States, Carlo Rubbia has chosen an additional goal of producing energy

using nuclear waste as reusable fuel through fission, not just for nuclear transmutation of the waste. In order to meet this purpose, the proposed ADSR is called Energy Amplifier (EA).

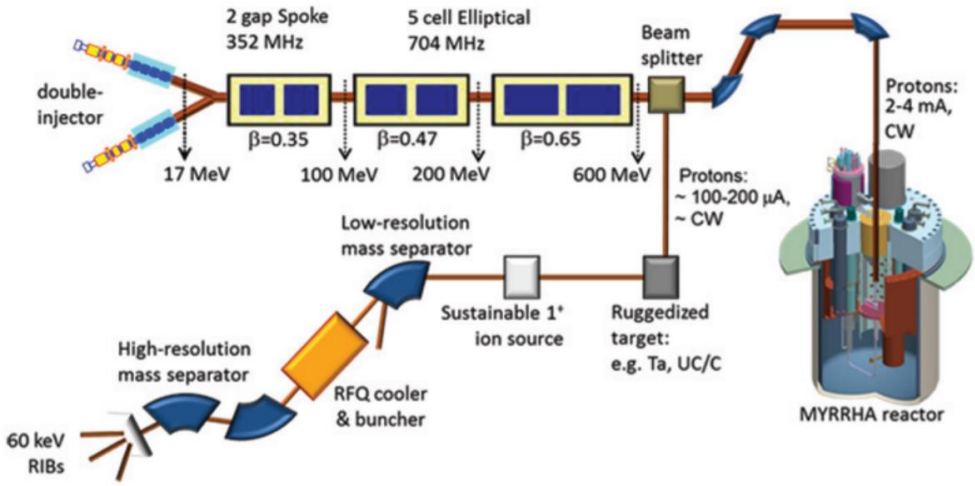

Figure 1. 2. Overview of MYRRHA project [6].

Although various basic tests have been conducted on high-intensity neutron sources to drive subcritical system around the world, it is necessary to demonstrate and to prove engineering design that has increased the facility scale for commercialization. High-intensity neutron sources for this consideration include ESS and MYRRHA project currently under development in Europe. The European Spallation Source (ESS), which is being built in Sweden as a joint European project, is targeting a beam output of up to 5 MW with a 2 GeV proton linear accelerator. The European MYRRHA project requires a proton accelerator with a stable beam current of 600 MeV and 4 mA for subcritical operation with a multiplication factor of 0.95 in a reactor core. The MYRRHA project is the only ADSR system in the world that is currently scheduled for research/development and construction [5, 6].

1.2.2. Fusion neutron irradiation and test facility on fusion materials

Accelerator-based fast neutron sources with nuclear reaction have a principle that irradiate a proton beam or deuteron beam to a target composed of a single light element such as a deuterium, a lithium, and a beryllium. These fusion-relevant neutron sources may be useful according to their size and applications. Portable neutron generator is suitable for on-site neutron radiography or activation analysis with its small size. Productions of radio-isotope or nuclear data and boron-neutron capture therapy are other applications which require higher intensity than the portable one. Finally, this is very large scale to study radiation hardness of materials in a harsh radiation environment.

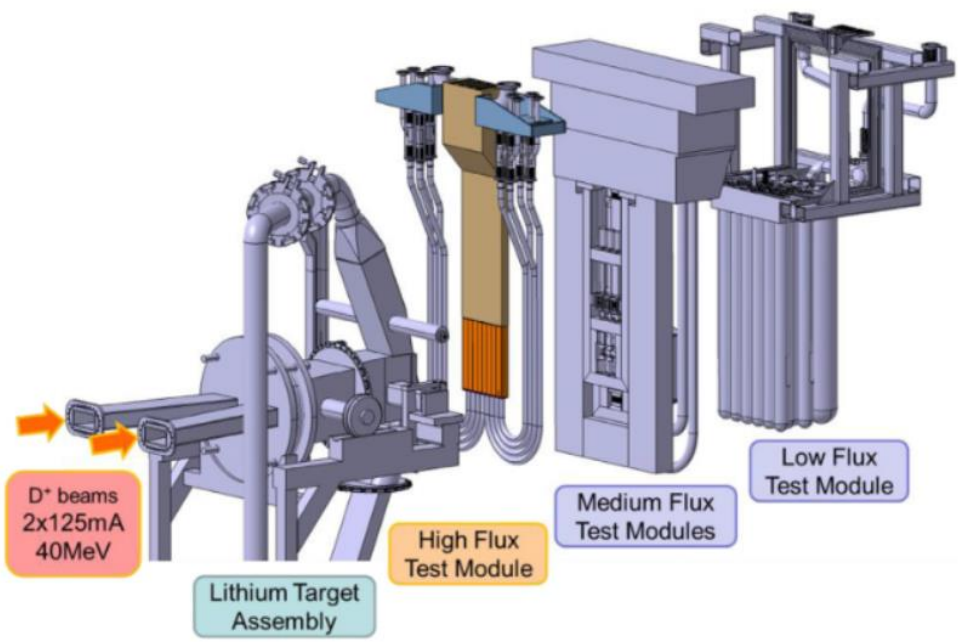

Figure 1. 3. International Fusion Material Irradiation Facility (IFMIF) [7].

High intensity proton injector is related to the latter application to study fusion materials that remain technical challenges in the field of

nuclear fusion. International Fusion Material Irradiation Facility (IFMIF) is part of a project to test fusion materials in extreme radiation environments which will be very high-flux fast neutron and gamma fields such as ITER, DEMO, and fusion power plant in the future. European Union and Japan are intimately involved in the project. The Engineering Validation and Engineering Design Activities (EVEDA) phase of the IFMIF project try to build the test facility corresponding to the level of $10^{18} n/m^2 s$, which is expected as 14 MeV neutron flux at the primary inner wall of DEMO, by irradiating a two 40 MeV and 125 mA deuteron beams onto a liquid lithium target [7].

1.2.3. Facility for testing the radiation effect of protons and neutrons on electronics.

As the operating voltages and dimensions of semiconductor-based electronics decrease in order to meet consumer demand for higher density, functionality, and lower power, their sensitivity to radiation is rapidly increasing [8]. The phenomenon that the commercial semiconductor industry wants to quantitatively evaluate and cope with is soft single-event effects (SEEs), and is abbreviated to soft error. Soft single-event effects mean that data states of memory cell, flip-flop or register are reversed or flipped. It is "soft" because it does not permanently damage the circuit or the device itself. Background radiation sources that affect semiconductors can be broadly divided into two sources, similar to the classification of “internal exposure” and “external exposure” as sources of radiation effects on living organisms. One corresponds to internal exposure, in the case that a trace amount of alpha particle emitters such as uranium and thorium present in the crust are added as impurities to the packaging material of the semiconductor.

These radioactive nuclides usually emit alpha particles of from 2 to

9 MeV, and their range is very short, so they can cause errors in semiconductors as a mechanism to transfer all kinetic energy to electrons in the path. This effect has been somewhat mitigated by the efforts of manufacturers and vendors to purify materials that are in close proximity of the integrated circuit (IC). If this ultra low alpha (ULA) material emits alpha particles below (0.001 alpha/h cm^2), it is estimated that this effect can be reduced to less than 20% in most cases. Other sources of radiation are cosmic ray incident on the Earth from the sun or space [8].

Cosmic radiation refers to radiation incident on the Earth from the sun or space. It is classified into galactic cosmic-ray (GCR) flying from outside the solar system such as a supernova explosion and solar cosmic radiation (SCR) caused by the sun's sunspot activity. In GCR, about 85% of protons, 12.5% of alpha particles, and the rest are composed of all kinds of nuclei and electrons. These protons are released from the sun and trapped in Van Allen Belts on the way to Earth by the Earth’s magnetic field. They threaten satellites including low earth orbit (LEO) satellites.

Soft errors are caused by high-energy particles such as solar protons and trapped protons in the magnetic field. They lead to deterioration of device performance, operation errors, data loss, or permanent breakdown. The primary cosmic radiation that reaches the atmosphere through a magnetic field reacts with oxygen, nitrogen, and argon constituting the atmosphere to generate secondary cosmic radiation, including pions, protons, neutrons, muons, electrons, and photons having an energy of hundreds of MeV or more. The dose rate of these secondary cosmic radiation decreases as the depth increases due to the shielding effect by air, and becomes insignificant at the ground level. At a flight level where the dose rate is much higher than the ground, secondary particles are mostly composed of neutrons and can induce SEE in avionics systems. SEE generated by atmospheric neutrons has become a major threat to the high reliability

requirements of aircraft electronics, and has been strongly required to be tested in accelerator-based facility.

As mentioned in the first paragraph, the SEE has begun to be serious concern not only at a flight level, but also in ground-based electronic devices. At sea level, there are a variety of electronic components that play an important role, from large power electronics to microelectronic devices embedded in sophisticated systems such as automotive electronic devices and medical equipment such as pacemakers.

Soft error rate (SER) can be fast estimated, and it is often called accelerated SER (ASER) test. The device in the ASER test is exposed to a specific radiation source that is much higher in intensity than the ambient radiation level that normally occurs, and it takes less time to obtain useful data. The downside of ASER is that the results require trend extrapolation of the conditions of use, and several different radiation sources must be used to account for the soft errors caused by both alpha particles and cosmic neutrons [8].

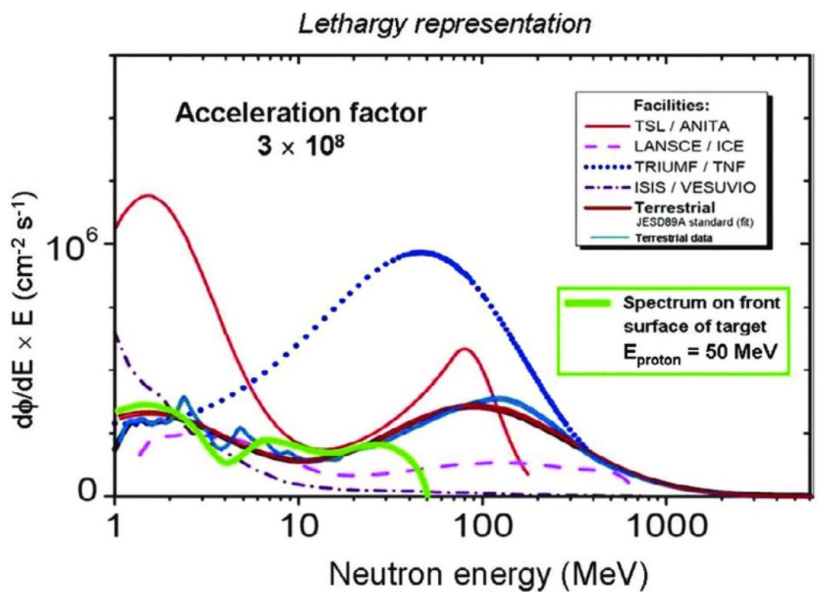

Figure 1. 4. Neutron energy spectra of the international neutron source facilities and terrestrial source [9, 10].

The TRIUMF is representative facility to serve ASER test with spallation neutrons generated from a proton beam of 520 MeV [11]. It is being used most actively to test soft errors caused by cosmic radiation. The other facilities are Ice House of LANSCE (Los Alamos Neutron Science Center) in the United State, ANITA in Sweden, ISIS in the United Kingdom, and RCNP in Japan. As shown Figure 1.4, these facilities similarly imitate the neutron spectrum like cosmic-ray-induced neutrons by properly designing shields and reflectors to be placed around the target [9, 10]. Acceleration factor represents how fast ASER test is to be performed. It is generally determined by proton beam specifications and target systems. In this context, performance of proton injector is a crucial factor for higher efficiency and capacity of the test.

1.3. Previous Work and Research Motivation

Table 1.1. Comparison: space charge model and emittance measurement.

	This study	IFMIF-LIPAc,
Space charge Model	Steady-state model with a realistic gas pressure distribution.	Dynamic model with a homogeneous gas pressure value.
Diagnostics	Scintillating screen Solenoid scan	Allison Scanner

Residual gases are typically used to enhance space charge compensation in magnetostatic LEBTs. When residual gas molecules are heavier and higher in pressure, the compensation increases and this effect has been validated in several high-intensity accelerators [3, 12-14]. Injector teams in ESS and IFMIF are dedicated to calculate space charge potential as

Figure 1.5 using particle-in-cell code such as CARTAGO and SolMaxP [3, 12]. However, this space charge potential map is difficult to obtain and to compare with direct measurement.

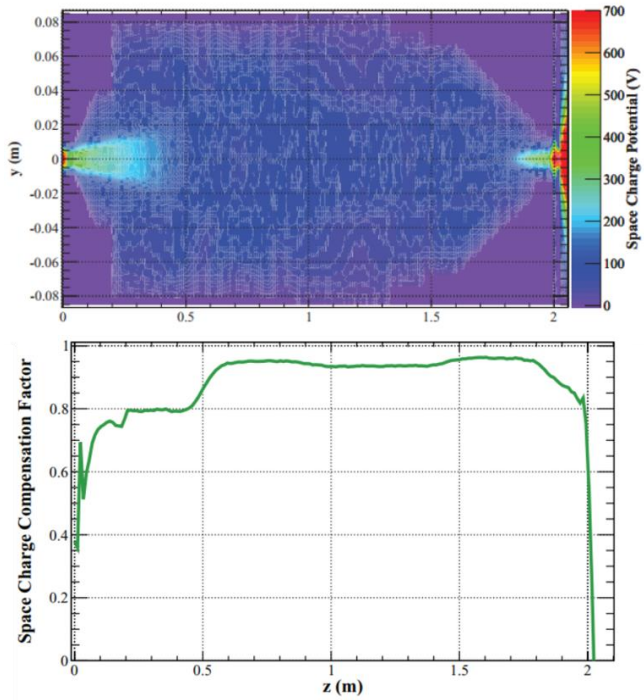

Figure 1. 5. Space charge potential map calculated by PIC method - SolMaxP and space charge compensation map [12].

Space charge and its neutralization should be quantified to study suppression of emittance growth and realistic beam transport with the support of space charge model and diagnostic data. Previous studies have critical limitation of assuming homogeneous gas pressure in the beamline, causing discrepancy between actual behavior and simulation of beam. Monte-Carlo analysis on gas molecules can improve space charge neutralization model with realistic steady-state pressure distribution.

The objectives of previous works in the KOMAC are to characterize and improve the proton injector [18, 19]. An Allison-type emittance scanner

had been installed and utilized to investigate transverse beam emittance and Twiss parameter. Operating parameters has been studied in Duoplasmatron ion source and low energy beam transport system. The study dedicated to reveal the dependency of on arc current and background gas pressure on beam emittance [18, 19]. The measurement data roughly shows time transient characteristics of the beam emittance. However, neutralization time which is very short as tens of microsecond was not measured because of the limited number of time step. Also, this scanner is disadvantage of taking a long time to get data, so that alternative beam diagnostics needs to be investigated.

Table 1.2. Comparison: low energy beam tuning method.

This study	MYYRHA
ANN model by beam profile data with operating conditions	ANN model by beam current data
Other studies on proton injectors	
Parametric Scan	

In the issue of beam tuning, Artificial neural network (ANN) has ability of fast response to overcome the inefficiency of traditional tuning method in low energy beam transport (LEBT). Optics correction has been actively studied in ring accelerators [15]. Automation of collimator alignment at Large Hadron Collider has shown saving human resources during the machine operation [16]. In the field of high intensity injector for linear accelerator, the MYRRHA injector and its machine learning (ML) model has been simultaneously developed to optimize the beam matching

between ion source, the low energy beam transport, and 176 MHz 4-rod radio-frequency quadrupole in MYRRHA project [17]. The ML models have shown reconstruction of LEBT scan parameters, but the parameter spaces are limited since ion source parameters are not yet introduced in the model [17]. Machine learning model from beam profile data can demonstrate flexible usability to optimize beam parameters, not just beam current.

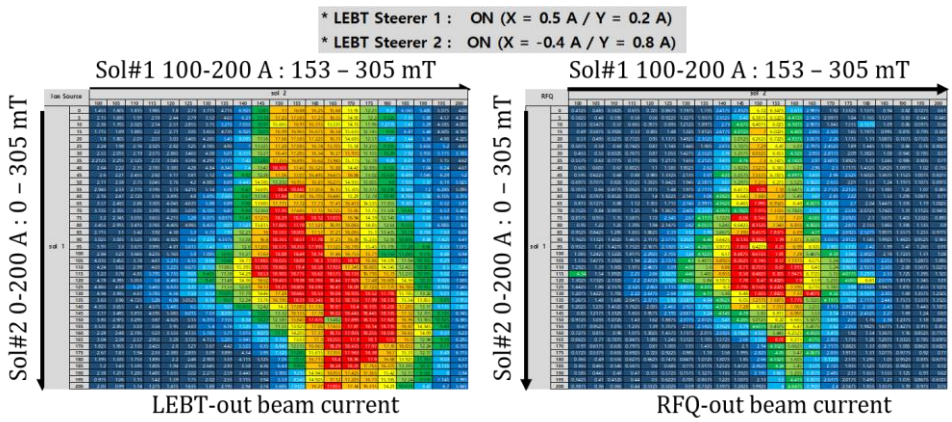

Figure 1. 6. Parametric scan of the LEBT solenoids in KOMAC.

In terms of optimization of magnetic elements in the KOMAC injector, parametric scans have been repeated as shown in Figure 1.6. whenever injector condition changes by a plasma stability or maintenance. This scanning method is time-consuming and the optimizing results are also limited due to the lack of time.

1.4. Contribution and Scope of the Study

This study focuses on suppression of emittance growth and fast tuning methods to improve the performance of proton injectors. Figure 1.7 shows the time structure of pulsed beam in proton injector and linear accelerator. The beam first generated from the proton injector is accelerated

to high energy through radio-frequency quadrupole (RFQ) and drift tube linac (DTL), and in the process, beam current decreases due to beam loss and mismatch caused by emittance growth.

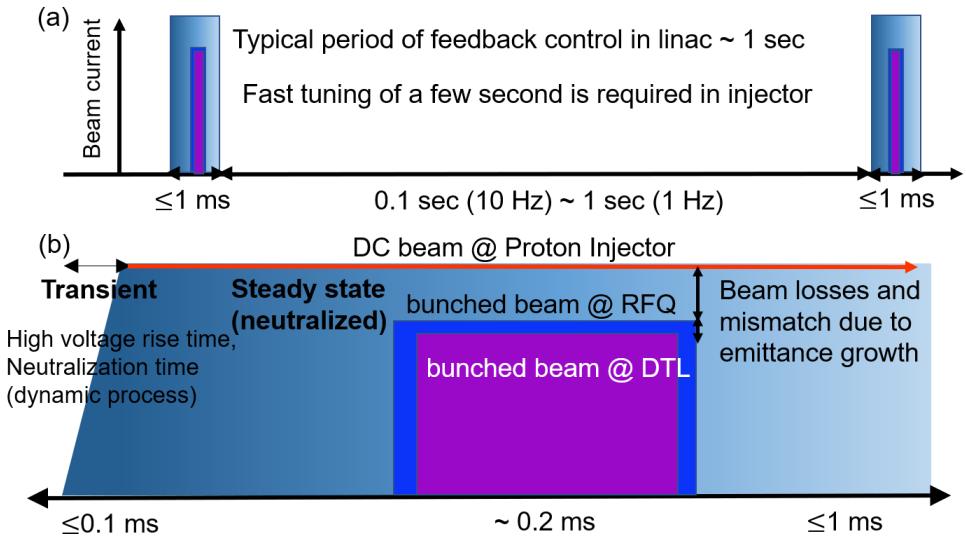

Figure 1. 7. Time structure of pulsed beam in proton injector and proton linear accelerator.

For the improvement of emittance, special attention is paid to the fact that the self-neutralization is essentially originated from the residual gases. In high vacuum condition, residual gases behave in molecular flow, which is close to random motion. The Monte-Carlo analysis is numerical method to simulate random motion of each particle. To analyze gas molecules and optimize the injection, residual gas molecules are numerically simulated to produce distribution of gas pressure which is compared with measured pressures in multiple points of the beamline. The neuralization factor is calculated with steady-state space charge model with gas density distribution and beam dynamics simulation data. It is an approach that greatly improves the previous works [12] of calculating self-neutralization by assuming a single gas pressure. Since proton injector

delivers a long pulse beam or a DC beam into a subsequent RF accelerator, a steady state is generally assumed. The emittance growth is estimated by further beam dynamics simulation and compared to emittance measurements.

According to Figure 1.7 (a), the RF linear accelerator operates at a repetition rate of several Hz to several tens of Hz. It is common to perform feedback control in units of 1 second or less. For example, the resonance cooling control system feedback control the RF resonance frequency through valve opening at 1 second intervals. Similarly, if the operating parameters of the proton injector can be tuned quickly, it will achieve a fast optimization scenario according to the feedback control cycle in the entire accelerator and become a stepping stone for accelerator autonomous operation.

A traditional tuning method for low energy beam matching is parametric scan depending on beam current and its transmission ratio. Artificial neural networks (ANN) or deep learning enables an efficient and systematic beam tuning with the help of previously accumulated data. In this study, to create and apply an ANN model for fast and accurate tuning of a proton injector, beam dynamics-based simulation data and useful measurement data are generated. They are labeled output in form of beam size and beam position changed with various operating conditions and errors as input. The performance of ANN model is compared with the parametric scan method in terms of accuracy and tuning speed.

A proton injector test stand is established and a useful beam diagnostic system is introduced to experimentally study techniques for improving the low energy beam transport in high-power proton injectors. The beam emittance and beam tuning performance are selected as evaluation index. Self-neutralization regime and ANN model are introduced respectively to improve the low energy beam transport. Beam profile monitor using a scintillation plate and a CCD camera is applied to measure

the position and size of the beam. The transverse beam emittance is estimated by analyzing the change in the beam size according to the solenoid scan.

Chapter 2. Theoretical Background

2.1. Ion Source for High-Intensity Proton Injector

2.1.1. Duoplasmatron

The duoplasmatron ion source is capable to produce negatively and/or multiply charged ion beams with high current and good beam quality in compact size. The disadvantages are a complicated structure and frequent replacement of filament which has limited lifetime. The unoplasmatron ion source had been first developed, and it was upgraded as the duoplasmatron consisting of two plasma regions by Manfred von Ardenne [20].

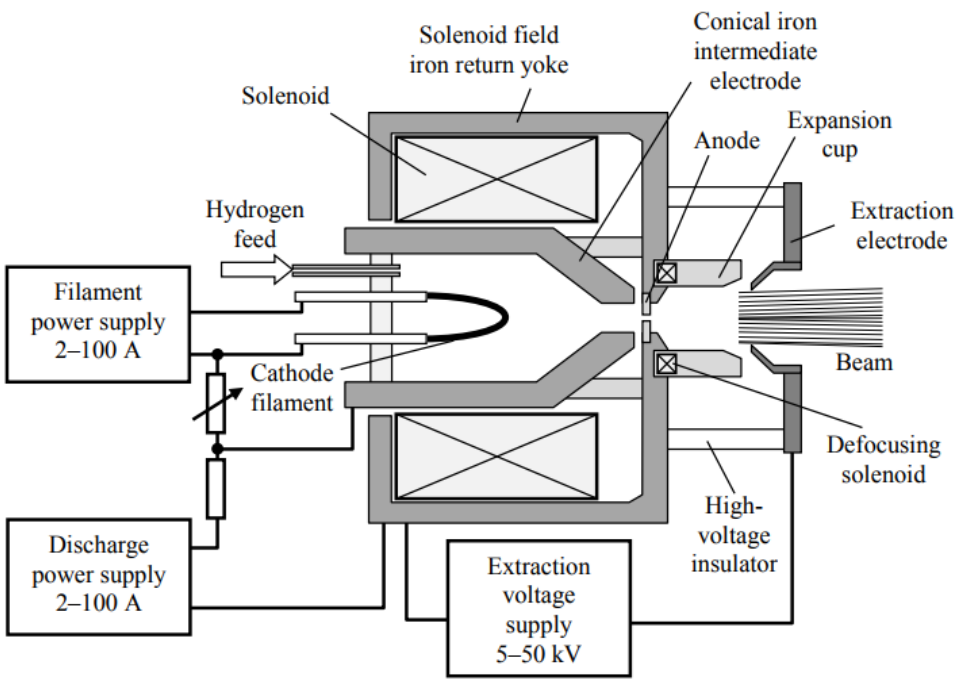

Figure 2. 1. A schematic diagram of a duoplasmatron [21].

The duoplasmatron source generally consists of five electrodes – cathode (filament wire or hollow cylinder), intermediate electrode, anode (with or without expansion cup), extraction electrode, and ground electrode–

as shown in Figure 2.1. An intermediate electrode (IE) is a key element to produce discharge as well as a unique feature positioned between cathode and anode. It has conical shape and a center bore of a few millimeters in diameter and length [Handbook of ion source]. Plasma regions are divided into low-density cathode plasma and high-density anode plasma based on the intermediate electrode. Ion beam is extracted through the anode in the high-density region, and expansion cup is normally utilized to reduce plasma density for good ion beam optics.

The cathode is a filament wire or hollow cylinder made of a tantalum or tungsten in cases where the ion source runs with oxygen or corrosive gases. For proton or negative hydrogen ion sources, oxide cathodes are used for relatively long lifetime and high currents than metal cathodes [22].

The duoPIGatron is an improvement of the duoplasmatron with an additional reflector electrode located between the anode and extraction electrode. The reflector electrode has nearly the same potential with the cathode and energetic electrons created in cathode plasma are partially trapped by axial magnetic field and electrostatic mirror effect between the electrodes. It borrows the principle of the penning ion gauge (PIG) discharge that can produce a dense plasma. The duoPIGatron was proven to produce high proton beam with small emittance at high extraction voltage of 100-keV. The multi-aperture duoPIGatron developed by Arbique produce multi-beamlet proton beam of up to 90 mA [23]. This ion source provides high currents with modest proton fraction of 30-40%, which requires dipole magnets to select proton beam and to remove unwanted species.

2.1.2. Electron Beam Ion Sources (EBIS)

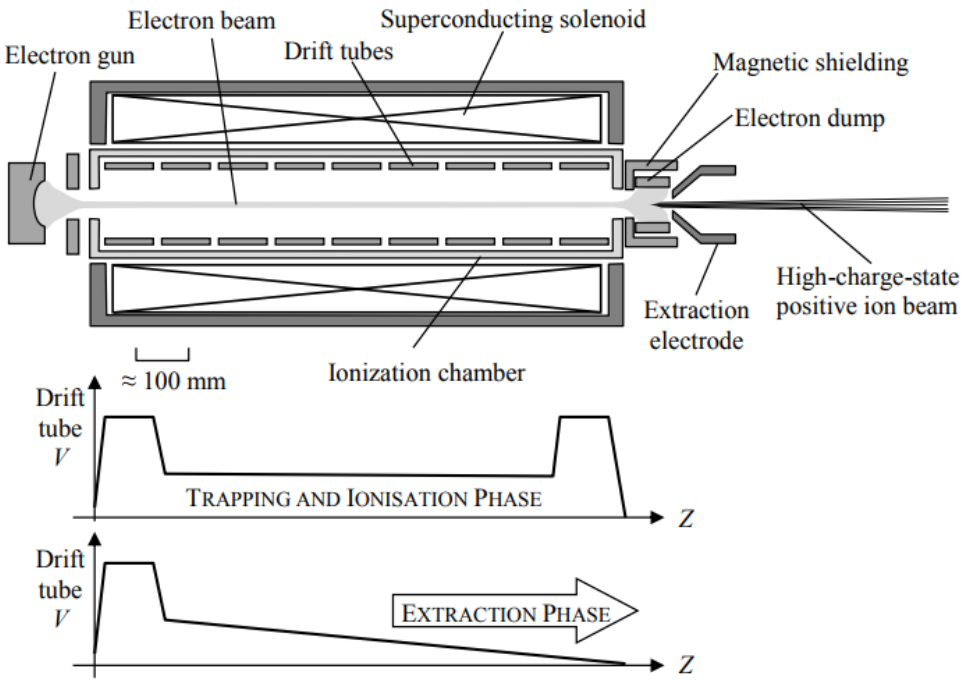

Figure 2. 2. A schematic diagram of electron beam ion source [21]

Electron beam ion source (EBIS) uses very dense electron beam to make plasmas. The EBIS has the merit to produce positive ion beams with very high charge state despite a short pulse beam. Operation principle starts with electron gun that can produce a 1 keV to 20 keV electron beam with very high current density of the order of $1000\ \mathrm{A \cdot cm^{-2}}$. The electron beam passes and highly compressed through a set of drift tubes in a 1-5 T magnetic field formed by a superconducting solenoid [21].

In the process, the strong space charge of the electron beam creates a deep potential well that can trap positive ions pulsed into ionization chamber or injected by another ion source. In terms of voltage applied in the series of drift tubes, there are two phases to make a beam highly charged and extract the beam as expressed in Figure 2.2. During the trapping and

successive ionization phase, greater positive voltages are applied to both ends of drift tubes for the longitudinal confinement of the ions. After reaching the required charge state, the electric potential distribution changes to extract beam outward [21].

The major operating variables are a trapping time, current density of electron beam, electron beam energy and a length of trap. Total charge of multiply charged ion is mostly proportional to current density of electron beam and confinement time.

2.1.3 Microwave Ion source (MWIS)

Instead of a cold cathode discharge, a microwave discharge is generated and delivers a high electron current for the main discharge. The microwave generators for the usual frequency of 2.45 GHz are easy to build from parts from microwave ovens and low in cost. Because the microwave antennas or windows can be made from a wide variety of materials, corrosion can be kept low and the microwave cathode lifetime is high.

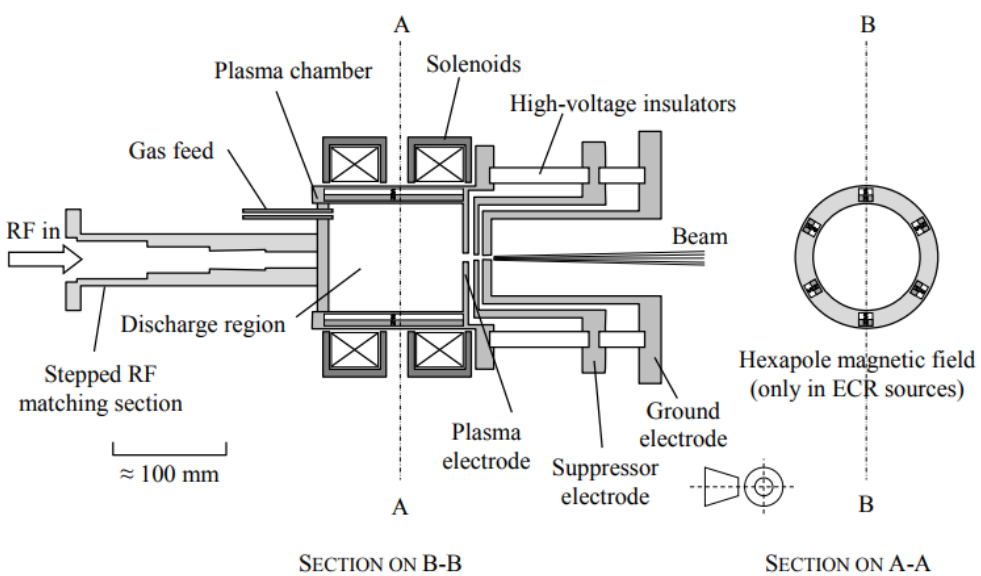

Figure 2. 3. A schematic diagram of microwave ion source [21].

The Microwave ion source (MWIS) has the advantage of a stable operation with a few beam current modulation, production of a high-current low-emittance beam and a high monoatomic fraction of ion beam. The MWIS are distinguished from RF ion sources by the fact that the wavelengths are comparable to or smaller than plasma chambers while wavelengths of RF ion source are larger. The alternating electric field of microwave is synchronous with the gyration frequency of the free electrons, and increases kinetic energy of the electrons. The MWIS can be classified into two types – electron cyclotron resonance (ECR) operation and off-resonance operation – according to operational conditions or purpose of application [24].

In the ECR operation mode, the ion source is operated at the lower pressure than off-resonance mode. The low gas pressure is necessary so that electrons can be less collided with ions and neutrals, and more heated in the ECR zone. These energetic electrons can lead ions and neutral to higher charge states via step-by-step or multiple ionization. Based on this principle, a production of multiply charged ion beam can be achieved by the ECR operation with low gas pressure and modest magnetic field to form resonance condition in a plasma chamber. A number of ion sources to apply the principle of electron cyclotron resonance have been designed and developed at the higher frequency of 14, 18 and up to 30 GHz than 2.45 GHz microwave [25].

In the off-resonance operation mode, the ion source is operated at a higher pressure and a higher magnetic field than the ECR mode. According to plasma theory on microwave discharge in magnetic fields, the right-hand circularly polarized (RHCP) wave cannot effectively propagate and reflected at the magnetoactive plasma boundary in the ECR magnetic field [24]. Instead, magnetic field greater than the ECR field, the microwave energy is transferred to kinetic energy of electrons in plasma and increases

the plasma density. Previous studies suggest that the magnetic field should be applied at slightly higher than the ECR field to form overdense plasma with no initial plasma for both plasma ignition and microwave absorption.

The high intensity singly charged ions such as proton beam can be obtained from the off-resonance mode of operation in microwave plasma. High electron density has been reported in previous studies, more than 10 times higher than the critical density, which means maximum density by the ECR operation [24]. Electron density normally increases as function of absorbed microwave power.

The high intensity MWIS can be classified into cavity type and antenna type, according to coupling structures. In cavity type MWIS, cavity length and axial magnetic field distribution are important parameters to design and operate this ion source [26]. Impedance matching is another crucial aspect to produce stable and dense plasma, whose load should be electrically separated from microwave generator. The plasma impedance is dependent on the input microwave power, axial magnetic field distribution, and plasma properties. An automatic stub tuner reads the forward/reflected power measured by directional coupler and performs feedback control to match the impedance.

Microwave discharge is utilized to generate a high-current proton beam. Microwave ion source has several advantages. First, electrode-less discharge is possible, so it is free from contamination by sputtering of internal electrodes. This has the advantage of long-term stability, which reduces the frequency of parts replacement and maintenance. In addition, plasma having a high degree of ionization and a high mono-atomic fraction can be generated without excessive heating of the background gas. Through this, it is possible to obtain a high current proton beam from the hydrogen ion source.

2.2. Beam Formation and Extraction

In the first acceleration gap, where the beam is formed, the space-charge forces acting on the beam are largest. The situation can be evaluated in one dimension by assuming a beam starting with zero velocity with Poisson equation.

$$\frac{\mathrm{d}^2\phi}{\mathrm{d}z^2} = -\frac{\rho}{\epsilon_0} = -\frac{J}{\epsilon_0}\sqrt{\frac{m}{2q\phi}} \tag{2.1}$$

As the emission current density increases, the electric field at the emission surface decreases until it becomes zero. At that point the emission current is at the maximum can be solved with the boundary condition as:

$$\frac{\mathrm{d}\phi}{\mathrm{d}z}(z = 0) = 0. \tag{2.1}$$

This condition is known as space-charge-limited emission, and the resulting limit for the maximum emission current density can be calculated using the following equation, which is known as the Child–Langmuir law.

$$J_{\max} = \frac{4}{9}\epsilon_0\sqrt{\frac{2q}{m}}\frac{V^{3/2}}{d^2} \tag{2.3}$$

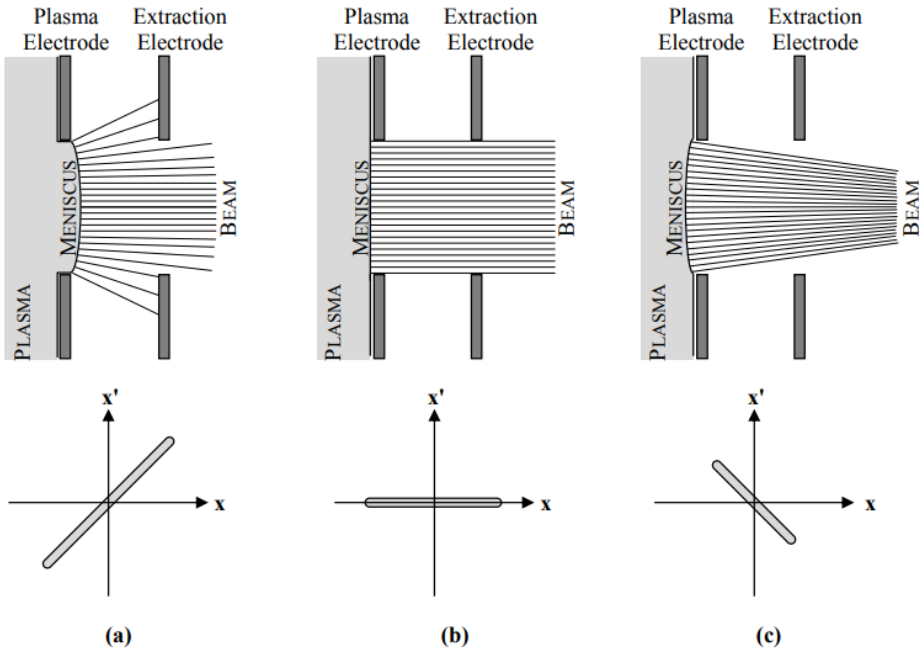

Figure 2. 4. Beam formation depending on a plasma meniscus [21].

The beam formation is dependent on both of an electric field structure and properties of the plasma. It can be conceptually divided into the three cases as depicted in Figure 2.4. The plasma meniscus, which is relevant to the balance between the electric field and properties of plasmas, can have convex, flat, and concave shape. When the plasma density is higher than the electric field near the beam extraction region, the meniscus has convex shape like Figure 4.2 (a), so that diverging beam can be continuously lost by hitting extraction electrodes and beam pipe even in a short drift. In case of Figure 4.2 (b), flat meniscus is a desirable case to extract the high beam current with the lowest beam emittance. The other is concave meniscus as Figure 4.2 (c), which normally produces the highest beam current, but with relatively higher emittance and divergence.

Some concave meniscus may be acceptable and be close to an optimal regime of beam formation, according to the combination with a following low energy beam transport section and the requirement of beam emittance at the end of the LEBT. This optimization can be obtained by

changing electric field or a plasma. To control the properties of plasmas is normally more difficult than to change electric field structure, since the ion sources used in high intensity proton mentioned in Section 2.1 have non-linear characteristics and make it difficult to diagnose the properties due to the lack of space.

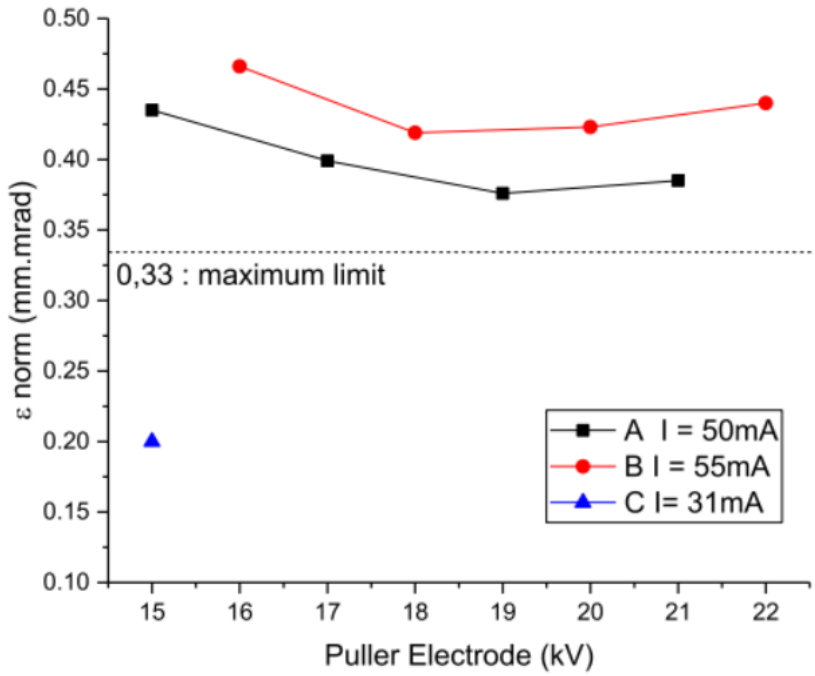

Figure 2. 5. Initial beam parameters depending on a puller electrode potential [27].

On the other hand, multi-electrode systems having four or more than five electrode enable an adjustment of electric field structure in an easy and intuitive manner, in spite of their complex structure to build and maintain. An intermediate electrode, it is sometimes called a puller electrode, is located between the plasma electrode and the outermost extraction electrode. Changing the electric potential of this puller electrode affect the characteristics of beam formation such as initial beam current and beam emittance as shown in Figure 2.5 [27].

2.3. Beam Parameters and Beam Dynamics

To describe distribution of particles in a beam in phase space, ellipse equation and matrix representation are used. The general equation of an ellipse centered at the origin can be written as:

$$ax^2 + bxy + cy^2 = 1 \tag{2.4}$$

Rewriting it as:

$$cy^2 + bxy + (ax^2 - 1) = 0 \tag{2.5}$$

Solving the quadratic equation for y,

$$y = \frac{-bx \pm \sqrt{(b^2 - 4ac)x^2 + 4c}}{2c} \tag{2.6}$$

The two solutions correspond to the upper and lower parts of the ellipse from -x_0 to +x_0.

The limits of x for this ellipse can be found when the quadratic equation has a multiple root as:

$$x_0 = \sqrt{\frac{4c}{4ac - b^2}} \tag{2.7}$$

The area of the ellipse is integration of the absolute value of the function,

$$\mathrm{A} = 2\int_{-x_0}^{x_0} \frac{\sqrt{(b^2-4ac)x^2+4c}}{2c}\,dx$$
$$= \frac{4}{\sqrt{4ac-b^2}}\int_{-1}^{1}\sqrt{1-u^2}\,du \tag{2.8}$$

$$\mathrm{A} = \frac{4}{\sqrt{4ac-b^2}}\int_{-\pi/2}^{\pi/2}\cos^2\theta\,d\theta = \frac{2\pi}{\sqrt{4ac-b^2}} \tag{2.9}$$

Maximum extent of the ellipse in the x and y direction can be written as:

$$x_0 = \sqrt{c}(A/\pi),$$
$$y_0 = \sqrt{a}(A/\pi) \tag{2.10}$$

Describing the equation of ellipse in matrix notation,

$$\mathrm{X} = \begin{pmatrix} x \\ y \end{pmatrix} \tag{2.11}$$

$$\mathrm{A} = \begin{pmatrix} a_{11} & a_{12} \\ a_{21} & a_{22} \end{pmatrix} \tag{2.12}$$

$$\mathrm{X}^T \cdot A \cdot X = \begin{pmatrix} x & y \end{pmatrix} \cdot \begin{pmatrix} a_{11} & a_{12} \\ a_{21} & a_{22} \end{pmatrix} \cdot \begin{pmatrix} x \\ y \end{pmatrix} = a_{11}x^2 + (a_{12}+a_{21})xy + a_{22}y^2 = 1 \tag{2.13}$$

In case of symmetric matrix A, $a_{12} = a_{21}$

$$\mathrm{X}^T \cdot A \cdot X = a_{11}x^2 + 2a_{12}xy + a_{22}y^2 = ax^2 + bxy + cy^2 = 1 \tag{2.14}$$

$$Area = \frac{2\pi}{\sqrt{4ac - b^2}} = \frac{2\pi}{\sqrt{4a_{11}a_{22} - 4a_{12}^2}} = \frac{\pi}{\sqrt{\det(A)}} \quad (2.15)$$

Two-dimensional beam matrix σ is defined as,

$$\sigma \equiv \langle \mathrm{X} \cdot \mathrm{X}^T \rangle = \left\langle \begin{pmatrix} x \\ y \end{pmatrix} \cdot (x\ y) \right\rangle = \begin{pmatrix} \langle xx \rangle & \langle xy \rangle \\ \langle yx \rangle & \langle yy \rangle \end{pmatrix} = \begin{pmatrix} \sigma_{11} & \sigma_{12} \\ \sigma_{21} & \sigma_{22} \end{pmatrix} \quad (2.16)$$

The inverse of the beam matrix is:

$$\sigma^{-1} = \frac{1}{\det(\sigma)} \begin{pmatrix} \sigma_{22} & -\sigma_{12} \\ -\sigma_{12} & \sigma_{11} \end{pmatrix} \quad (2.17)$$

Using the inverse matrix to make an ellipse equation,

$$\mathrm{X}^T \cdot \sigma^{-1} \cdot X = 1 \quad (2.18)$$

$$\sigma_{22}x^2 - 2\sigma_{12}xy + \sigma_{11}y^2 = \det(\sigma) = \left(\frac{\epsilon}{\pi}\right)^2 \quad (2.19)$$

ϵ is the area of the ellipse and is called the beam emittance.

In this context, Courant-Snyder parameters (α,β,γ) are introduced to describe the orientation and eccentricity of an ellipse that represents the shape and orientation of the particle distribution.

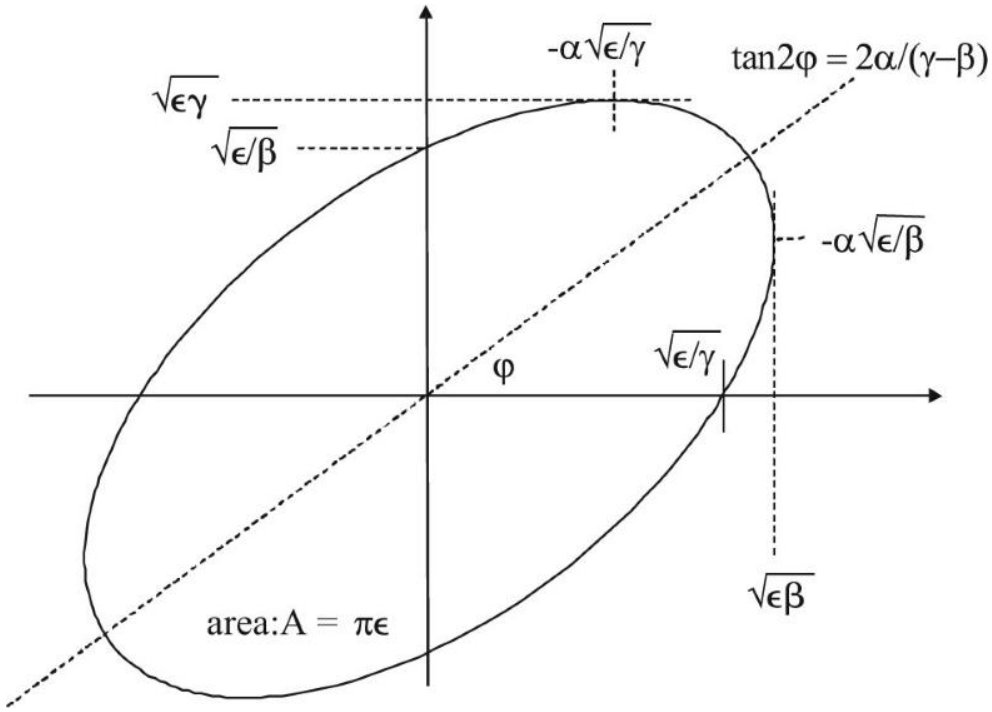

Figure 2. 6 Beam emittance and Courant-Snyder parameters in a phase space ellipse [28]

The above quadratic equation with a beam matrix can be rewritten with Courant-Snyder parameters as,

$$\gamma x^2 + 2\alpha xy + \beta y^2 = \frac{\epsilon}{\pi} \tag{2.20}$$

$$\alpha \equiv -\sigma_{12} / \left(\frac{\epsilon}{\pi}\right), \ \beta \equiv \sigma_{11} / \left(\frac{\epsilon}{\pi}\right), \ \gamma \equiv \sigma_{22} / \left(\frac{\epsilon}{\pi}\right) \tag{2.21}$$

Three Courant-Snyder parameters are not independent as a feature.

$$\beta\gamma - \alpha^2 = 1 \tag{2.22}$$

In x-x’ phase space, root-mean-square (rms) values are referred as,

$$x_{rms}{}^2 = \langle x^2 \rangle = \frac{1}{N}\sum_{i=1}^{N} x_i^2 \quad ,$$
$$x'_{rms}{}^2 = \langle x'^2 \rangle = \frac{1}{N}\sum_{i=1}^{N} x_i'^2 \quad , \qquad (2.23)$$
$$xx'_{rms} = \langle xx' \rangle = \frac{1}{N}\sum_{i=1}^{N} x_i x'_i$$

The maximum extent or the envelope of an ellipse refer to root-mean-square value of the distribution as follows,

$$x_0 = \left(\frac{Area}{\pi}\right)\sqrt{c} = \left(\frac{\epsilon}{\pi}\right)\sqrt{\sigma_{11}/\left(\frac{\epsilon}{\pi}\right)^2} = \sqrt{\sigma_{11}} = \sqrt{\langle x^2 \rangle} = x_{rms} \qquad (2.24)$$

And likewise, $x'_0 = x'_{rms}$

The rms emittance is defined as,

$$\epsilon_{rms} = \pi\sqrt{\langle x^2 \rangle\langle x'^2 \rangle - \langle xx' \rangle^2} \qquad (2.25)$$

The density of particles in phase space does not generally change along a beam transport line following Liouville’s Theorem, where conservative forces acting on particles can be derived from macroscopic electromagnetic fields.

Beam dynamics can be represented by the matrix operations in linear optics problem. Assuming a beam is only propagated by a linear transformation M from Point 1 to point 2,

$$\mathrm{X}_2 = MX_1 \tag{2.26}$$

Beam matrix at the point 2 is:

$$\sigma_2 = \langle X_2 X_2^T \rangle = \langle MX_1 (MX_1)^T \rangle = \langle MX_1 X_1^T M^T \rangle = M\sigma_1 M^T \tag{2.27}$$

When beam matrix M has a unit determinant, the phase space emittance is conserved and invariant during the propagation.

This representation of particles in a beam and Liouville's theorem allows simple and fast estimation of the beam parameters such as centroid and envelope, without calculation of individual particles. Beam dynamics simulation, such as *TraceWin* extensively used in this thesis, can perform this matrix multiplication (Envelope mode) as well as multiparticle tracking simulation (Partran mode) to calculate a beam transport [29].

2.4. Low Energy Beam Transport and Beam Matching

Low energy beam transport (LEBT) system in high intensity proton injector can be generally divided into two categories – electrostatic LEBT and magnetostatic LEBT. Table 2.1 summarizes parameters of LEBTs in worldwide high-intensity injectors.

Table 2.1. Low energy beam transport in worldwide high-intensity light ion injectors.

Facility	Particle, Energy	Focusing elements	Beam Current [mA]	RMS Emittance [pi mm mrad]
SNS	H-, 65 keV	2 Einzel lenses	35	0.22
J-PARC	H-, 50 keV	2 Solenoids	35	0.22
KOMAC	H+, 50 keV	2 Solenoids	20	0.3
LANSCE	H-, 80 keV	2 Solenoids	17	0.2
FAIR	H+, 95 keV	2 Solenoids	100	0.33
ESS	H+, 75 keV	2 Solenoids	55	0.2
LIPAc	D+, 100 keV	2 Solenoids	140	0.3

Electrostatic LEBTs are composed of a series of electrodes in a relatively shorter beamline than magnetostatic LEBT. These non-magnetic beamlines enable to be built in the form of open structure which can make a vacuum conductance. This compactness is also advantageous of minimizing the beam losses by charge exchange. Spallation Neutron Source (SNS) in Oak Ridge National Laboratory (ORNL) has a very short electrostatic LEBT in length less than 5 inches as shown in Figure 2.7. The electrodes act electrostatic focusing, deflecting and chopping. As another advantage of electrostatic LEBT, in the case of short pulse chopping, there is no transient time for space charge compensation.

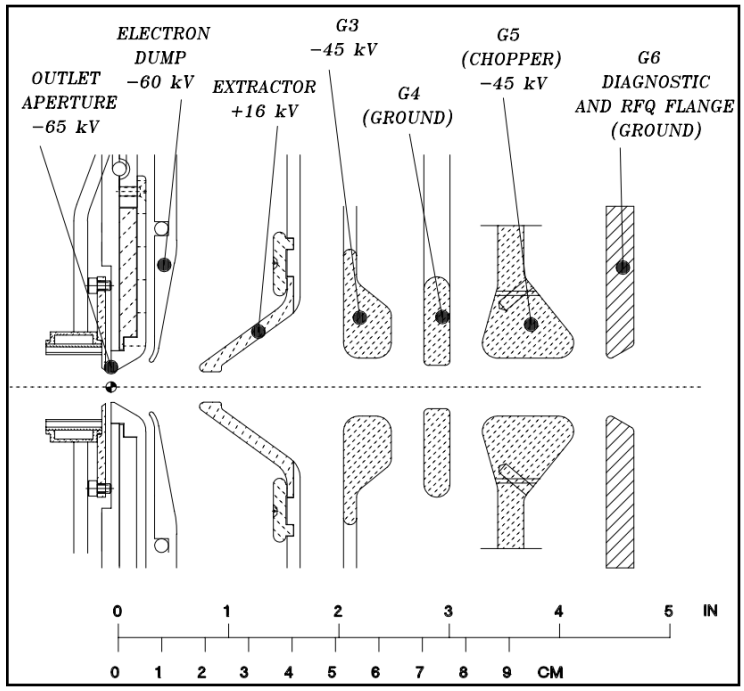

Figure 2. 7. A schematic diagram of the electrostatic low energy beam transport in Spallation Neutron Source [30].

On the other hands, electrostatic LEBTs have many disadvantages and are not preferred in general since they require many techniques and experience to overcome the expected problems. Electrostatic focusing elements attract or repel the electrons which are crucial to compensate space charge effects [30]. Near the electrostatic focusing elements, charge particle beams are un-neutralized and transport with their original space charge. Beam divergence and size can be exponentially increased with its intensity due to the un-neutralized beam characteristics. It means that this LEBT can be limited within some beam intensity without beam losses or severe emittance growth. Also, several electric field components are physically close each other, so that the injector is vulnerable to electrical breakdown or trip. An einzel lens is a standard electrostatic component that focuses beam without changing the energy of charged particles. An einzel lens intrinsically induces spherical aberrations which cause beam halo and

emittance growth than magnetic solenoid lenses [30].

Magnetostatic LEBTs typically consist of two solenoid magnets and two steerer magnets. Charged particle beam can be neutralized in magnetostatic LEBTs since neutralizing particles – in case of positive beam, electrons - are easily trapped in the beams without interruption by external electric field. Neutralizing electrons are mainly generated by ionizing collisions of positive beams with residual gases and secondary emission when beams hit the dense matters, such as electrode or inner wall of beam pipe. Beam emittance can be improved with compromise on beam losses in a high-pressure condition.

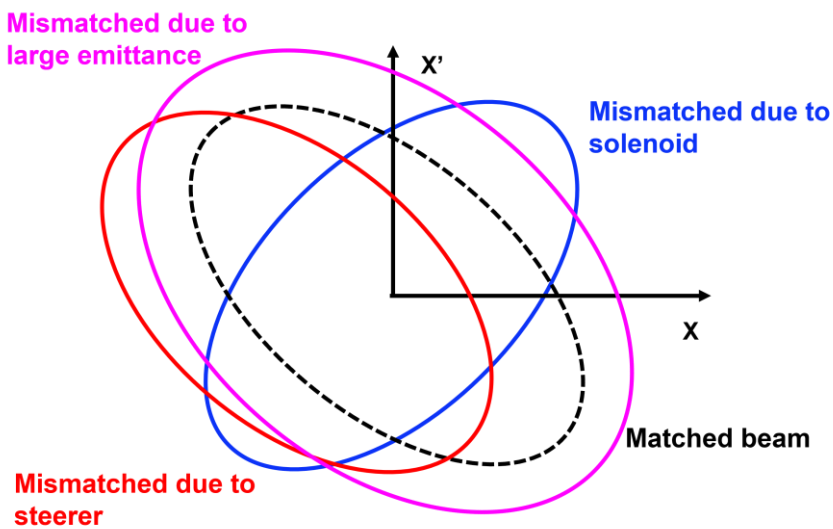

Figure 2. 8. Schematic diagram of beam mismatch in phase space

Beam matching and mismatch can be illustrated in phase space as Figure 2.8. Mismatched beam can be categorized into three types. The first case is a position shift or offset due to a wrong steerer control. The second one is over-focusing or under-focusing due to a wrong solenoid control. The third one is large emittance due to the emittance growth during beam transport. These are key elements of proper beam matching in the low energy beam transport section.

2.5. Beam Diagnostics for the Low Energy Beam

2.5.1. Single Faraday Cup

A Faraday cup collects electric charge of incident beam. It is electrically floated from a chamber ground and connected to a current meter such as pico-ammeter. The accuracy of this device depends on the noise level and charge collection efficiency. An accelerator is normally noisy environment to the Faraday cup installed in close proximity to many other high-power RF lines.

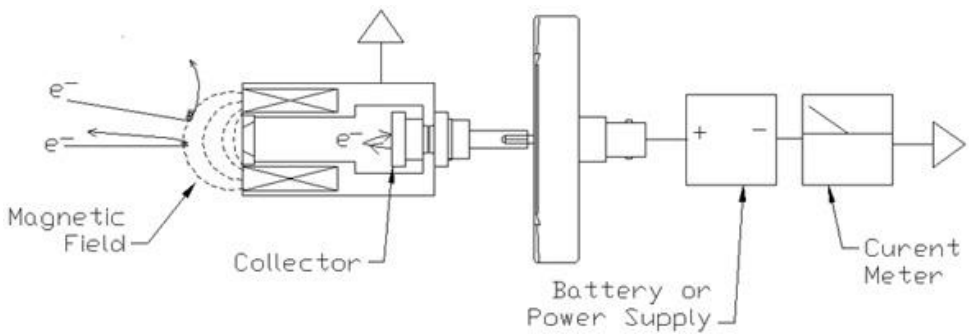

Figure 2. 9. The schematic diagram of a single-channel faraday cup.

The design of faraday cup is determined by particle's energy to be measured. Low-energy beam may be shortly stopped even in a very thin metal film, so that the thickness is not so important factor. Instead, lower energy proton beam produces more secondary electrons that carry the charge away and cause measurement error. To prevent secondary electrons from the Faraday cup, small magnets are attached nearby a collector as shown in Figure 2.10.

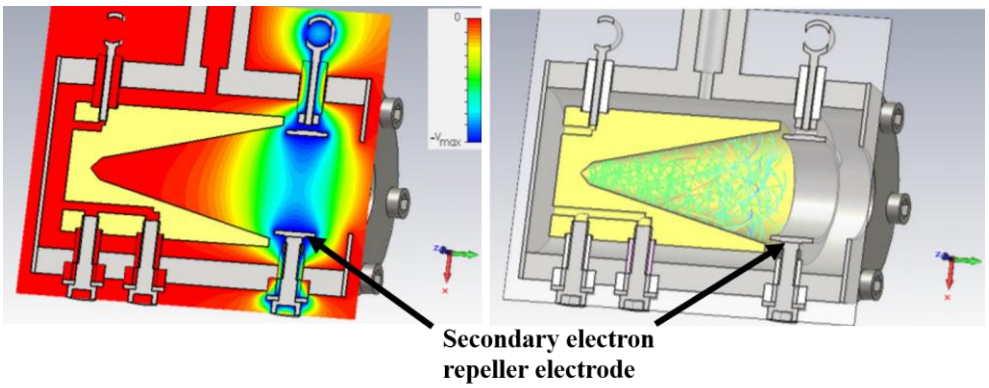

Figure 2. 10. Particle tracking in a single faraday cup by SIMION.

A negatively biased electrode can be added in front of the collector to repel electrons. Some simulation tool like *SIMION* is useful for a dedicated design by tracking charged particle beams and solving electromagnetic field equations, described in Figure 2.11**.**

2.5.2. Multi-pinhole Faraday Cup

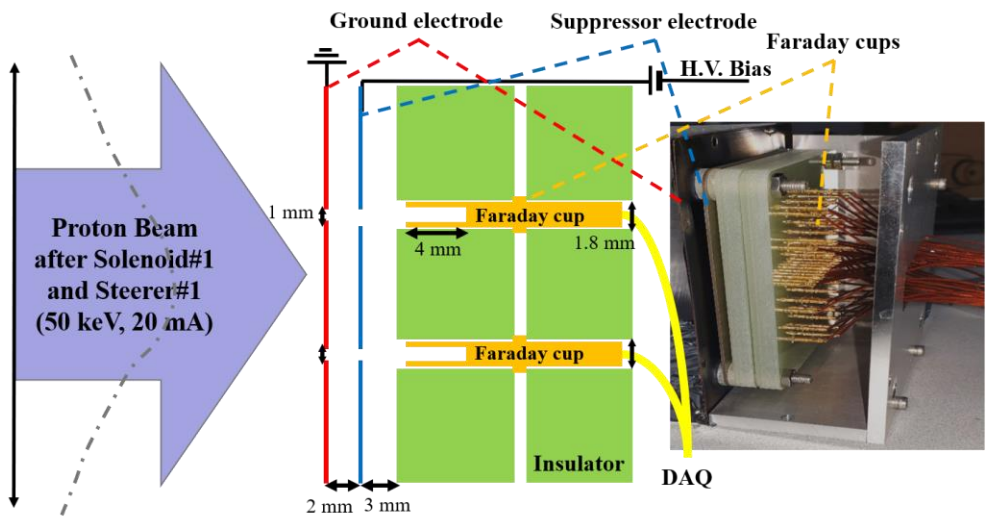

Figure 2. 11. The layout of a multi-pinhole faraday cup [32].

A multi-pinhole faraday cup (MPFC) is developed to measure transverse beam profiles. It has two parallel plates with many apertures in

the form of pepper-pot mask, and small copper cups to collect protons through the pinhole [31]. This has the similar design purpose and installed to measure two-dimensional beam current density profile.

A prototype MPFC is designed to assure its feasibility as candidate for time-resolved beam diagnostics tool as shown in Figure 2.11. A MPFC has two parallel electrodes made up of tantalum plate with a thickness of 0.25 mm and fifty respective faraday cups. The first plate is ground electrode to absorb most of beam current except for the one through apertures. The second plate is suppressor electrode to mitigate perturbation of measured ion current by secondary electron emission. The diameter of apertures in the two plates is 1 mm each. The last electrodes are small pin-typed faraday cups made from a gold-plated copper alloy [32].

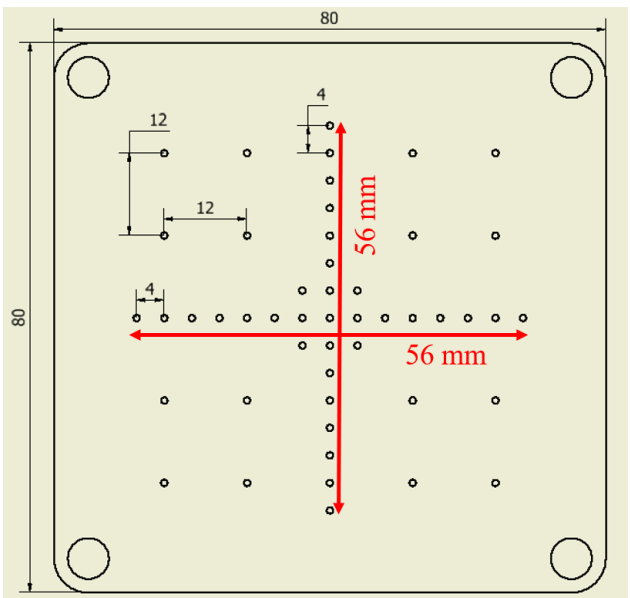

Figure 2. 12. Channel map of the MPFC [32].

The prototype MPFC has fifty channels which are 4 or 12 mm apart from each other to partially cover up to 56 mm * 56 mm of beam size at a time as illustrated in Figure 2.12. Each plate and faraday cup is electrically insulated by G10 epoxy glass laminate which is favored for its high physical

and chemical strength. All components above mentioned are assembled with bolts fastening, and are enclosed in grounded 5 mm-thick aluminum housing for the electromagnetic noise immunity. The assembly hung from a flexible in-vacuum bellows, so that the MPFC could be remotely armed or disarmed using bipolar stepper motor connected to a shaft with bellows. Bias voltage is fed into suppressor plate using high voltage supply module such as ORTEC 556 [32].

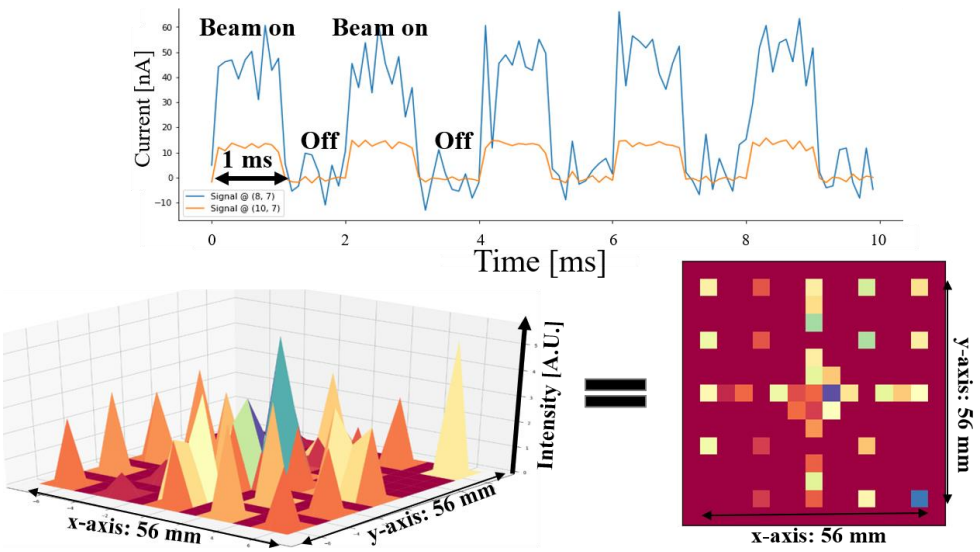

Figure 2. 13. Time evolution and density distribution of beam current measured by the homemade and prototype multi-pinhole faraday cup.

Data acquisition (DAQ) board is 128-channel electrometer I128 model with input current rating of +550 nA. This low current rating is limiting factor to measure high current, especially on the center channel in focused beam operation during solenoid scan. Current-integrated signals are extracted from I128 software and post-processed by Python for the two-dimensional imaging as plotted in Figure 2.13. There are alternative DAQ systems such as a general-purpose digitizer such as NI PXIe-6363 module. These diagnostics can be further tested with a robust DAQ, even though it is difficult to fabricate the device and prepare suitable electronics [32].

2.5.3. Scintillating Screen

Scintillation is the process in which energy deposited in a material is converted into photons. The creation of electronic excitations leads electron transport to luminescence centers, and eventually light emits from the centers. Scintillation is influenced by several factors such as temperature, concentration, and impurities. Inorganic scintillators are widely adapted for the detection of ionizing radiation. The representative material is Al2O3:Cr, so called Chromox-7, Quartz glass, and Gd2O2S:Tb (P43) as a powder screen.

To collect information from the illuminated screen by a beam irradiation, various photo-sensors such as photodiode, photomultiplier, SiPM and CCD camera, as depicted in Figure 2.14, can be combined use. In this regard, proper selection is needed to collect the light effectively, since scintillators have their own light emission spectrum. Visible light is widely allowable and compatible to most of optical devices, but in case of scintillator having emission spectrum near the ultraviolet, proper optical components should be utilized.

2.6. Machine Learning and its Application in Accelerator Control

Recently, the field of machine learning has been in the spotlight because of its superior performance to humans in certain fields, from natural language processing such as speech recognition and handwriting recognition, to image recognition and automatic operation of machines. Tom Mitchell provides the modern definition on machine learning as [33]:

“A computer program is said to learn from experience E with respect to

some task T and some performance P, if its performance on T, as measured by P, improves with experience E."

Machine learning, especially supervised learning dealt with this thesis, refers to the process of finding appropriate parameter values by training "labeled" input and output values. Artificial neural networks (ANN) are sub-category of the machine learning and software implementations of the neural structure of our brains. Neurons which are kind of like organic switches can change their state depending on the strength of their electrical or chemical input. Learning occurs by repeatedly activating certain neural connections over others, and this reinforces those connections. ANN attempt to simplify and mimic this brain behavior. In a supervised ANN, the network is trained by providing matched input and output data samples, with intention of getting the ANN to provide a desired output for a given input.

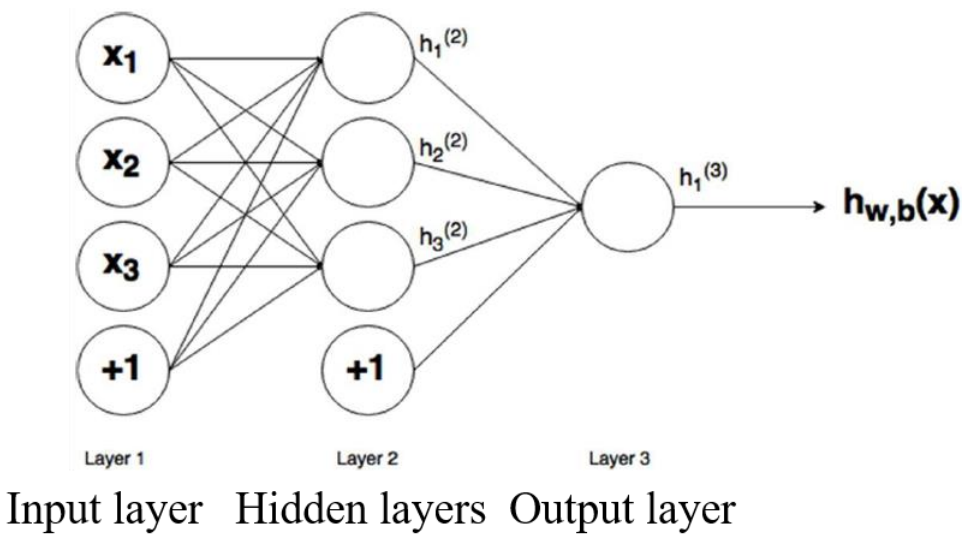

Figure 2. 14. Schematic diagram of three layer neural network [34].

Neurons are connected hierarchical networks, with the outputs of

some neurons being the inputs to others. The unit of a connection is called node or perceptron. Each node takes multiple weighted and biased inputs and is simulated by an activation function to the summation of these inputs. Output may be calculated in the feed-forward way. Figure 2.13 shows three layers of neural network with three notations and formulas on output node [34].

- Weight notation: $w_{ij}^{(l)}$ - *btw* node i in layer l *and* node j in layer l+1
- Bias notation: $b_i^{(l)}$ - node i in layer l
- Output notation: $h_i^{(l)}$ - node i in layer l

$$\begin{aligned} h_1^{(2)} &= f(w_{11}^{(1)}x_1 + w_{12}^{(1)}x_2 + w_{13}^{(1)}x_3 + b_1^{(1)}) \\ h_2^{(2)} &= f(w_{21}^{(1)}x_1 + w_{22}^{(1)}x_2 + w_{23}^{(1)}x_3 + b_2^{(1)}) \\ h_3^{(2)} &= f(w_{31}^{(1)}x_1 + w_{32}^{(1)}x_2 + w_{33}^{(1)}x_3 + b_3^{(1)}) \\ h_{W,b}(x) &= h_1^{(3)} = f(w_{11}^{(2)}h_1^{(2)} + w_{12}^{(2)}h_2^{(2)} + w_{13}^{(2)}h_3^{(2)} + b_1^{(2)}) \end{aligned} \quad (2.31)$$

Matrix multiplication and vectorization are used to write general equations for calculation in neural networks.

$$z_1^{(2)} = w_{11}^{(1)}x_1 + w_{12}^{(1)}x_2 + w_{13}^{(1)}x_3 + b_1^{(1)} = \sum_{j=1}^{n} w_{ij}^{(1)}x_i + b_i^{(1)} \quad (2.32)$$

$$z^{(l+1)} = W^{(l)}h^{(l)} + b^{(l)} \quad (2.33)$$

$$h^{(l+1)} = f(z^{(l+1)}) \quad (2.34)$$

In training the neural network, the goal is to obtain better prediction. The cost function is generalized formulation to represent the degree of error. The equivalent cost function of a single training pair (x^z, y^z) is:

$$J(w,b,x,y) = \frac{1}{2} || \, y^z - \mathrm{h}^{(n_l)}(x^z) \, ||^2 = \frac{1}{2} || \, y^z - y_{pred}(x^z) \, ||^2 \tag{2.35}$$

Mean squared error (MSE) over all *m* training pairs is:

$$J(w,b) = \frac{1}{m} \sum_{z=1}^{n} \frac{1}{2} || \, y^z - \mathrm{h}^{(n_l)}(x^z) \, ||^2 = \frac{1}{m} \sum_{z=1}^{n} J(w,b,x^{(z)},y^{(z)}) \tag{2.35}$$

Gradient descent method is the most common algorithm used to find the local minima in an optimization problem. This method updates weight and bias iteratively towards the minimum cost. Iteration can be stopped after a certain number of iterations or stop condition.

$$w_{ij}^{(l)} = w_{ij}^{(l)} - \alpha \frac{\partial}{\partial w_{ij}^{(l)}} J(w,b) \tag{2.36}$$

$$b_i^{(l)} = b_i^{(l)} - \alpha \frac{\partial}{\partial b_i^{(l)}} J(w,b) \tag{2.37}$$

While comparing the output of the neural network to our expected training value, the cost function can be changed. It is necessary to evaluate the gradient for all the hidden layers and to find out how much a change in the weight has on the cost function. the cost function can be directly calculated by comparing the output layer to the training data.

Using backpropagation algorithm, delta rule is adapted to calculate $\delta^{(l)}$ and to update the difference of weight and bias, $\Delta W^{(l)}$ and $\Delta b^{(l)}$, in each layer. Finally, a gradient descent method is performed to find local minima of the weights and bias [34].

$$W^{(l)} = W^{(l)} - \alpha[\frac{1}{m}\Delta W^{(l)}] \tag{2.38}$$

$$b^{(l)} = b^{(l)} - \alpha[\frac{1}{m}\Delta b^{(l)}] \tag{2.39}$$

The process of finding the optimal convergence value by updating the weight and bias of the node in each layer from the formulas described above is repeated every epoch, and Figure 2.15 below shows this process.

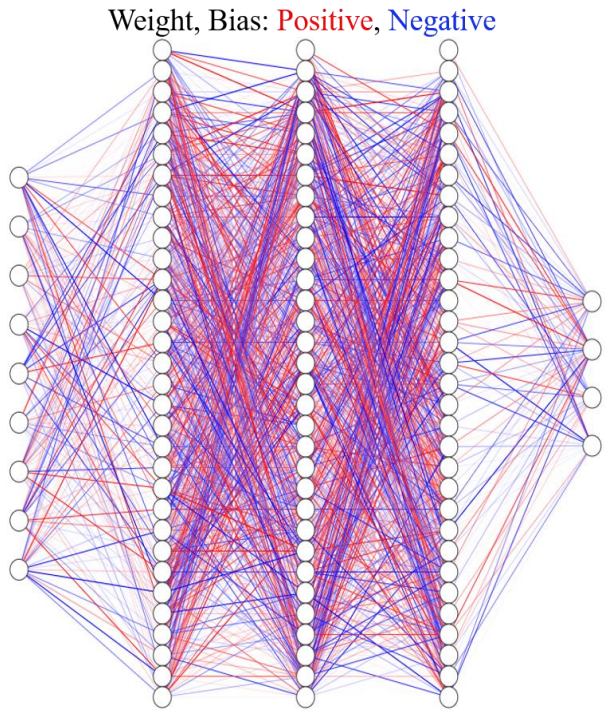

Figure 2. 15 Update of weight and bias during the learning process.

These algorithms are the key of mathematical understanding the neutral network in the machine learning. To make better performance and generalization without overfit data, various techniques have been developed and adopted such as multiple hidden layers called deep layers, dropout, novel fast optimizer, max pooling, regularization, and so on.

In accelerator physics and experiments, machine learning-based regression, classification, and prediction have been utilized to improve diagnostics data to measure beam parameters such as position, size and phase [15].

The most prevalent and useful application ML-based beam optics correction and alignment. In previous studies, optics correction has been based on probability theory such as Bayesian. Simulations with randomly generated errors in the focusing magnets are utilized to train and validate the regression model [35]. As another example, automation of specific tasks like collimator alignment at Large Hadron Collider saves many operational resources in a machine control room [16].

In linear accelerator, the LANSCE has utilized particle swarm optimization (PSO) and genetic algorithm (GA) as a fast optimization technique. Beam matching into the drift tube linac (DTL) and tuning of DTL and buncher are major applications to apply multi-objective optimization techniques based on machine learning [36].

Chapter 3. Experimental Setup of Proton Injector Test Stand

In the 100-MeV accelerator, which is usually in operation as a user facility, there is a limitation to install new beam diagnostics and to test beam control technique. This section describes the newly constructed proton injector test bench and compares it with the proton injector of the existing 100-MeV accelerator. It also describes Microwave ion source, beam extraction system, low energy beam transport system, and beam diagnostics.

3.1. Microwave Ion Source and Beam Extraction System

Microwave discharge is utilized to generate a high-current proton beam. Microwave ion source has several advantages. First, electrode-less discharge is possible, so it is free from contamination by sputtering of internal electrodes. This has the advantage of long-term stability, which reduces the frequency of parts replacement and maintenance. In addition, plasma having a high degree of ionization and a high mono-atomic fraction can be generated without excessive heating of the background gas. Through this, it is possible to obtain a high current proton beam from the hydrogen ion source [37].

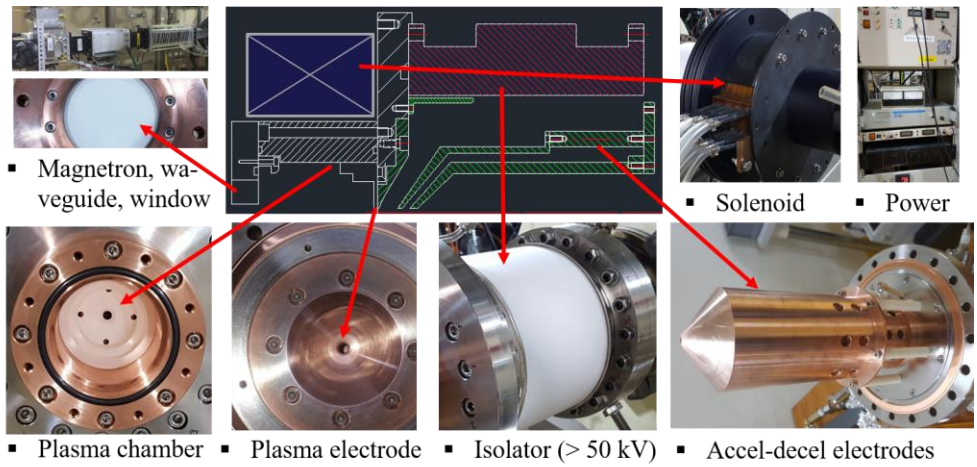

Figure 3. 1. Pictures and drawings of components included in microwave ion source and beam extraction system.

Microwave ion source consists of cathode-less plasma chamber, insulated solenoid magnet, beam extraction electrodes, high-voltage vacuum feedthrough, hydrogen gas feeding line, and cooling water line as shown in Figure 3.1. In particular, the system that applies the 2.45 GHz microwave to the plasma chamber is composed of Magnetron, directional coupler, isolator for blocking reflected wave, 4E auto-tuner for impedance matching, DC break waveguide, and double ridged waveguide. The plasma chamber and the part electrically connected to it are all floating at 50 kV when extracting the proton beam. Therefore, the hydrogen gas feeding line and the cooling water line are grounded away from the plasma chamber to prevent electric sparks caused by undefined electric potential.

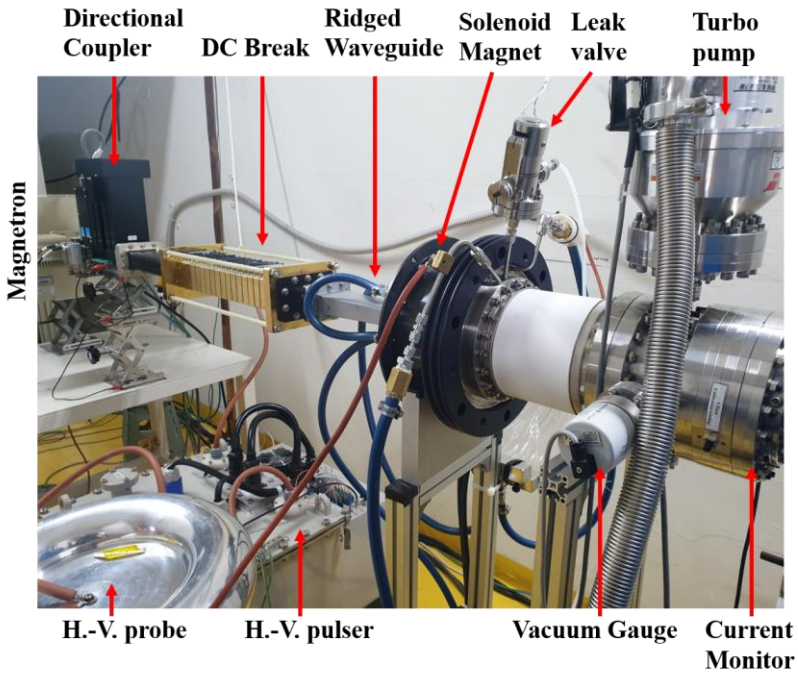

Figure 3. 2. Picture of the microwave ion source and beam extraction system applied in proton injector test stand.

Figure 3.2 is a picture of the microwave ion source and beam extraction system in the proton injector test stand. Pulsed proton beam can be extracted with a pulse width of maximum 1.33 millisecond in 60 Hz by fast high voltage pulser made up of IGBTs. Beam current is monitored in two different positions by current transformers – the first one located right after the ion source and the second one located right after a bending magnet. Proton beam extraction is accomplished by applying a positive high voltage of 50 kV to the plasma chamber and plasma electrode, and grounding the extraction electrode to 0 V. For insulation of 50 kV, *CeramTec* 17146-03-CF model is adopted as an insulating vacuum pipe, and the length of the insulation made of alumina ceramic is 114 mm. There is a suppression electrode that applies a negative voltage of up to -4 kV between the plasma electrode and the extraction electrode to prevent secondary electrons from

flowing back to the plasma chamber.

3.1.1. Hydrogen Plasma Diagnostics and Estimation of Plasma Properties on Microwave Ion Source

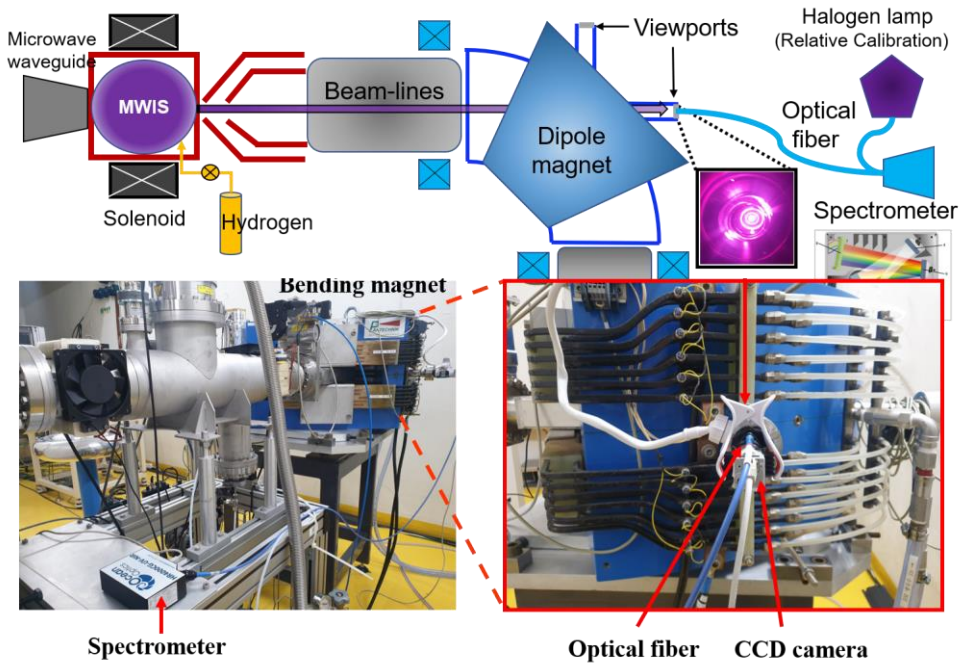

Figure 3. 3. The layout and picture of optical emission spectroscopy installed at the proton injector test stand.

The ion source is an important part of the initial beam formation. Plasma characteristics should be studied in order to form a beam with good beam characteristics parameters with high current. Because the temperature inside the ion source is very high and a high voltage of 50 kV is applied, it is not easy to measure the characteristics with an intrusive probe. Optical emission spectroscopy is a diagnostic method to indirectly measure hydrogen emission light. For an optical data acquisition, window viewport and optical fiber is installed in the straight line from the ion source aperture to the dipole bending magnet as shown in Figure 3.3.

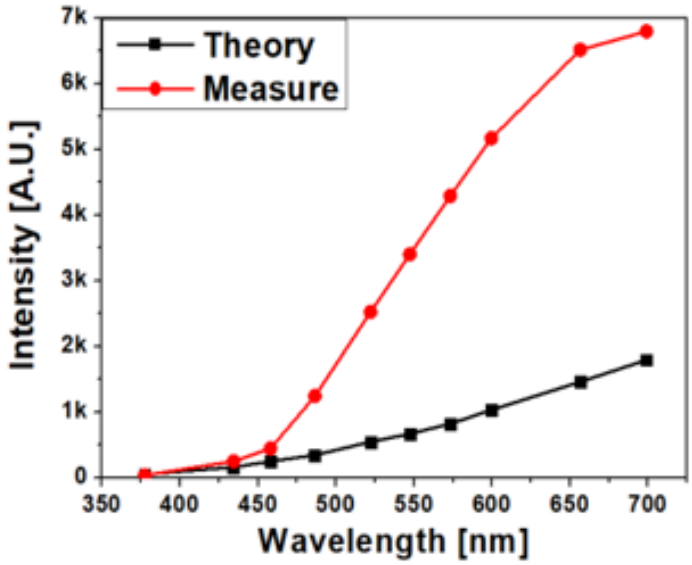

Figure 3. 4. Efficiency calibration data of spectrometer using Halogen-Tungsten lamp.

The spectrometer used in experiments is HR-4000 (*OceanOptics Co.*). The spectroscopic device requires two different calibrations – wavelength and efficiency calibration. Wavelength calibration can be performed with a mercury-argon lamp which has well-known multiple peaks such as 253.65 nm, 296.73 nm, 302.15 nm, and so on. A third-order polynomial function is fitted by a linear regression.

$$\lambda_p = I + C_1 p + C_2 p^2 + C_3 p^3 \tag{3.1}$$

Efficiency calibration uses a tungsten-halogen lamp with a theoretical data on the continuous emission spectrum as illustrated in Figure 3.4. Efficiency calibration is more important in the study since this plasma diagnostics analyzes the intensity ratio of well-known hydrogen Balmer lines. The efficiency calibration data is periodically obtained since it may

drift slightly as time and environment and have a sensitive effect on the measured data.

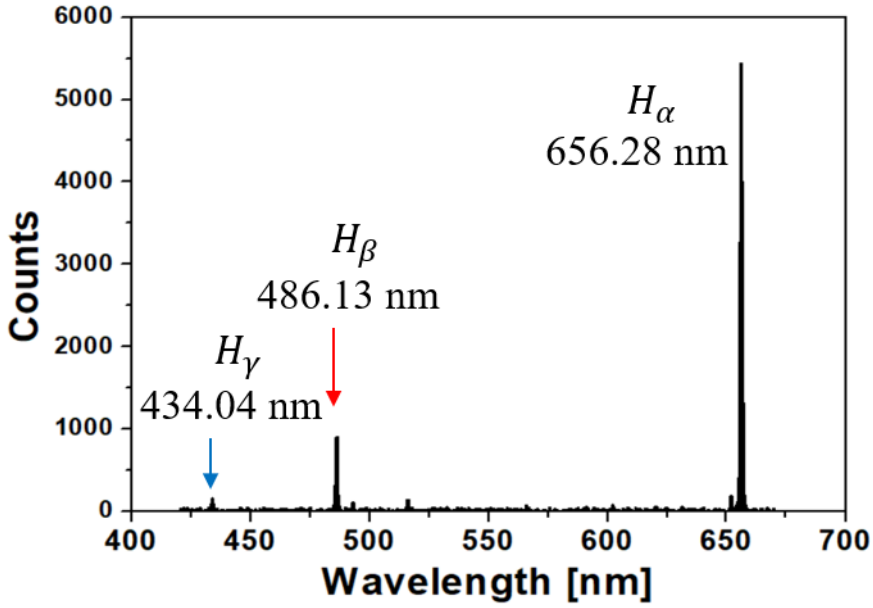

Figure 3. 5. An example of measured emission spectrum from the microwave hydrogen plasma.

The measured spectrum is shown in Figure 3.5 and three dominant Balmer lines can be observable. A light acquisition time is determined by H-gamma intensity so that this weak line can be distinguished from background noises.

Theoretical line intensity ratio is numerically calculated by solving a set of steady-state rate equations to determine population densities [38-40]. To estimate plasma properties, measured line ratio is entered into theoretical equation derived from the collisional radiative model on hydrogen as:

$$\frac{I_{H_\beta}}{I_{H_\alpha}} = \frac{E_{42}A_{42}n(4)}{E_{32}A_{32}n(3)} = \frac{E_{42}A_{42}n_H R_4(n_e,T_e)}{E_{32}A_{32}n_H R_3(n_e,T_e)} \quad (3.2)$$

$$\frac{I_{H_\gamma}}{I_{H_\alpha}} = \frac{E_{52}A_{52}n(5)}{E_{32}A_{32}n(3)} = \frac{E_{52}A_{52}n_H R_5(n_e,T_e)}{E_{32}A_{32}n_H R_3(n_e,T_e)} \quad (3.3)$$

$$\left[\frac{I_{H\alpha}}{I_{H\beta}}\right]_{exp} = \left[\frac{I_{H\alpha}}{I_{H\beta}}\right]_{th}(n_e, T_e) \tag{3.4}$$

$$\left[\frac{I_{H\alpha}}{I_{H\gamma}}\right]_{exp} = \left[\frac{I_{H\alpha}}{I_{H\gamma}}\right]_{th}(n_e, T_e) \tag{3.5}$$

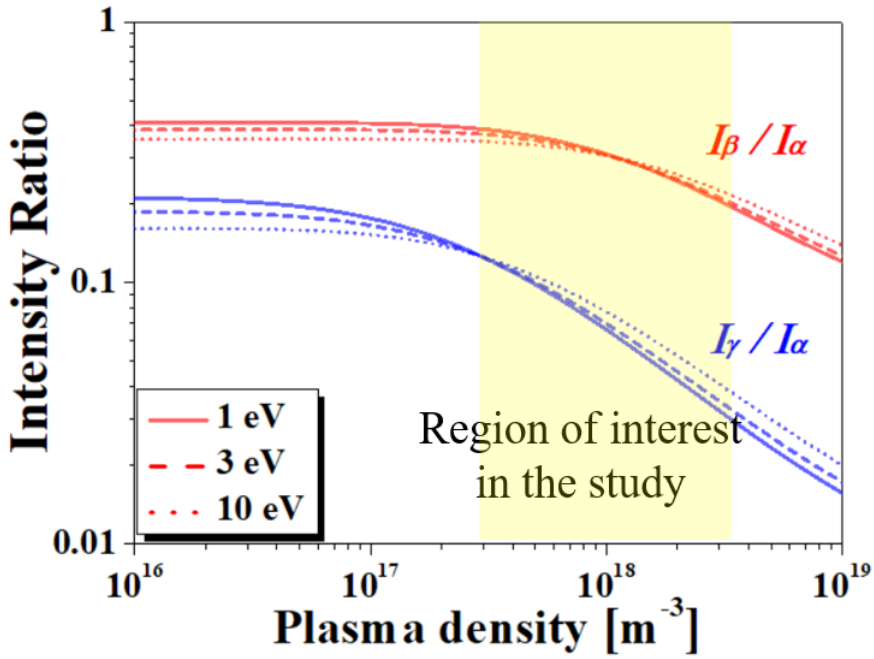

Figure 3. 6. Theoretically driven line-intensity ratio curve from the hydrogen collisional radiative model.

Plasma properties affect population density of states in hydrogen plasma. In low density and low temperature plasmas, line intensity ratio is mainly affected by electron temperature which is closely related to electron-impact excitation from the ground state. It generally follows corona regime in optical emission spectroscopy.

On the other hand, in high density region, plasma density has an

impact on the line intensity ratio since transitions between adjacent states is important in this region. Microwave ion source used in the high-intensity injector is operated in off-resonance mode where plasma density is much higher than the critical density at 2.45 GHz electron cyclotron resonance – $n_e = 7.5 \times 10^{16}\, m^{-3}$ [37].

In the ion source of the study, plasma density is roughly placed in the region of $n_e = 3 \times 10^{17} \div 3 \times 10^{18}\, m^{-3}$ where the plasma density is more dependent on intensity ratios than the plasma temperature. For simplicity of analysis, plasma temperature is assumed to be 3 eV and plasma density is estimated by measurement and theoretical data.

The dependency of the plasma densities according to the ion source operating conditions as summarized in Figure 3.7 and Figure 3.8.

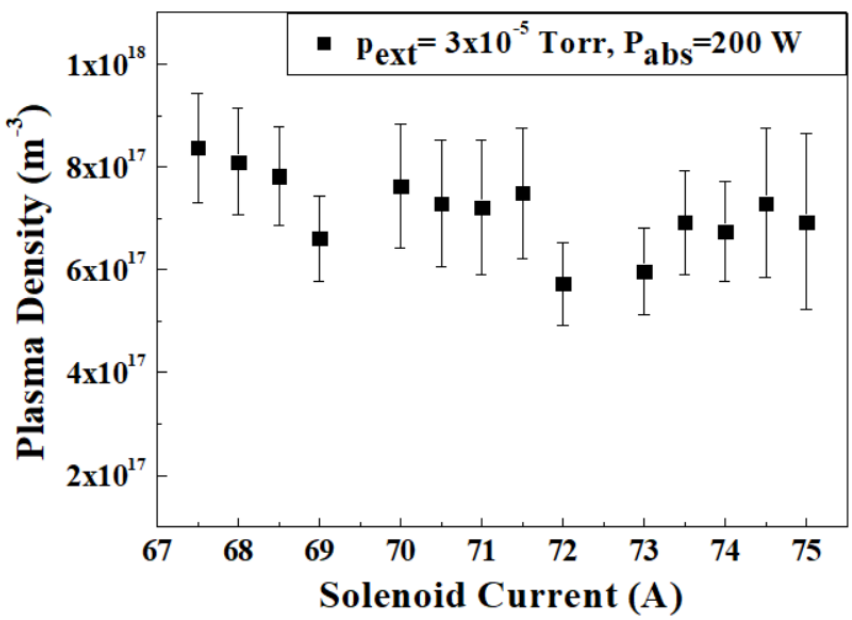

Figure 3. 7. Plasma density depending on the solenoid current.

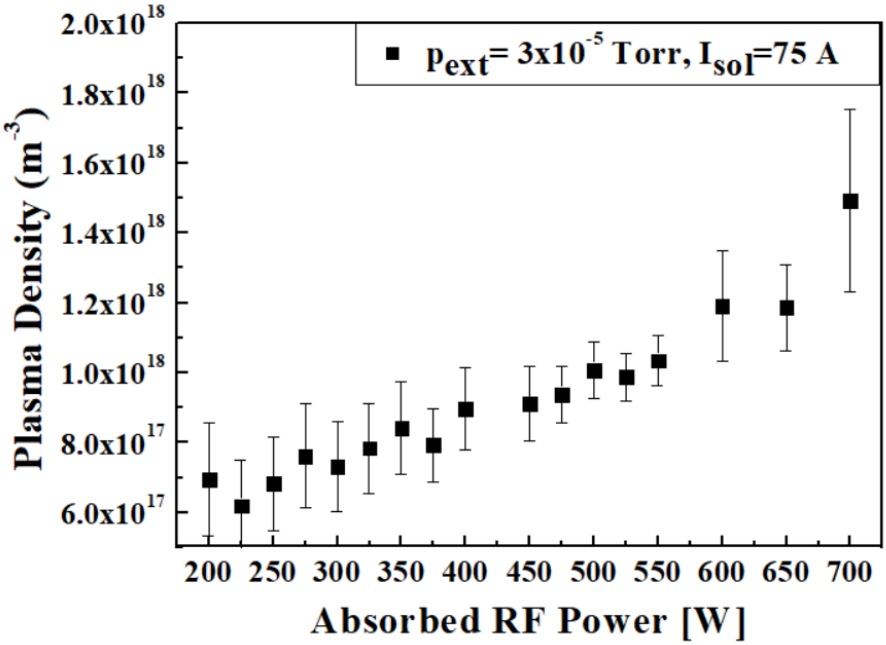

Figure 3. 8. Plasma density depending on the absorbed RF power.

For the solenoid current, the trend of plasma density is not clearly seen because of non-linearity between magnetic field strength and plasma formation in the source. The magnetic field strength changes in proportion to the current strength applied to the solenoid magnet, which affects plasma density and temperature. In the microwave ion source, there is a nonlinear relationship between the magnetic field and the plasma characteristics, and there is a region where the 2.45 GHz microwave transmitted from the magnetron causes electron cyclotron resonance (ECR) locally, and the density and temperature within the plasma chamber are inhomogeneous.

Absorbed RF power shows a positive correlation with plasma density. Using this clear correlation, it is possible to increase beam transmission or reduce beam losses by performing beam extraction under conditions with good optics. These plasma measurement data are used to understand beam optics in beam extraction experiments and simulation studies.

3.1.2. Beam Extraction Experiments and Beam Current Measurement

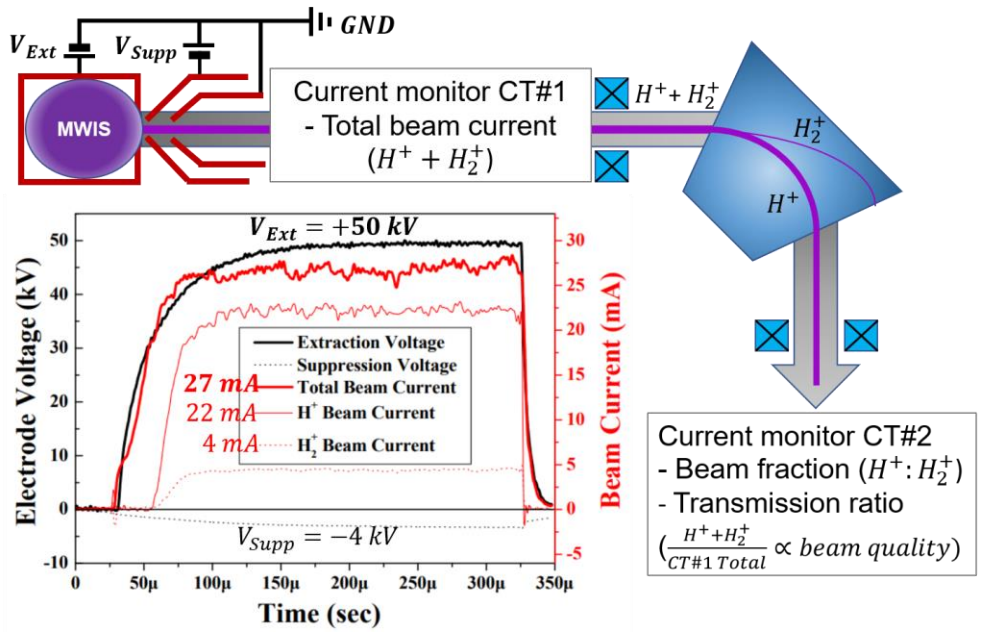

Figure 3. 9. The schematic of beam extraction and the beam current measurement at two positions: upstream and downstream the dipole bending magnet.

Microwave discharge is in a dc-operation state, and when high voltage is applied in the form of a pulse to the plasma electrode and the suppression electrode, a pulse beam is extracted. Figure 3.9 demonstrates the schematic diagram of beam extraction experiment and beam current measurement. An electric potential difference of 50 kV is applied between the plasma electrode and the extraction electrode, and the rise time is about 50 μs. At the beginning, the electric potential rises and as it approaches the plateau, the extracted beam current also approaches the plateau. And a constant beam current is maintained while the extraction voltage is maintained at the maximum. The first beam current monitor is installed downstream of the

bias feedthrough flange in the ion source extraction system. Not only H^+ contained in hydrogen plasma, but also H_2^+ and H_3^+ are generated together in a specific ratio, and the total current is measured.

There is a dipole magnet that bends the beam at 90 degrees, which can selectively pass the particle species according to the difference in mass and charge, or magnetic rigidity. For a 50 keV proton beam, a uniform magnetic field of about 808 G is required for a 90 degree circular motion with a radius of curvature of 400 mm. On the other hand, in the case of an H2+ beam, it can be transported with a magnetic field of 1142 G. In the case of H3+, it accounts for 0.1% of the system and is ignored. Atomic fraction and transmission ratio of the beam can be estimated by the ratio of the current values of the two current monitors located upstream and downstream the dipole bending magnet.

The atomic fraction is basically determined by the design of the ion source and is a value that changes depending on the operating conditions. The wall liner is a component that affects the beam fraction, and it has a different beam fraction depending on the material such as boron-nitride (BN) and aluminum-nitride (AlN). As a result of the beam fraction measurement test for the two materials, aluminum-nitride obtained an average of 80% and boron-nitride an average of 84% mono-atomic fraction, showing no significant performance difference for the same dimension of the liners.

Another information that can be obtained from beam current measurement is the transmission ratio, which is related to the initial beam optics. This dipole bending magnet has a gap of 70 mm, so the beam pipe acts as a collimator. That is, a low-quality beam incident with large divergence shows a low transmission ratio. Since there is no focusing element between the ion source extraction system and the dipole magnet, the higher transmission ratio can be obtained in this region with better beam

optics. This device configuration has the advantage of quickly finding the operating conditions of an ion source having a low emittance beam without mounting an emittance measurement unit downstream the ion source extraction system.

Table 3. 1. The operation conditions of ion source and measured beam current data.

Ion source control parameters	Input values	Measurable beam parameters	Output values
Hydrogen flow rate	2.0 sccm	H^+ beam current	21.8 mA
Microwave power	410 W	H_2^+ beam current	4.3 mA
Solenoid current	75.8 A	Atomic beam fraction	83.5% (21.8 / 26.1)
Extraction voltage	+50 kV, -3 kV	Transmission ratio	97.4% (26.1 / 26.8)

The waveform graph presented in Figure 3.9 is an example of a condition with good beam optics, and the operating conditions and measurement results are summarized in Table 3.1. Under the conditions of hydrogen 2.0 sccm, microwave power 410 W, and solenoid current 75.8 A, the atomic beam fraction is 83.5%, and the transmission ratio is calculated to be 97.4%.

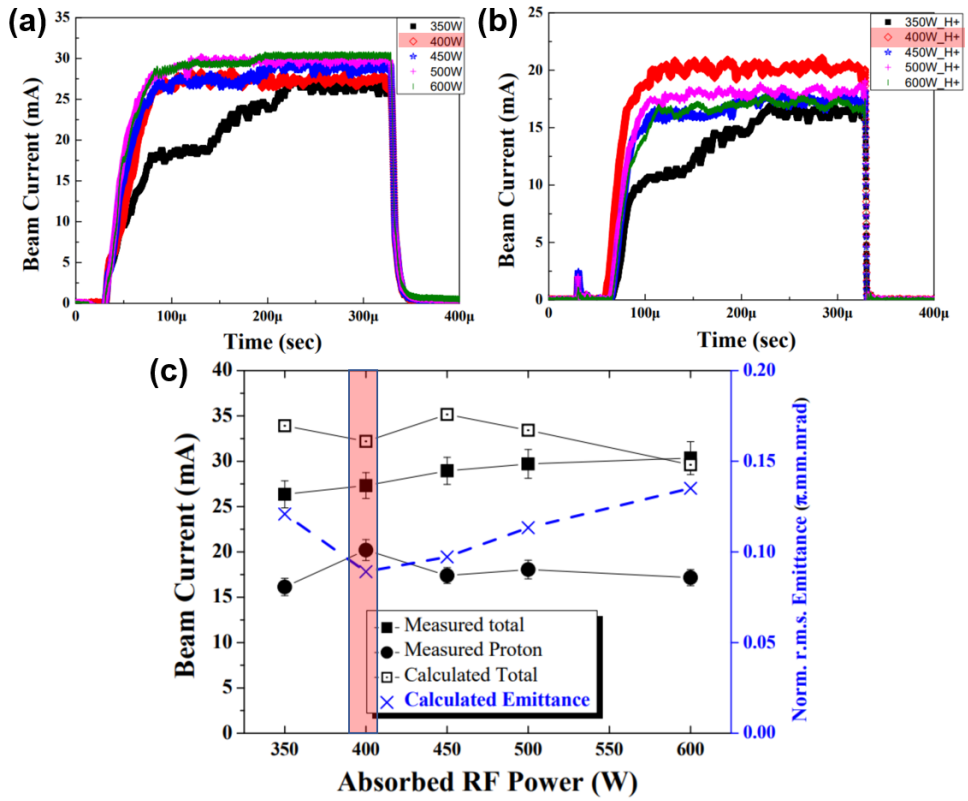

Figure 3. 10. Beam current waveform – (a) total beam current (CT#1) upstream the dipole bending magnet, (b) proton beam current (CT#2) downstream the bending magnet – and (c) comparison with calculated beam current and beam emittance.

Figure 3.10 compares and interprets the measurement and simulation results according to the absorbed microwave power among the control parameters of the ion source. Figure 3.10 (a) is the waveform of the total current measured at the CT#1, Figure 3.10 (b) is a dipole magnet after shows the waveform of a proton current measured at the CT#2. Here, the comparison of the average result for (200 – 300) μs, where the beam extraction is in a steady state, with the result of beam extraction simulation is shown in Figure 3.10 (c). As the input of the simulation, the plasma properties value is important, and the value measured by optical emission

spectroscopy is used according to the ion source operation variable. According to the calculation result, the total current shows a larger value than the measured value, and the beam emittance shows the lowest in the case of 400 W. Through this, it can be explained that it has the best beam optics and the highest transmission ratio in the condition near 400 W.

3.2. Low Energy Beam Transport System

The Low Energy Beam Transport (LEBT) system properly transports the beam extracted from the ion source to a subsequent RF accelerator. In general, the accelerator next to the LEBT system in a high-intensity proton accelerator is a radio-frequency quadrupole (RFQ). The RFQ accelerator is an efficient system that simultaneously accelerates, focuses, and bunches low-energy charged particles, but has certain requirements for input beam parameters. The center and size of the beam must fit well with the RFQ inlet aperture, and the angle at which the beam is incident should also meet a requirement.

In the installation process of proton injector test stand, LEBT beamline, which is longer than 3 meters, is fundamentally aligned with laser leveling devices as shown in Figure 3.11. In spite of some basic and mechanical alignment, it is considered that beamline elements are not perfectly aligned, but have a few alignment errors that can affect overall beam trajectories in a LEBT. This is the reason that steerers should be installed and optimization of their operating values is needed.

(a) From ion source to LEBT

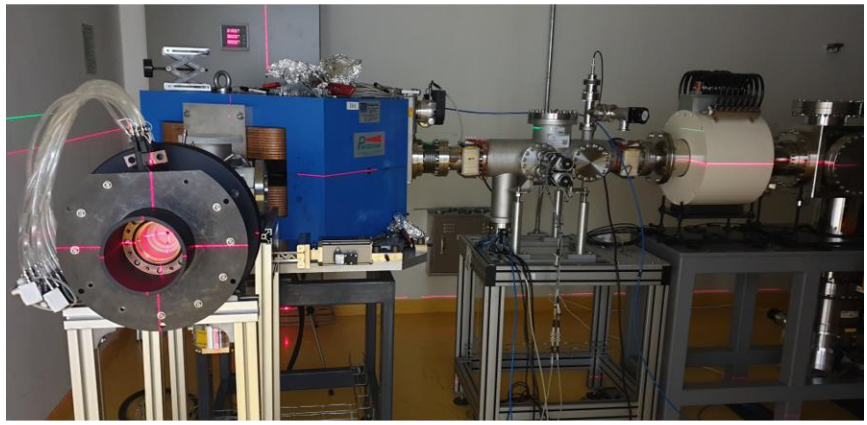

(b) From LEBT to RFQ

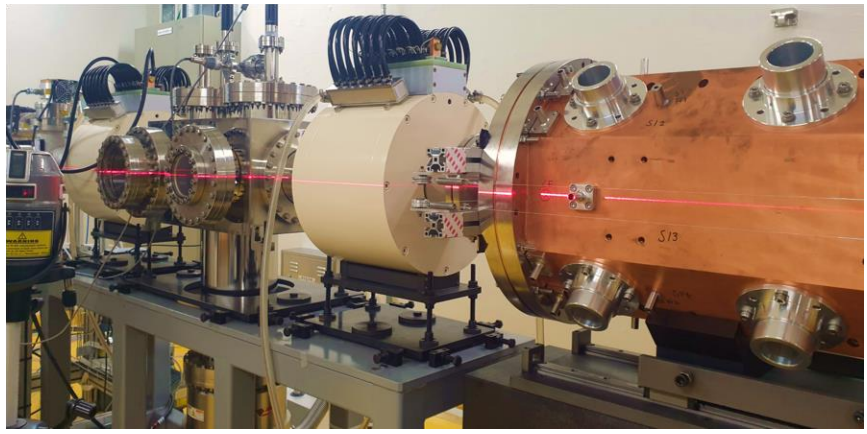

Figure 3. 11. The LEBT beamline alignment using laser leveling devices.

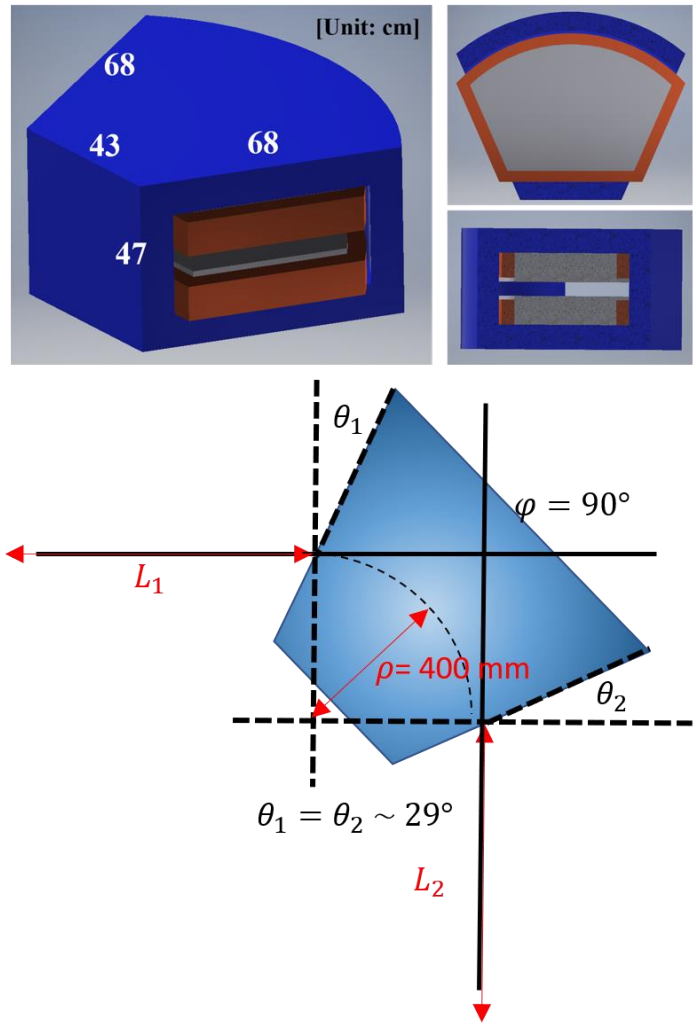

Figure 3. 12. Schematic diagram of dipole bending magnet in the LEBT.

In the LEBT system of the proton injector test stand, the bending magnet and solenoid magnet control the size of the beam, and the bending magnet and steerer magnet control the center position of the beam. Beam parameters such as beam size and beam center position at a specific location change according to the combination of operating values for these magnets. Figure 3.12 is a schematic diagram of a bending magnet. It is symmetric double-focusing dipole magnet, which has the same focal length in entrance

direction and exit direction.

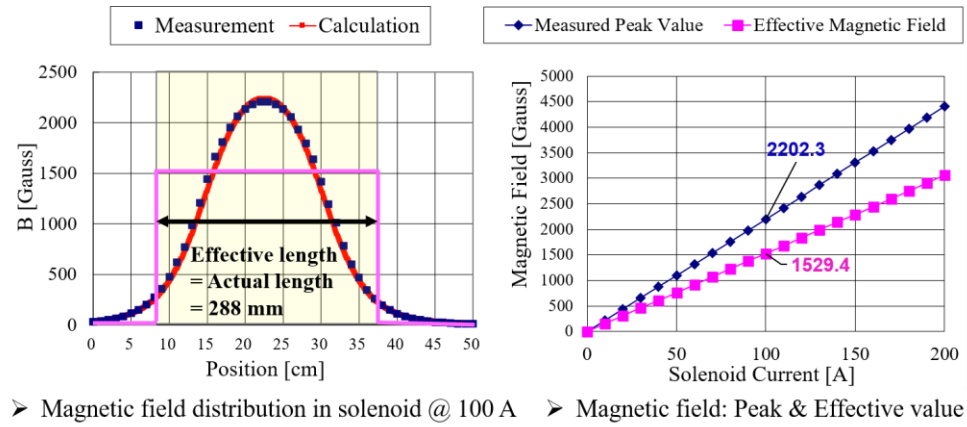

Figure 3. 13. Magnetic field distribution of the LEBT solenoid.

The solenoid magnet is exploited as a major focusing element in the proton injector. Protons show two different behaviors in a solenoid magnet – helical motion along the solenoid axis and focusing action near the edges of the solenoid where the magnetic field has a strong radial component. Figure 3.13 is a schematic diagram of the LEBT solenoid magnet and the magnetic field calculation results obtained in *POISSON/SUPERFISH* code [].

Figure 3.13 illustrates the axial magnetic field distribution of the LEBT solenoid magnet measured by a Hall effect sensor and comparison with calculated field distribution. The excitation curve is also measured by the same probe with compared with the calculations. The discrepancy between magnetic field calculation and measurement is less than 1% in both cases of the field distribution and the excitation curve. This solenoid can be approximated as a hard-edge model, which enables simple implementation to beam dynamics study. The effective length of the solenoid is calculated by:

$$l_{eff} \equiv \frac{1}{k_{peak}} \int_{-s_1}^{s_1} k(s) ds \tag{3.6}$$

In the similar way, the effective magnetic field is calculated by:

$$k_{eff} \equiv \frac{1}{l_{solenoid}} \int_{-s_1}^{s_1} k(s) ds \tag{3.7}$$

Above integration is performed in the range of 500 mm which includes fringe field outside the solenoid. Peak field is measured to be a 2202 G and the corresponding effective magnetic field is calculated as a 1529 G when current of 100 A flows in the solenoid coils and the actual length of solenoid is a 288 mm.

The linear equation of motion of charged particle beams in the focusing field, k(s), is described by Hill differential equation as:

$$x''(s) + k(s)x(s) = 0 \tag{3.8}$$

This second-order linear ordinary differential equation can be solved with the paraxial approximation which is a small-angle approximation. The general solution of the equation can be written as:

$$x(s) = x(0)\cos(s) + x'(0)\sin(s) \tag{3.9}$$

$$x'(s) = x(0)\cos'(s) + x'(0)\sin'(s) \tag{3.10}$$

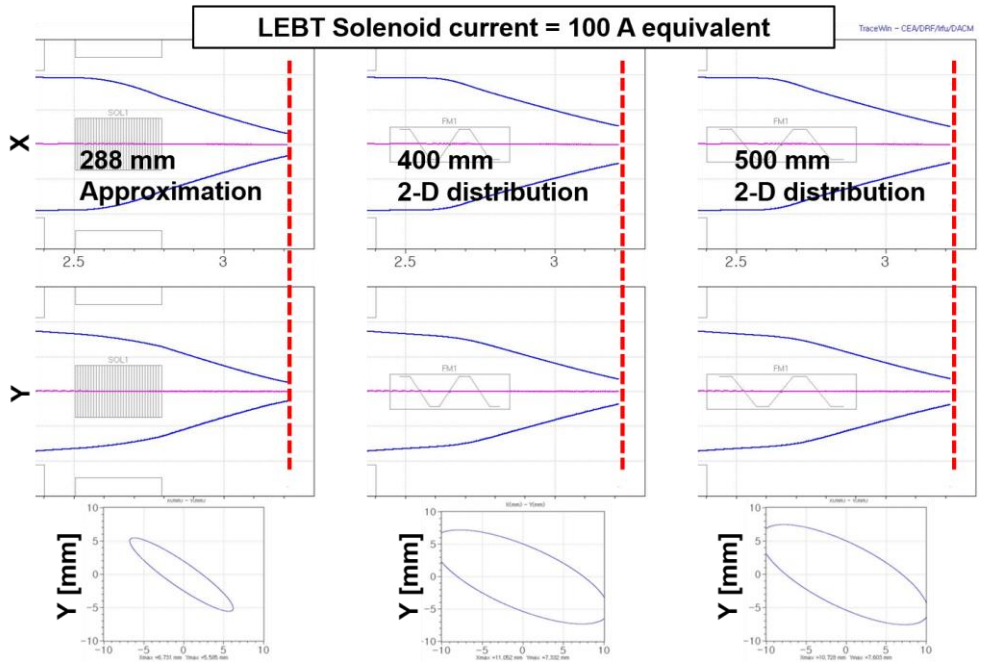

Figure 3. 14. Comparison of beam dynamics calculation depending on solenoid magnet model: hard-edge model, 2-D field map (400 mm dimension), and 2-D field map (500 mm dimension).

Table 3.2. Comparison of beam center and beam size according to solenoid magnet model.

B Field model	Center		Size	
	X	Y	X	Y
288 mm Hard-edge	-0.26	-0.07	3.24	2.76
400 mm 2-D Field map	-0.22	-0.08	**5.41**	**3.63**
500 mm 2-D Field map	-0.22	-0.08	**5.25**	**3.76**

In the low energy beamline, one of the most important phenomena is a strong focusing which can violate the paraxial approximation.

For more accurate beam dynamics study, therefore, two-

dimensional magnetic field distribution with azimuthal symmetry along the z-axis is calculated by the electromagnetic field analysis code and incorporated in beam dynamics simulation. Figure 3.14 and Table 3.2 show that hard-edge model overestimates a focusing strength in beam dynamics calculation, compared to the 2-D field map model.

.

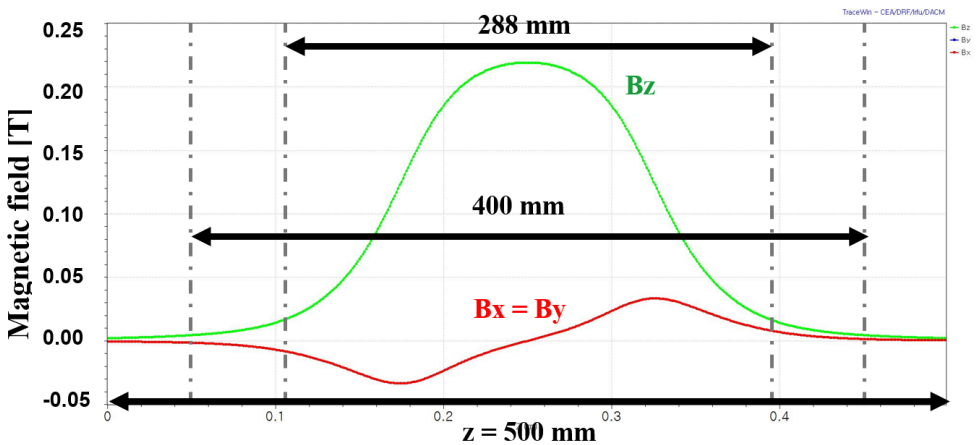

Figure 3. 15. Two-dimensional magnetic field map calculated by *Superfish/Poisson* code.

Axial and radial distribution of magnetic field calculated on the LEBT solenoid magnet is illustrated in Figure 3.15. Physical dimension of the solenoid magnet is 288 mm in length, and fringe field is stretched beyond the dimension.

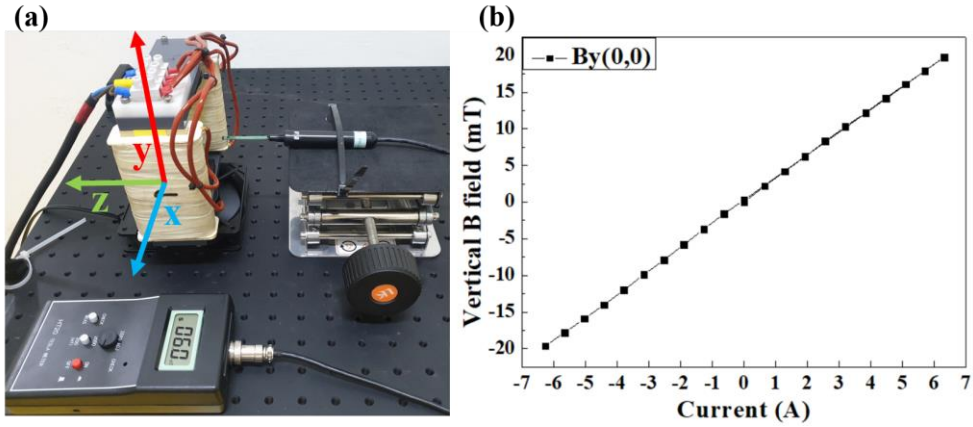

Figure 3. 16. (a) Magnetic field measurement, (b) measured excitation curve of magnetic steerer in the LEBT.

Figure 3.16 (a) is a schematic diagram of the steerer magnet and the result of magnetic field calculation, and Figure 3.16 (b) shows the excitation curve of the steerer magnet measured with a gauss meter. This magnetic steerer in the Figure 3.16 kicks the beam in the horizontal direction because magnetic field is exerted in the vertical direction, so called as x-steerer or horizontal steerer.

Beam centroid angle is typically changed by the magnetic steerer as:

$$x' = x' - \frac{qBL_y \cdot c}{mc^2 \beta\gamma} \quad \text{And} \quad y' = y' + \frac{qBL_x \cdot c}{mc^2 \beta\gamma} \tag{3.11}$$

where x’ and y’ is the horizontal and vertical beam centroid angle.

The fundamental design concept of low energy beam transport is pure-electrostatic LEBT or pure-magnetostatic LEBT in general. In the study, dipole bending magnet is installed right after the ion source and beam extraction system. Dipole bending magnet is itself focusing element, but normally weaker than a solenoid or an einzel lens. Total length of beam pipe

in the dipole is about 628 mm, which is not negligible drift length in LEBT.

In this context, an einzel lens is considered as a compact focusing element to reduce beam size before the bending magnet. The einzel lens is selected as commercially available product EL44-50 from *National Electrostatics Corporation (NEC)*. The lens has the aperture diameter of 44.5 mm, length along the beamline of 165 mm and electrode voltage rating of 50 kV. From these specifications, beam dynamics are simulated with electric potentials on the center electrode of an einzel lens as plotted in Figure 3.6. Calculated beam trajectories and beam transmission is not acceptable when initial beam current is 20 mA and beam emittance is $\varepsilon_{n,rms} = 0.2\ \pi \cdot mm \cdot mrad$.

Measured beam current or beam transmission is compared with calculation results as depicted in Figure 3.8. Beam transmission along the electric field shows a similar trend, but shows few discrepancy in beam current of the second monitor located downstream the bending magnet. It implies a worse beam loss near the einzel lens and the bending magnet than expected in simulation model. It may be related to un-neutralization or full space charge transport nearby the einzel lens, but neutralization is set zero only in the total length of the einzel lens on the beam dynamics simulation model. In conclusion, it can be seen that the einzel lens is not suitable for this structure, and it is generally difficult to add electrostatic components to a magnetostatic low energy beam transport system.

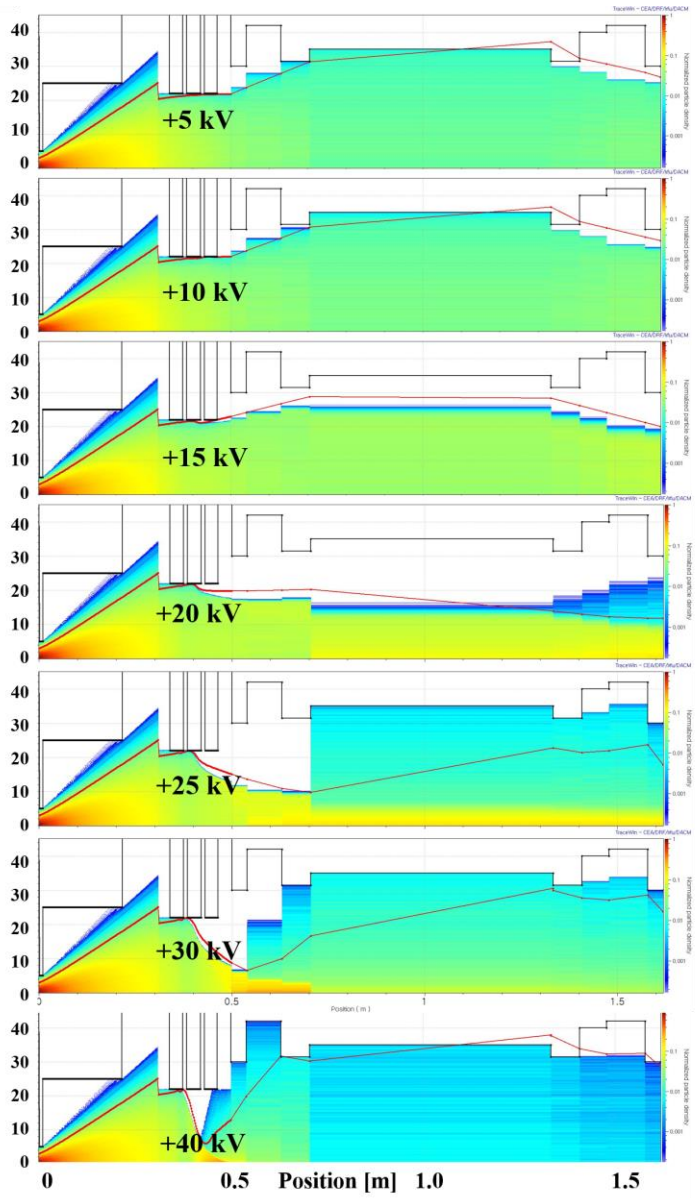

Figure 3. 17. Beam dynamics simulation according to the various Einzel lens voltages.

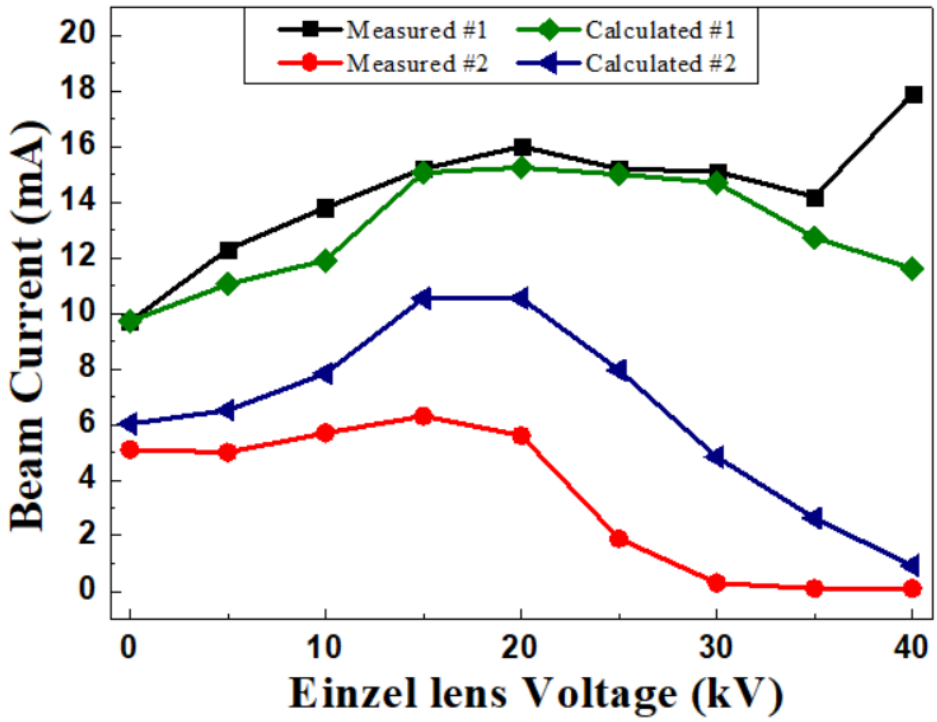

Figure 3. 18. Beam current depending on an Einzel lens voltage: measurement vs. calculation.

3.3. Low Energy Beam Diagnostics

A low-energy beam transport system is a system that transports a beam starting from the ion source from which the proton beam is formed and before a high-frequency accelerator, commonly referred to as RFQ. Controls the size of focusing the beam at the solenoid to achieve the beam conditions required by the high frequency accelerator, It consists of control of where the steerer bends the beam path, and diagnostics that measure whether this control has been done well.

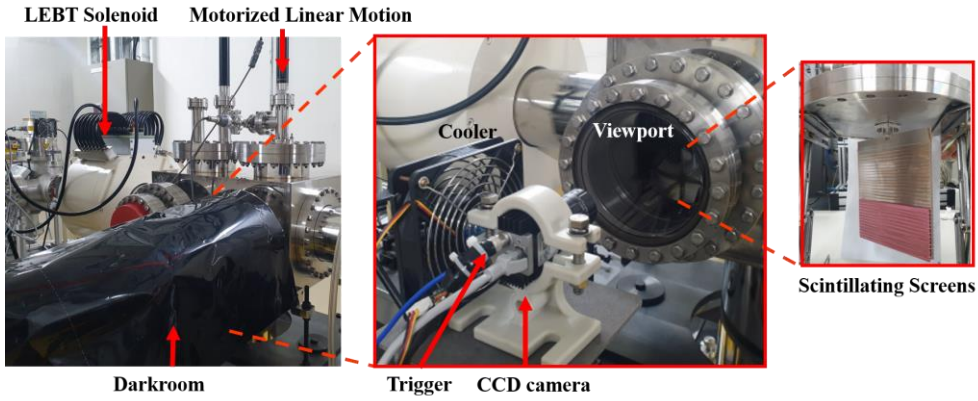

Figure 3. 19. Installation of scintillation screen and CCD cameras.

Among the beam diagnostics, a device that measures the two-dimensional distribution of a beam using a scintillation screen and a CCD is very simple and highly effective. This measuring device is used to measure transverse beam profile and emittance with solenoid scan method.

Image processing is performed by OpenCV as open-source code for computer vision technology. Image binarization, canny edge detection, blob detection, and ellipse fitting technique are utilized to analyze the captured beam images.

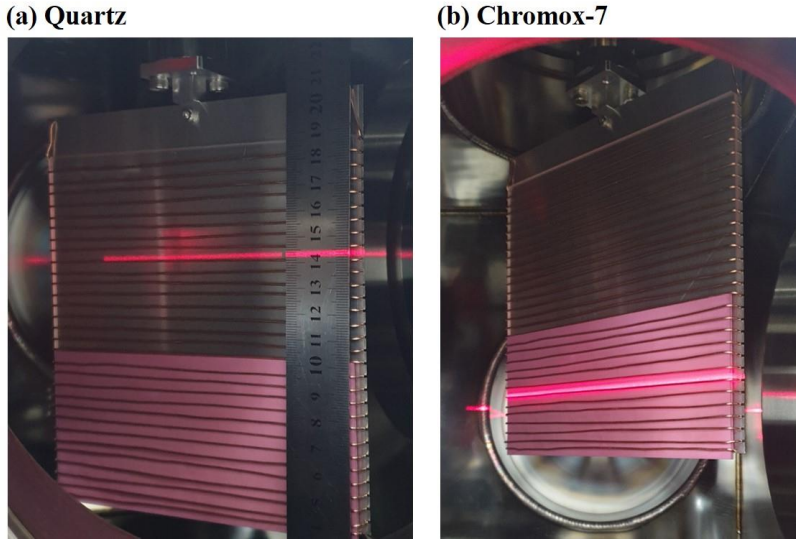

Figure 3. 20. Alignment of scintillating screen in a beamline

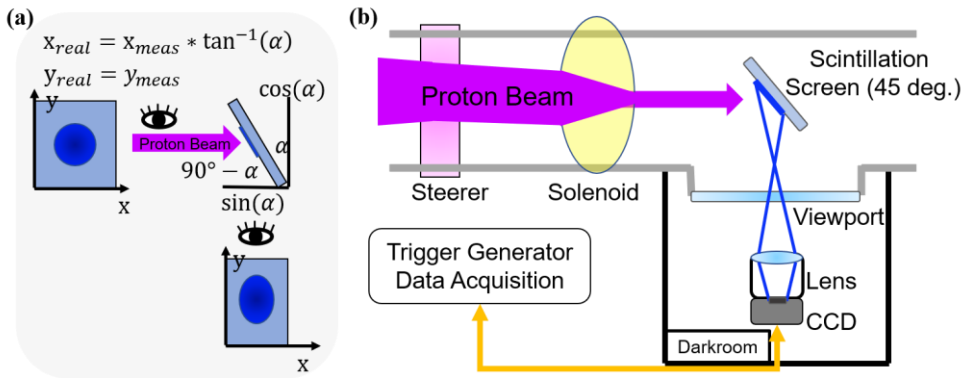

Figure 3. 21. Beam profile monitoring system with scintillating screen: (a) image distortion along the installed angle, (b) schematic diagram of the beam profile measurement.

Beam current monitors measure the intensity of the beam, but not the density distribution in the transverse direction. A beam profile monitor is used to measure the change in size and center position of a low energy beam transported from an ion source through the dipole bending magnet, the steerer magnets, and the solenoid magnet. The beam profile monitor in Figure 3.21 can obtain beam size and position by capturing the light emitted when the proton beam hits the scintillating screen directly. According to Figure 3.21 (a), there may be a difference between the actual image and the measured image depending on the angle at which the screen is installed with respect to the beamline axis and the relative installation position of the camera. Therefore, by installing it at an angle of 45 degrees in the horizontal direction with respect to the transverse plane of the beamline, the difference in the aspect ratio between the actual image and the measured image is not distorted.

Quartz glass and chrome-doped aluminum oxide, chromox-7 (Al2O3:Cr), are used for the scintillating screen. The two materials have

different sensitivity, generate light in different wavelength ranges, and have different decay times. Chromox-7 belongs to a scintillator with very good sensitivity, but it has the characteristic of saturation when the beam current is high. The proton injector generates a proton beam of 10 mA or more, and if this beam is focused at the screen position through a solenoid magnet, it is saturated and unable to measure the beam distribution. Therefore, it is suitable for use in a beam with relatively weak intensity like H2+ beam. Quartz glass has lower sensitivity than chromox-7, so it does not saturate even when the beam current density is high. Instead, in a solenoid magnet setting that is far from the focal length, the light intensity is not sufficient and repeated measurements are required. Since the scintillating screen method measures accumulated beam profile during the exposure time, it is difficult to observe the change of the beam over time such as dynamic process of space charge neutralization, compared to a electrical signal-based beam profile monitor. However, it satisfies the purpose of this study to measure beam properties in a steady-state where the beam properties is not so changed as DC beam or long pulse beam in the proton injector.

Table 3.3. Specification and setting conditions of vision camera used in beam profile monitor.

Model name	*Basler* acA640-120gc
Resolution	658 * 492 VGA GigE color
Pixel	5.6 μm * 5.6 μm
Sensor	1/4 CCD (3.68 mm * 2.75 mm)
Frame rate	120 fps (max.)
Exposure time	1 ms (variable)
Lens	*Computar* M2514-MP2 megapixel

A vision camera is used and its specifications and setting conditions

are summarized in Table 3.3. The frame rate is up to 120 fps, but since the repetition rate of operation is typically set as 1-10 Hz, a pulse delay generator is used to synchronize a camera trigger with a beam trigger. The image is focused with the center of the screen by manually adjusting the lens, and the exposure time and gain are adjusted to obtain an image under the condition of obtaining enough signal-to-noise ratio.

Chapter 4. Beam Emittance Measurement and Mitigation of Emittance Growth

For high-current beams at low kinetic energies, the space charge effect must be carefully taken into account. The space charge effect fundamentally defocuses beam and the nonlinear terms cause an unwanted increase in emittance, so called emittance growth. Self-neutralization regime that reduces the space charge effect by artificially injecting residual gas is used to suppress the emittance growth. This effect can be accurately predicted by numerically calculating the residual gas distribution and beam dynamics.

To verify the self-neutralization effect and experimentally find the gas injection conditions that most effectively suppress the emittance growth, beam emittance is measured under several conditions.

4.1. Space Charge Effect and Self-Neutralization

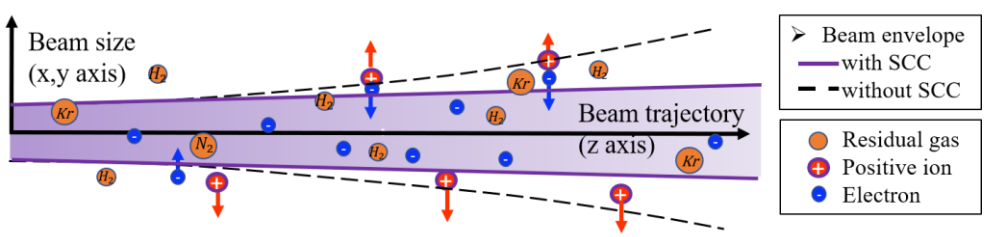

Figure 4. 1. Self-neutralization induced by ionization of charged particles beam with residual gases.

In the low energy section of beam transport, a high current beam is space charge dominated. This nonlinear force can cause a large emittance growth which is irreversible and unfavorable to the beam transmission into

the radio-frequency quadrupole. Fortunately, space charge effect can be naturally reduced by ionization of residual gases during beam transport, and it is so-called self-neutralization.

Beam-residual gas collisions are divided into two major reactions – ionization and charge exchange. Ionization may help self-neutralization by producing electrons that compensate positive ion beam potential. On the other side, charge exchange may lead beam loss and halo formation.

$$\text{(ionization) } H^+ + X^0 \rightarrow H^+ + X^+ + e^- \tag{4.1}$$

$$\text{(charge exchange) } H^+ + X^0 \rightarrow H^0 + X^+ \tag{4.2}$$

Assuming a beamline is occupied by residual gases – Nitrogen from atmosphere, Hydrogen from an ion source, and Krypton as intentionally injected, list of possible reactions is written in Table 4.1. The cross-section of 50 keV proton beam with residual gas, obtained by previous works [41-43], is summarized in table 4.2.

Table 4.1. List of reactions of proton beam with residual gases: Nitrogen, Hydrogen and Krypton.

(1) $\boldsymbol{H^+ + H_2 \rightarrow H^+ + H_2}$
(2) $\boldsymbol{H^+ + Kr \rightarrow H^+ + Kr}$
(3) $H^+ + N_2 \rightarrow H^+ + N_2$
(4) $\boldsymbol{H^+ + H_2 \rightarrow H^+ + H_2^+ + e^-}$
(5) $\boldsymbol{H^+ + Kr \rightarrow H^+ + Kr^+ + e^-}$
(6) $H^+ + N_2 \rightarrow H^+ + N_2^+ + e^-$
(7) $H^+ + H^+ \rightarrow H^+ + H^+$
(8) $H^+ + H \rightarrow H^+ + H$
(9) $H^+ + H_2 \rightarrow H^+ + H_2$*

(10)	$H^+ + Kr^+ \rightarrow H^+ + Kr^+$
(11)	$H^+ + Kr \rightarrow H^+ + Kr^*$
(12)	$H^+ + e^- \rightarrow H^+ + e^-$

Table 4.2. Collisional cross-section of 50 keV proton with residual gases

Cross-section of 50 keV H+ with residual gas [$10^{-20} m^2$]	Hydrogen	Nitrogen	Krypton
Ionization	1.8	5.0	7.2
Charge Exchange	1.3	2.7	4.5

The potential well on the beam axis created by a uniform beam without any space charge neutralization is expressed as:

$$\phi(r) = \begin{cases} \Delta\phi \left[1 - \dfrac{r^2}{r_{beam}^2} + 2\ln\left(\dfrac{r_{beam}}{r_{pipe}}\right)\right] & for\ r \le r_{beam}, \\ \Delta\phi\ 2\ln\left(\dfrac{r}{r_{pipe}}\right) & for\ r_{beam} \le r \le r_{pipe} \end{cases} \quad (4.3)$$

$$\text{where, } \Delta\phi = \frac{I}{4\pi\epsilon_0 v} \quad (4.4)$$

In steady-state, the neutralization factor f_e can be calculated with Gabovich's derivations for the space charge potential [44-46]:

$$(\Delta\varphi_{neut})^2 = 3\mathcal{L}\frac{m_b}{m_e}\frac{\Phi_i}{U_0}\ \frac{n_b q e^2}{(4\pi\epsilon_0)^2}\left(\frac{q}{n_0\sigma_e} + \frac{v_b\sigma_i r_b}{2\bar{v}_i\sigma_e}\right) \quad (4.5)$$

$$f_e = 1 - \frac{\Delta\varphi_{neut}}{\Delta\varphi_{full}} \tag{4.6}$$

where the ionization energy of the gas molecules $e\Phi_i$, source voltage U_0, and coulomb logarithm $\mathcal{L}$:

$$\mathcal{L} = \ln\left(4\pi\epsilon_0^{\frac{3}{2}}\frac{m_e^{\frac{3}{2}}v_b^3}{qe^3n_e^{\frac{1}{2}}}\right) \tag{4.8}$$

$$n_e = qn_b + \frac{n_b v_b n_0 \sigma_i r_b}{2\bar{v}_i} \tag{4.7}$$

$$\Delta\varphi_{full} = \frac{I_b}{4\pi\epsilon_0 v_b} \tag{4.9}$$

Beam-residual gas collisional cross-section is written as:

$$\sigma_e \approx \sigma_{ionization} \tag{4.10}$$

$$\sigma_i \approx (\sigma_{ionization} + \sigma_{charge-exchange}) \tag{4.11}$$

This formula also requires residual gas density and beam size to obtain neutralization factor along the beamline. Residual gas density can be measured by pressure monitors and be estimated by numerical simulation. Beam size can be measured in some position, as well as numerically analyzed by beam dynamics simulation.

Another important aspect is the time constant written as:

$$t_{SCC} = \left(\sigma_{ioniz} \cdot n_g \cdot v\right)^{-1} \tag{4.12}$$

The characteristics time for the self-neutralization is relevant to the minimum time needed for the space charge neutralization to trap enough electrons and reach a steady state equilibrium. Before the steady state, beam transport keeps changing and shows transient characteristics as well. Previous experiments have proven that it is almost impossible to reach 100% full neutralization and zero space charge potential [45].

4.2. Numerical Analysis on Residual Gas Molecules

MolFlow+ is a Monte-Carlo code that numerically calculate the steady-state pressure in an arbitrarily complex geometry. The name comes from molecular flow, the condition when the mean free path of molecules is so long compared to the geometry size that collisions can be neglected [47].

Major inputs of this program are a geometry, outgassing factors and pumping speed of a vacuum system. Geometries can be imported from most CAD programs that support the STL file format. It is important to tune a CAD model to successfully import in Molflow+ code without geometrical error which is related to severe particle losses in undefined region.

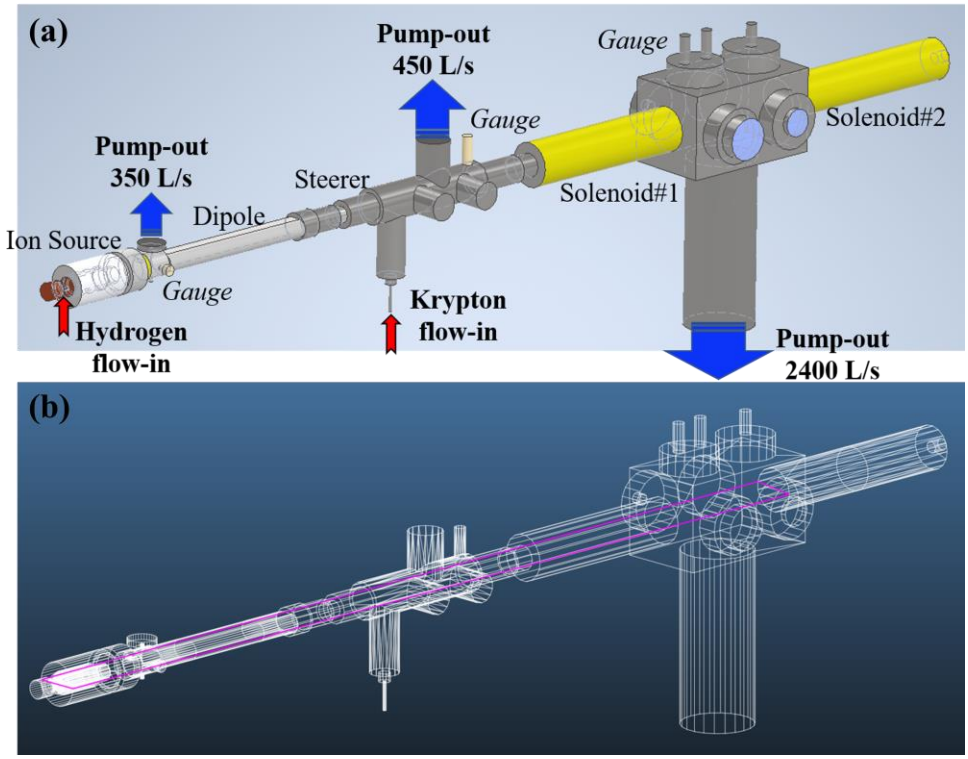

Figure 4. 2. Drawings of vacuum system of proton injector test stand in CAD and Molflow+ program.

Figure 4.2 (a) is simplified three-dimensional CAD model of the proton injector test stand and Figure 4.2 (b) is imported version of geometry file in the program. Instead of detailed design drawings such as vacuum flanges and sealing, drawings for empty spaces where gas molecules can exist in the vacuum system must be prepared separately. It is converted into a combination of vertices and facets in Molflow+ by exporting as a binary file with appropriate resolution.

Outgassing rates of water vapour from unbaked metal alloys are tabulated in some papers [48] and used as a dominant factor in analysis.

$$q_{H_2O} \approx \frac{3 \times 10^{-9}}{t\,[hr]} \left[\frac{mbar}{s}\ \frac{\mathrm{l}}{cm^2}\right] \tag{4.13}$$

Assuming fixed time point after 30 hours of high-vacuum pumping and un-baked system, outgassing rate is calculated as:

$$q_{30hours} \approx 1 \times 10^{-10} \left[\frac{mbar}{s} \ \frac{\mathrm{l}}{cm^2}\right] \tag{4.14}$$

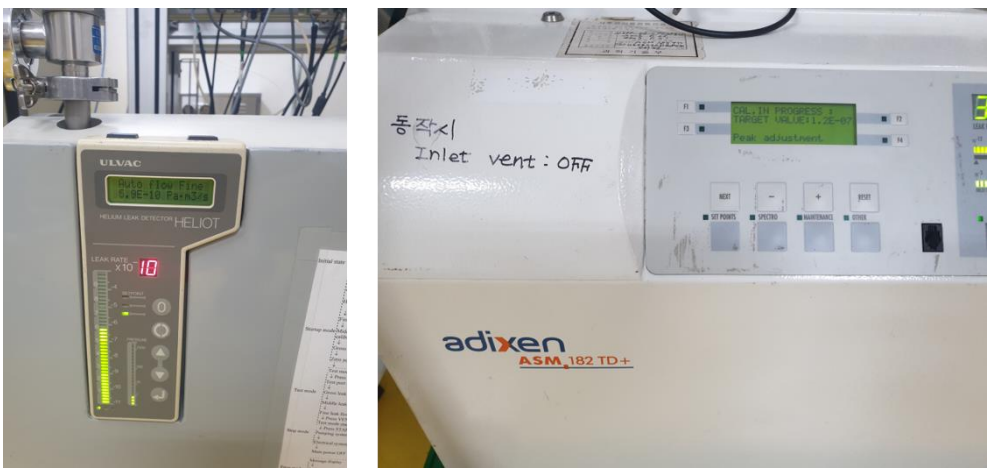

Figure 4. 3. Helium leak detection for assessment of leak rates on vacuum joints or vacuum bodies.

In addition to outgassing, parts that can be suspected of actual leaks such as vacuum joints, vacuum sealing, and welding parts are checked using a helium leak detector, and the leak rate of each part is measured to be low enough to be suitable for use.

Base pressure of the system is simulated to correlate assumed outgassing factors and effective pumping speed with the measured pressure. Typically, vacuum pressure is lower that $1.0 \times 10^{7}\ Torr$ after 30 hours of a high-vacuum pumping in the LEBT, as illustrated in Figure 4.3. As a further investigation, the correlation between various hydrogen gas flow rates and pressures indicated at the vacuum gauges can be used to find

unknown leak rate near the ion source.

The microwave ion source in the test stand typically operates with hydrogen flow rate of the 2.0 sccm. During this condition, hydrogen pressure in the LEBT diagnostics chamber is indicated as $2.6 \times 10^4\ Torr$ by the diffusion of hydrogen gases. In this case, partial pressure in the beam pipe after the extractor and suppressor is near the $4.5 \times 10^4\ Torr$. This is not desirable vacuum condition in LEBT since the pressure is 10 times higher than the nominal LEBT. In this context, another vacuum port is designed to improve vacuum pumping in the LEBT based on the numerical analysis. Simulation shows that additional turbo-molecular pumping of 450 l/s as pumping speed should be added between main vacuum chamber and bending magnet in the LEBT. As a result, hydrogen pressure in the LEBT and in the beam extractor is reduced up to $1.7 \times 10^5\ Torr$ and $1.3 \times 10^4\ Torr$ by the designed differential pumping regime.

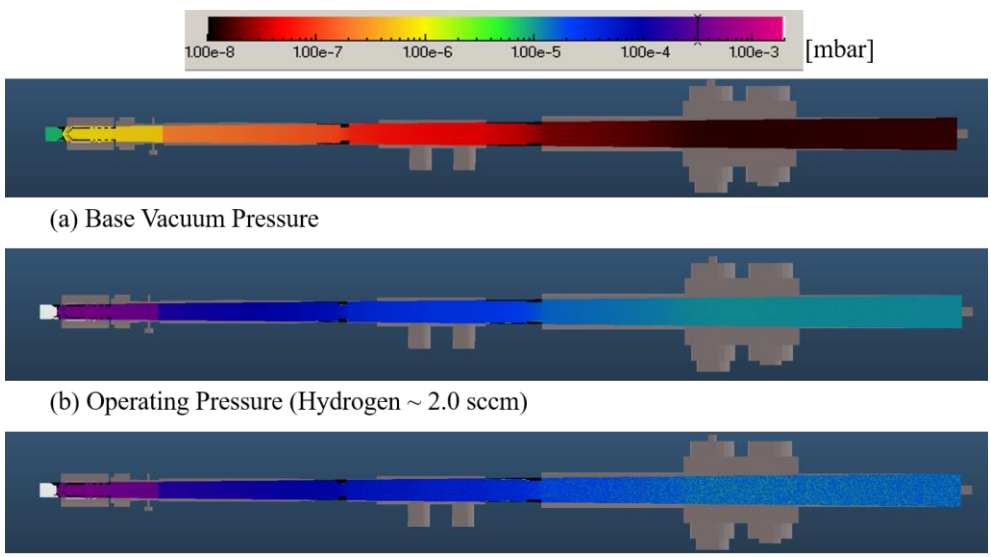

(a) Base Vacuum Pressure

(b) Operating Pressure (Hydrogen ~ 2.0 sccm)

(c) Operating Pressure (Hydrogen ~ 2.0 sccm and Krypton ~ 0.9 sccm)

Figure 4. 4. Calculated pressure distribution: (a) base vacuum condition, (b) operating condition (Hydrogen flow rate = 2.0 sccm), and (c) operating condition with additional residual gas (Hydrogen flow rate = 2.0

sccm and Krypton flow rate = 0.9 sccm).

For an improved vacuum system using a differential pump, the distribution of partial pressure is numerically calculated for the base vacuum condition, the beam experiment condition, and the krypton additional injection condition, as illustrated in Figure 4.4.

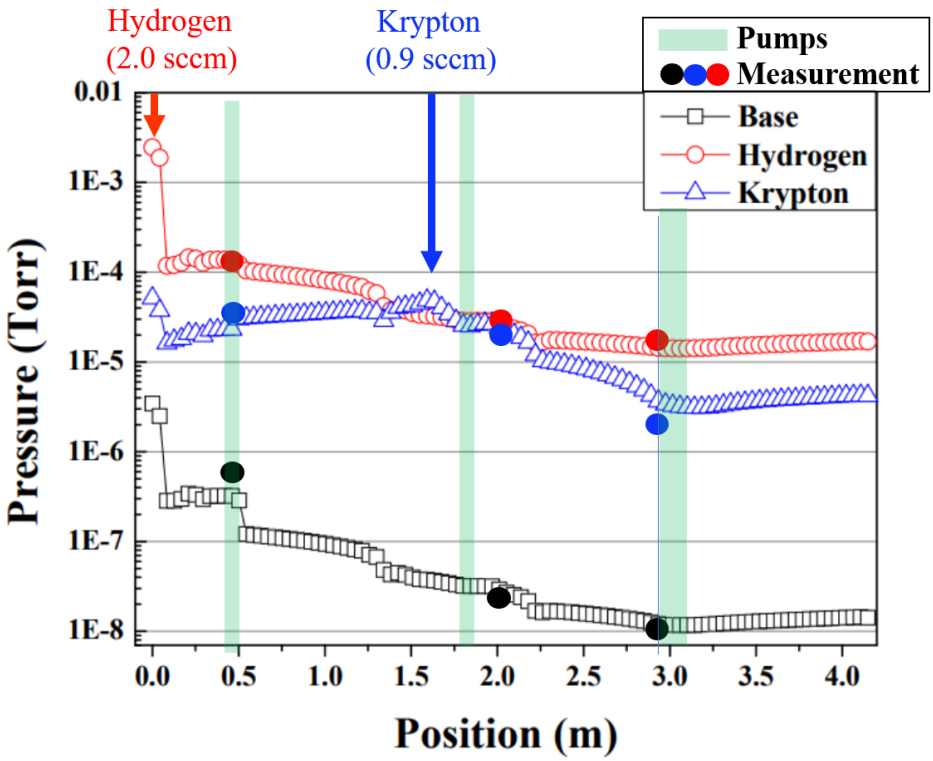

Figure 4. 5. Partial pressure distribution and measured pressure at the three monitoring positions: base vacuum (Air), hydrogen and krypton.

Figure 4.5 shows the pressure distribution in the beam propagation direction. Position indicates the distance to the beam direction with respect to the plasma chamber. First, in the case of an ion source, it has the relatively highest base pressure. Because it is composed of many in-vacuum parts, it is the area where outgassing, which is a surface phenomenon,

occurs the most. It has a narrower flow path compared to general beamline parts with a wide inner diameter and a simple structure, so the low vacuum conductance also explains the reason for the high base pressure. Since the electrode aperture, which is the outer boundary of the ion source, acts as an orifice on the vacuum side, a pressure difference of more than 10 times is expected. For a typical injection of 2.0 sccm of hydrogen for plasma discharge, the partial pressure of hydrogen at the ion source is estimated to be 2.5 mTorr. Since the downstream area of the ion source is composed of a beampipe with a wide inner diameter, there is no large pressure difference. Of course, in the low energy beam transport area, although the vacuum conductance is high, the pressure around the pump is low and the pressure is high near the gas injection line.

Most of vacuum gauges measure physical property like thermal conductivity, viscosity, or number density. Sensitivity to these properties may not be the same for different gas species. Commercially available gauge is usually calibrated for measurement of nitrogen, the most common gas species. To know accurate gas pressure, indicated value on gauge controller is corrected by using gas correction factor.

Ultimate pressure in equilibrated base vacuum is lower than 1.4% of the hydrogen pressure at normally operating condition in the proton injector test stand. This portion may be lower than sensing error of commercial gauges, so that it is generally acceptable that gauge value is almost the same with hydrogen gas pressure divided by gas correction factor without additional gas injection. In case of Krypton gas injection, gauge indicate mixed pressure value, which should be subtracted and corrected from hydrogen-only base pressure. In this way, actual partial pressure considering gas correction factor is described in Table 4.3.

Table 4.3. Gas correction factors.

Gas type	Air/Nitrogen	Oxygen	Water	Hydrogen	Krypton
Correction Factor	1	1	0.91	2.17	0.53

Table 4.4. Indicated values in cold cathode gauges (Calibrated to Nitrogen) along the hydrogen flow rate.

	Indicated value at cold cathode gauges [Torr] **Calculated Hydrogen gas pressure [Torr]**		
Hydrogen flow rate [sccm]	Ion source	LEBT1	LEBT2
Ultimate vacuum	6.50E-07	2.30E-08	1.00E-08
0	-	-	-
	4.26E-05	1.00E-05	7.60E-06
1.6	**9.11E-05**	**2.17E-05**	**1.65E-05**
	5.23E-05	1.10E-05	8.60E-06
1.8	**1.13E-04**	**2.39E-05**	**1.87E-05**
	6.28E-05	1.40E-05	1.10E-05
2.0	**1.36E-04**	**3.04E-05**	**2.39E-05**

Table 4.5. Indicated values in cold cathode gauges (Calibrated to Nitrogen) along the krypton flow rate.

	Indicated value at cold cathode gauges [Torr] **Calculated Krypton gas pressure [Torr]**		
Krypton flow rate [sccm]	Ion source	LEBT1	LEBT2
	6.28E-05	1.40E-05	1.10E-05
0.00	-	-	-
	8.90E-05	2.70E-05	1.20E-05
0.30	**1.38E-05**	**6.89E-06**	**5.30E-07**
	1.14E-04	3.70E-05	1.40E-05
0.60	**2.70E-05**	**1.22E-05**	**1.59E-06**
	1.35E-04	4.70E-05	1.50E-05
0.90	**3.82E-05**	**1.75E-05**	**2.12E-06**

	1.60E-04	5.80E-05	1.60E-05
1.20	**5.14E-05**	**2.33E-05**	**2.65E-06**
	1.81E-04	6.80E-05	1.70E-05
1.50	**6.25E-05**	**2.86E-05**	**3.18E-06**
	2.10E-04	8.00E-05	1.90E-05
1.80	**7.79E-05**	**3.50E-05**	**4.24E-06**
	2.51E-04	9.80E-05	2.10E-05
2.10	**9.96E-05**	**4.45E-05**	**5.30E-06**

Table 4.4 and Table 4.5 show the values indicated by the pressure gauge when hydrogen and krypton are injected, respectively, and the data converted to actual partial pressure by correcting this with a gas correction factor.

Actual pressure measurement was performed at ion source side pressure gauge #1 located near z=0.45 m, LEBT side pressure gauge #2 located near z=2.0 m, and LEBT diagnostics pressure gauge #3 located near z=2.8. In Gauge#1 and Gauge#2, the difference between the measured value and the calculated value is less than 10%, which is the error range of the gauge itself. At Gauge #3, the Krypton pressure was measured to be about 30% lower than the calculated value. It is estimated that the 2400 l/s pump located near z=3 has better exhaust performance for krypton than expected, but this area has little effect on the emittance growth measurement, so it is not seriously considered.

4.3. Transverse Beam Emittance Measurement with Solenoid Scan Method

The second order moments of the beam can be estimated at the first focusing element used for the scan by varying the focusing strength or varying relative position between a magnet and a beam detector [49].

In the limited space of low energy beam transport section, at a fixed

position of measurement, focusing strength is increasingly varied to control the beam size from under-focus to over-focus including a beam waist.

As described in section 2.3, beam transport from a point 0 to a point 1 can be solved by the following matrix multiplication.

$$\sigma = \begin{pmatrix} < x^2 > & < xx' > \\ < xx' > & < x'^2 > \end{pmatrix} = R\sigma_0 R^T \tag{4.15}$$

where the beam matrix at point 0 and point 1 is $\boldsymbol{\sigma_0}$ and $\boldsymbol{\sigma}$, respectively, and the transfer matrix of element between two points is expressed as R.
Thin lens approximation gives,

$$\mathrm{R} = \mathrm{FS} = \begin{pmatrix} S_{11} + KS_{12} & S_{12} \\ S_{21} + KS_{22} & S_{22} \end{pmatrix} \tag{4.16}$$

where,

$$F = \begin{pmatrix} 1 & 0 \\ K & 1 \end{pmatrix}, \quad K = \frac{1}{f_{sol}} = \int \left(\frac{eB_s}{2p}\right)^2 ds \quad , \quad \mathrm{S} = \begin{pmatrix} 1 & L \\ 0 & 1 \end{pmatrix}$$

$$\begin{aligned} < x^2 > \; &= \left(S_{11}^2\sigma_{11_0} + 2S_{11}S_{12}\sigma_{12_0} + S_{12}^2\sigma_{22_0}\right) \\ &\quad + \left(2S_{11}S_{12}\sigma_{11_0} + 2S_{12}^2\sigma_{12_0}\right)K \\ &\quad + S_{12}^2\sigma_{11_0}K^2 \\ = \mathrm{A}(\mathrm{K} - \mathrm{B})^2 + C &= AK^2 - 2ABK + (C + AB^2) \\ &= P_1K^2 + P_2K + P_3 \end{aligned} \tag{4.17}$$

$$\varepsilon_x = \sqrt{\det(\sigma)} = \sqrt{\sigma_{22} - \sigma_{12}^2} = \frac{\sqrt{AC}}{S_{12}^2} = \frac{\sqrt{P_1 P_3 - P_2^2}}{S_{12}^2} \tag{4.18}$$

On the other hand, when the thin-lens approximation is not applicable, 4-dimensional beam matrix can be solved as:

$$\sigma^{4D} = \begin{pmatrix} < x^2 > & < xx' > & < xy > & < xy' > \\ < xx' > & < x'^2 > & < x'y > & < x'y' > \\ < xy > & < x'y > & < y'^2 > & < yy' > \\ < xy' > & < x'y' > & < yy' > & < y'^2 > \end{pmatrix} \tag{4.19}$$

$$R = \begin{pmatrix} R_{11} & R_{12} & R_{13} & R_{14} \\ R_{21} & R_{22} & R_{23} & R_{24} \\ R_{31} & R_{32} & R_{33} & R_{34} \\ R_{41} & R_{42} & R_{43} & R_{44} \end{pmatrix} = \begin{pmatrix} R_{xx} & R_{xy} \\ R_{xy} & R_{yy} \end{pmatrix} \tag{4.20}$$

Transfer beam matrix for the hard edge Solenoid model:

$$R_{xx} = R_{yy} = \begin{pmatrix} \cos^2(kl) & \sin(kl)\cos(kl)/k \\ -k\sin(kl)\cos(kl) & \cos^2(kl) \end{pmatrix} \tag{4.21}$$

$$R_{xy} = -R_{yx} = \begin{pmatrix} \sin(kl)\cos(kl) & \sin^2(kl)/k \\ -k\sin^2(kl) & \sin(kl)\cos(kl) \end{pmatrix} \tag{4.22}$$

$$R_{zz} = \begin{pmatrix} 1 & l/\gamma^2 \\ 0 & 1 \end{pmatrix} \tag{4.23}$$

$$M^{4D} = D^{4D} \cdot R^{4D} = \begin{pmatrix} M_{xx} & M_{xy} \\ M_{yx} & M_{yy} \end{pmatrix} = \begin{pmatrix} m_{11} & m_{12} & m_{13} & m_{14} \\ m_{21} & m_{22} & m_{23} & m_{24} \\ m_{31} & m_{32} & m_{33} & m_{34} \\ m_{41} & m_{42} & m_{43} & m_{44} \end{pmatrix} \quad (4.24)$$

where $D = \begin{pmatrix} 1 & l \\ 0 & 1 \end{pmatrix}$: $Drift\ matrix\ in\ 2D\ \text{phase space}$

$$R^{4D} = \begin{pmatrix} R_{xx} & R_{xy} \\ R_{yx} & R_{yy} \end{pmatrix} \quad (4.25)$$

$$R^{4D} = \begin{pmatrix} R_{xx} & R_{xy} \\ R_{yx} & R_{yy} \end{pmatrix} : Solenoid\ matrix\ in\ 4D\ \text{phase space} \quad (4.26)$$

$$D^{4D} = \begin{pmatrix} D & 0 \\ 0 & D \end{pmatrix} : Drift\ matrix\ in\ 4D\ \text{phase space} \quad (4.27)$$

$$\sigma_0^{4D} = \begin{pmatrix} \sigma_{0,xx} & \sigma_{0,xy} \\ \sigma_{0,yx} & \sigma_{0,yy} \end{pmatrix} = \begin{pmatrix} \sigma_{0,11} & \sigma_{0,12} & \sigma_{0,13} & \sigma_{0,14} \\ \sigma_{0,21} & \sigma_{0,22} & \sigma_{0,23} & \sigma_{0,24} \\ \sigma_{0,31} & \sigma_{0,32} & \sigma_{0,33} & \sigma_{0,34} \\ \sigma_{0,41} & \sigma_{0,42} & \sigma_{0,43} & \sigma_{0,44} \end{pmatrix} \quad (4.28)$$

$$\sigma_{0,xx} = \begin{pmatrix} < x^2 > & < x'x > \\ < xx' > & < x'^2 > \end{pmatrix} = \epsilon_{0,x} \cdot \begin{pmatrix} \beta_{0,x} & -\alpha_{0,x} \\ -\alpha_{0,x} & \gamma_{0,x} \end{pmatrix} \quad (4.29)$$

$$\sigma_{0,yy} = \begin{pmatrix} < y^2 > & < y'y > \\ < yy' > & < y'^2 > \end{pmatrix} = \epsilon_{0,y} \cdot \begin{pmatrix} \beta_{0,y} & -\alpha_{0,y} \\ -\alpha_{0,y} & \gamma_{0,y} \end{pmatrix} \quad (4.30)$$

Initially x and y is decoupled before the first solenoid element.

$$\sigma_{0,xy} = \sigma_{0,yx} = \begin{pmatrix} 0 & 0 \\ 0 & 0 \end{pmatrix} \tag{4.31}$$

$$\sigma_1^{4D} = M^{4D} \cdot \sigma_0^{4D} \cdot M^{4D^T} =$$

$$\begin{pmatrix} m_{11} & m_{12} & m_{13} & m_{14} \\ m_{21} & m_{22} & m_{23} & m_{24} \\ m_{31} & m_{32} & m_{33} & m_{34} \\ m_{41} & m_{42} & m_{43} & m_{44} \end{pmatrix} \cdot \begin{pmatrix} \sigma_{0,11} & \sigma_{0,12} & \sigma_{0,13} & \sigma_{0,14} \\ \sigma_{0,21} & \sigma_{0,22} & \sigma_{0,23} & \sigma_{0,24} \\ \sigma_{0,31} & \sigma_{0,32} & \sigma_{0,33} & \sigma_{0,34} \\ \sigma_{0,41} & \sigma_{0,42} & \sigma_{0,43} & \sigma_{0,44} \end{pmatrix} \cdot M^{4D^T} \tag{4.32}$$

Letting $\delta_{ab} = \sum_{i=1}^{4} m_{ai}\sigma_{0,ib}$,

$$\sigma_1^{4D} = \begin{pmatrix} \delta_{11} & \delta_{12} & \delta_{13} & \delta_{14} \\ \delta_{21} & \delta_{22} & \delta_{23} & \delta_{24} \\ \delta_{31} & \delta_{32} & \delta_{33} & \delta_{34} \\ \delta_{31} & \delta_{42} & \delta_{43} & \delta_{44} \end{pmatrix} \cdot \begin{pmatrix} m_{11} & m_{21} & m_{31} & m_{41} \\ m_{12} & m_{22} & m_{32} & m_{42} \\ m_{13} & m_{23} & m_{33} & m_{43} \\ m_{14} & m_{24} & m_{34} & m_{44} \end{pmatrix} \tag{4.33}$$

$$\sigma_{1,ab}^{4D} = \sum_{j=1}^{4} \delta_{aj} m_{bj} = \sum_{j=1}^{4} \left(\sum_{i=1}^{4} m_{ai}\sigma_{0,ij} \right) \cdot m_{bj} \tag{4.34}$$

$$x_{rms}^2 = \sigma_{1,11}^{4D} = \left(m_{11}^2\sigma_{0,11} + 2m_{11}m_{12}\sigma_{0,12} + m_{12}^2\sigma_{0,22}\right) + \left(m_{13}^2\sigma_{0,33} + 2m_{13}m_{14}\sigma_{0,34} + m_{14}^2\sigma_{0,44}\right) \tag{4.35}$$

$$y_{rms}^2 = \sigma_{1,33}^{4D} = \left(m_{31}^2\sigma_{0,11} + 2m_{31}m_{32}\sigma_{0,12} + m_{32}^2\sigma_{0,22}\right) + \left(m_{33}^2\sigma_{0,33} + 2m_{33}m_{34}\sigma_{0,34} + m_{34}^2\sigma_{0,44}\right) \tag{4.36}$$

$$\begin{pmatrix} y^2_{rms,1} \\ y^2_{rms,2} \\ \vdots \\ y^2_{rms,n} \end{pmatrix} = \begin{pmatrix} m^2_{31,1} & 2m_{31,1}m_{32,1} & m^2_{32,1} & m^2_{33,1} & 2m_{33,1}m_{34,1} & m^2_{34,1} \\ m^2_{31,2} & 2m_{31,2}m_{32,2} & m^2_{32,2} & m^2_{33,2} & 2m_{33,2}m_{34,2} & m^2_{34,2} \\ & \vdots & & \vdots & \vdots & \\ m^2_{31,n} & 2m_{31,n}m_{32,n} & m^2_{32,n} & m^2_{33,n} & 2m_{33,n}m_{34,n} & m^2_{34,n} \end{pmatrix} \cdot \begin{pmatrix} \sigma_{0,11} \\ \sigma_{0,12} \\ \sigma_{0,22} \\ \sigma_{0,33} \\ \sigma_{0,34} \\ \sigma_{0,44} \end{pmatrix} \quad (4.37)$$

$$\text{where, } \begin{pmatrix} \sigma_{0,11} \\ \sigma_{0,12} \\ \sigma_{0,22} \\ \sigma_{0,33} \\ \sigma_{0,34} \\ \sigma_{0,44} \end{pmatrix} = \begin{pmatrix} \epsilon_{0,x}\beta_{0,x} \\ -\epsilon_{0,x}\alpha_{0,x} \\ \epsilon_{0,x}\gamma_{0,x} \\ \epsilon_{0,y}\beta_{0,y} \\ -\epsilon_{0,y}\alpha_{0,y} \\ \epsilon_{0,y}\gamma_{0,y} \end{pmatrix} \quad (4.38)$$

$$\sigma_{0,11}\sigma_{0,22} - \sigma^2_{0,12} = \epsilon^2_{0,x}\left(\beta_{0,x}\gamma_{0,x} - \alpha^2_{0,x}\right) = \epsilon^2_{0,x} \quad (4.39)$$

The derived formula from matrix multiplication with beam matrix and transfer matrix is implemented and solved by the least square method as multi-variate linear regression.

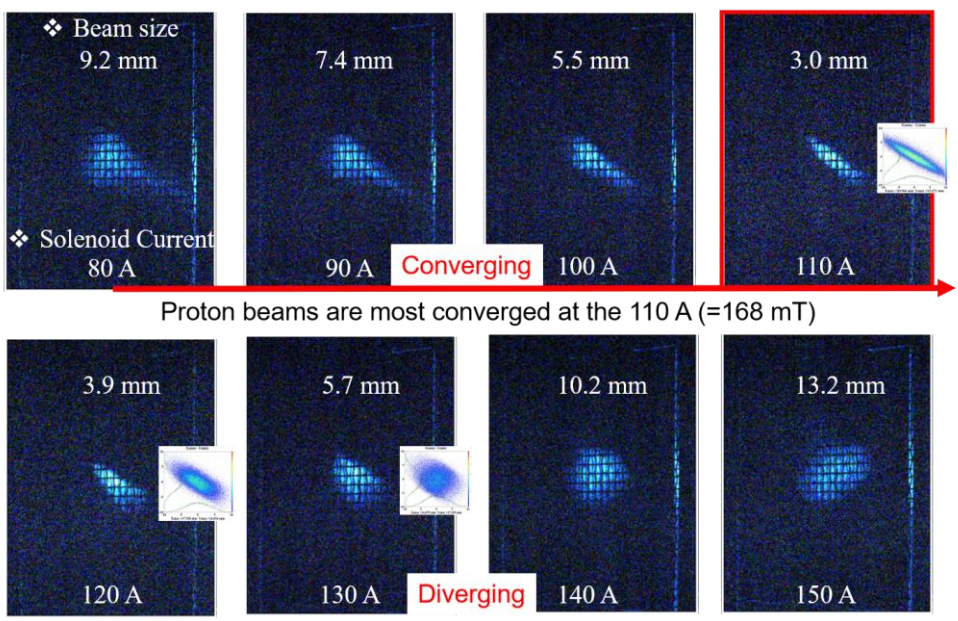

Figure 4. 6. Transverse beam profile during a solenoid scan.

Figure 4.6 is raw image data representing beam profile during a solenoid scan. These images are used to estimate the transverse beam emittance by analyzing the size by openCV and python code and inputting it into the measurement term of the least square formula derived from the beam matrix and transfer matrix.

4.4. Mitigation of Emittance Growth by Enhanced Self-Neutralization

Combining the formulas for self-neutralization and measuring and calculating the residual gas density distribution and beam envelope, mitigation of emittance growth by improved self-neutralization can be confirmed.

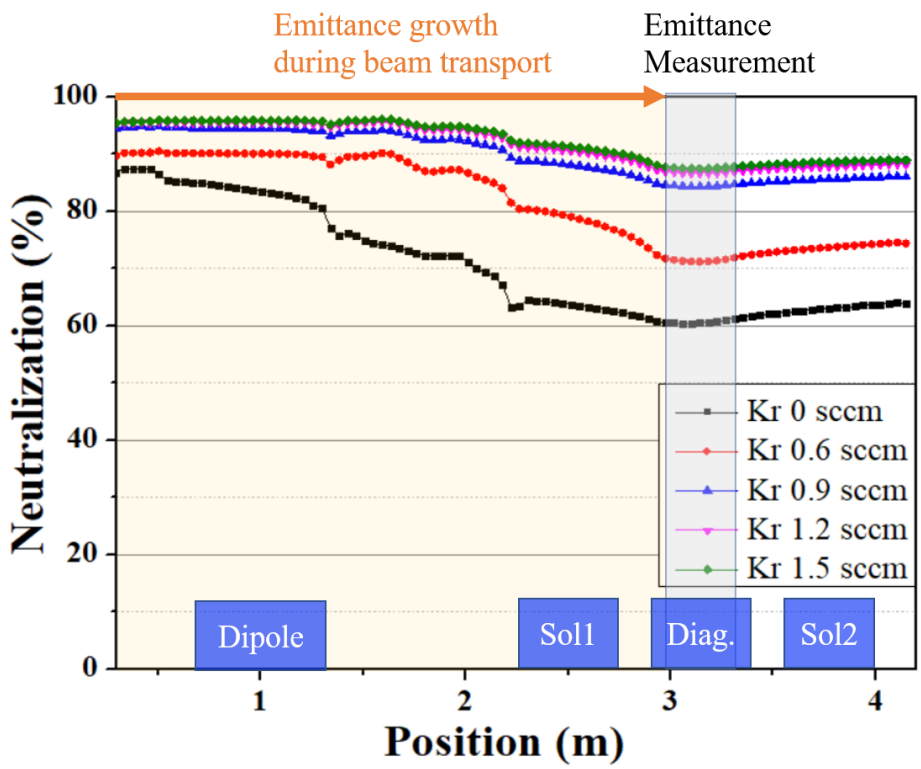

Figure 4. 7. Calculated distribution of neutralization factor depending on krypton gas flow rate in low energy beam transport line in the proton injector test stand.

Neutralization map as shown in Figure 4.7 can be obtained by

substituting the gas pressure distribution and the beam envelope calculated from beam dynamics simulation into equation (4.5). Since the cross-section differs depending on the type of gas, in this case, hydrogen and Krypton should be calculated separately and the neutralized potential should be summed.

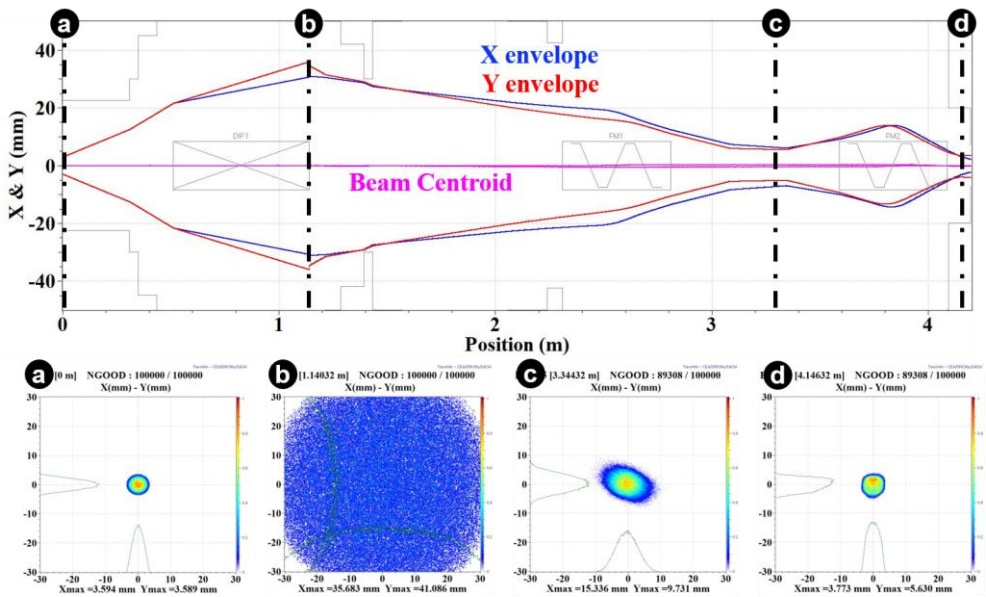

Figure 4. 8. Beam dynamics simulation with neutralization factor in the low energy beam transport system.

Figure 4.8 shows the calculation of the beam center and beam envelope using beam dynamics simulation. Realistic model on neutralization factor may produce accurate beam dynamics simulation results. The distribution of the neutralization factor is obtained with the analytic formula for the space charge potential and the gas density distribution obtained by numerically calculating the vacuum system. For more accurate calculation, the neutralization factor is updated with the beam size data obtained from the beam dynamics simulation, and the beam dynamics simulation is performed again. This process is repeated until the

neutralization factor converges.

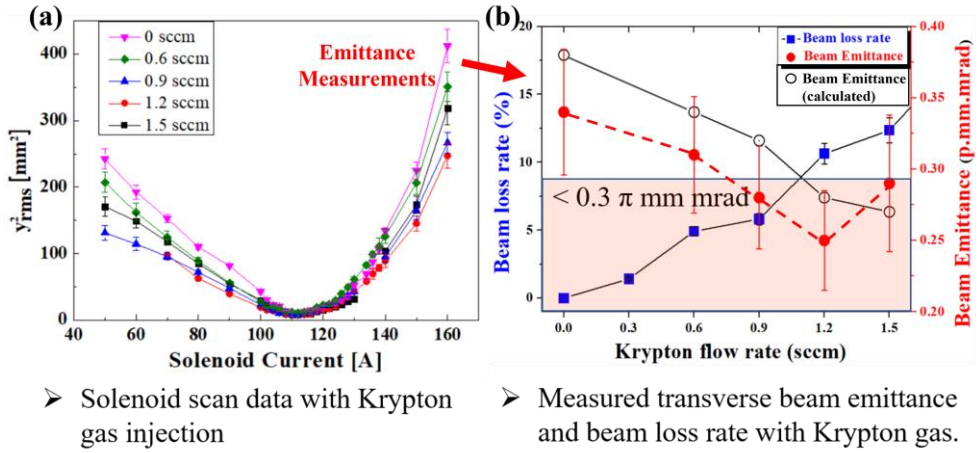

➢ Solenoid scan data with Krypton gas injection

➢ Measured transverse beam emittance and beam loss rate with Krypton gas.

Figure 4. 9. (a) Beam profile change during solenoid scan with different krypton gas flow rate and (b) comparison measured beam emittance to calculated emittance.

Figure 4.9 (a) is the data of measuring the change in beam size using a scintillation screen in a solenoid scan experiment for several Krypton gas flow rates. As the Krypton gas flow rate increases, the overall beam size tends to decrease due to the enhanced space charge neutralization.

By substituting the solenoid scan data into equation (4.26) and performing regression analysis, the transverse beam emittance can be obtained. Figure 4.9 (b) compares the measured beam emittance according to the krypton gas flow rate, the measured beam loss rate, and the beam emittance calculated by beam dynamics simulation. As the Krypton gas flow rate increases, the beam emittance decreases and the beam loss rate tends to increase. This explains the phenomenon that the self-neutralization effect is enhanced by Krypton gas injection, and the emittance growth is suppressed as the neutralization factor increases.

However, in the experiment, when more Krypton gas than 1.2 sccm

is injected, the beam emittance is rather increased. This can be explained by the side effects of increasing beam emittance while increasing halo formation as beam loss due to gas scattering occurs. Therefore, the optimal gas injection scheme experimentally found in terms of suppressing emittance growth is to inject 1.2 sccm of Krypton gas between the bending magnet and the LEBT diagnostics chamber.

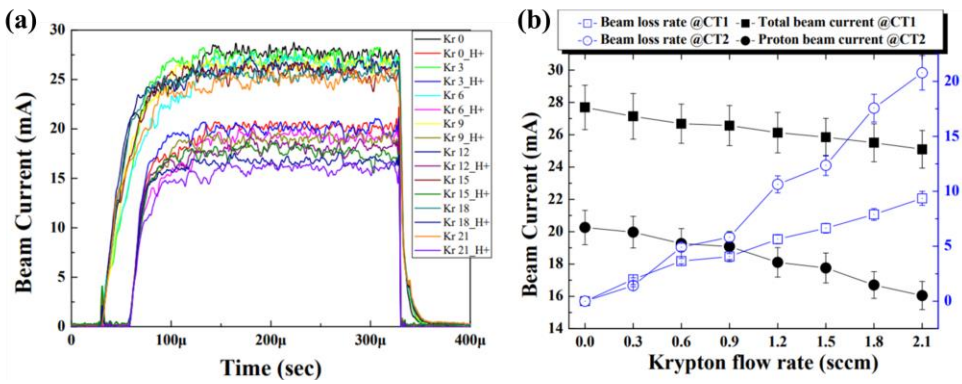

Figure 4. 10. Beam losses with different krypton gas flow rate.

Quantitative experimental data for beam loss is shown in Figure 4.9. The beam current is measured in CT#1 before the bending magnet and CT#2 after the bending magnet. What is measured in CT#1 is a total beam current that combines $H^+, H_2^+,$ and H_3^+ and what is measured in CT#2 is only proton beam current. Figure 4.10 (a) shows the raw waveforms of measured beam current at the CT#1 and CT#2 according to the Krypton gas flow rate for a beam pulse of 300 μs in one graph.

According to Figure 4.10 (b), when Krypton is not injected (0 sccm), the averaged total beam current in CT#1 is 27.7±1.4 mA, and the averaged proton beam current in CT#2 is 20.1±1.1 mA. By measuring the beam current, it can be seen the change in the beam loss rate as Krypton is added at intervals of 0.3 sccm from 0 sccm to 2.1 sccm. When maximum 2.1 sccm

is injected, CT#1 before the bending magnet shows a beam loss rate of 9.2± 0.7%, and CT#2 after the bending magnet shows a beam loss rate of 21.3± 2.5%. This result implies that beam loss rates of 6.9% and 12.4% or more are measured in CT#1 and CT#2, respectively, and rather increases the emittance when the Krypton flow rate is 1.5 sccm or more.

Chapter 5. Tuning of the Beam Parameters by Artificial Neural Network Model

In order to study the beam dynamics in a high-intensity proton injector, it is necessary to know several variables and operating values. But there are several unknowns that are difficult to measure and even out of control. Beam tuning and control is required to transport the beam to the right position, to the right size, i.e. with the right beam parameters for subsequent RF accelerator.

5.1. Beam Dynamics Simulations: Training Data Preparation

Beam dynamics of the proton injector test stand is numerically modeled in *TraceWin* code [29]. There are some essential input beam parameters - such as beam emittance, Twiss parameters, beam current and beam energy – to run the simulation. Table 5. 1 describes typical beam parameters measured in the previous study [50]. On the other hand, some parameters are tough to be exactly measured - such as a beam centroid offset at the extraction region and a tilt at the magnetic elements due to misalignment, and spatial distribution of space charge compensation, even though they have a great impact on beam transport in LEBT. Assuming the unknown parameters as reasonable values, the code calculates a beam trajectory and an envelope by solving beam matrix with a second order momentum or a macro particle distribution.

Table 5.1. Initial beam parameters used in beam dynamics simulation.

Parameter	Value
Normalized r.m.s. beam emittance	0.2 π mm·mrad
Twiss parameters	α=0, β= 0.1125 mm/π·mrad
Beam current	Total: 30 mA $H^+ : H_2^+ : H_3^+ = 80 : 20 : 1$
Beam energy	50 keV

In the proton injector, an initial beam with errors goes through the bending magnet as the first magnetic element, and then passes two steerers at z=1.5 m and z=2.15 m. This off-axis beam finally passes the solenoid magnet, and experiences rotation and focusing due to the azimuthal momentum induced by the fringe field effect nearby the entrance and the exit of the magnet.

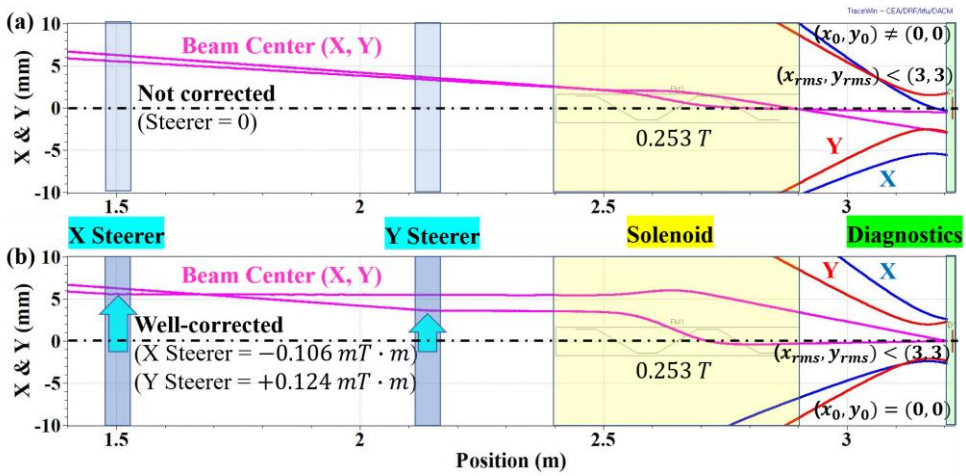

Figure 5. 1. Calculated beam centroid (X&Y: magenta) and r.m.s. envelope (X: blue, Y: red) by TraceWin code at the specific input parameters: (a) Not corrected as no steerer power, (b) Automatically corrected with adjusted steerer power to satisfy beam parameters (size and centroid) desired at the beam diagnostics [51].

Without any orbital correction along the beamline, this beam eventually arrives at a wrong or off-center position. The beam dynamics code can simulate auto-tuning process by means of adjustable elements and diagnostics elements, to correct the beam. The strengths of the solenoid and steerers are adjusted for the desired beam properties at the beam diagnostics and the results are depicted in Table 5.2 and Figure 5.1.

Table 5.2. Input parameters and output parameters with desired values and adjusted values.

Input Parameters	**Input Values**	**Output Parameters**	**Output Values**
Initial beam centroid angle (X', Y')	(10, 10) [mrad]	*Desired* Beam Size	(X_rms, Y_rms) < (3, 3) [mm]
Space Charge Compensation Factor	Extraction region = 40% LEBT region = 90%	*Desired* Beam Position	(X, Y) < (0.1, 0.1) [mm]
Initial beam offset (X, Y)	(0, 0)	*Adjusted* LEBT Solenoid Strength	115 [A] ~ 0.253 [T]
Tilt of solenoid magnet (XZ, YZ)	(0, 0)	*Adjusted* LEBT Steerer Strength	Horizontal: -0.106 Vertical: +0.124 [mT·m]

It is, however, almost impossible to reconstruct the realistic beam dynamics by a few number of calculations because there should be many assumptions. It is believed that the artificial neural network (ANN) model trained by huge datasets is capable to analyze the correlation between beam control variables and beam transport no matter how affecting unknown parameters are, when assisted by effective beam diagnostic data. To verify the assumption and develop good ANN model, extensive beam dynamics calculations are conducted with input parameters summarized in Table 5.3 [51].

Table 5.3. Input parameters and scanned values of the beam dynamics simulations for the mass production of training data [51].

Six Unknown and Three Adjustable Parameters	Scanned Input Values	Number of Cases
X' initial beam centroid angle	-20, -15, -10, -5, 0, +5, +10, +15, +20 [mrad]	9
Y' initial beam centroid angle	0, +5, +10, +15, +20 [mrad]	5
X Initial beam centroid offset	0, +2, +4 [mm]	3
Space charge compensation	80%, 85%, 90%, 95%	4
XZ tilt in Solenoid	-1, 0, 1 [deg]	3
YZ tilt in Solenoid	-1, 0, 1 [deg]	3
LEBT solenoid#1 strength	110, 115, 120 [A]	3
Horizontal X steerer strength	-0.6, -0.4, -0.2, 0, +0.2, +0.4, +0.6 [mT·m]	7
Vertical Y steerer strength	-0.6, -0.4, -0.2, 0, +0.2, +0.4, +0.6 [mT·m]	7

The range of input variables is chosen within the system constraints so that it is assumed that beam is a circular or elliptical shaped in transverse space without beam loss. The number of cases is decided within available computing resource. Vertical tilt of initial beam centroid is assumed as the only one direction since the proton injector is symmetric about the y-axis. Horizontal tilt and offset are all included in both direction because there is bending magnet in the XZ plane between the ion source and LEBT solenoid. Space charge compensation factor is typically from 80% to 95% in the magnetostatic LEBT maintained by residual hydrogen gases diffused from an ion source. Another critical error source, tilt of solenoid magnet, is also considered as nine different cases. The major output variables in interest are beam sizes and centroid positions at the beam diagnostics plane. To sum up,

nine different input parameters are scanned to see how four output values are affected.

5.2. Artificial Neural Network Model for the Fast Beam tuning

The advantage of machine learning is that it enables good regression analysis for nonlinear systems and discovers patterns in conjunction with actual machine data [35]. Even if any unknown parameter exists, it is required that beam control elements can be optimized, thereby the beam matching condition can be reached. To facilitate this objective, a multi-layer perceptron model is applied. The training and validation are carried out with the extensive beam dynamics calculation datasets.

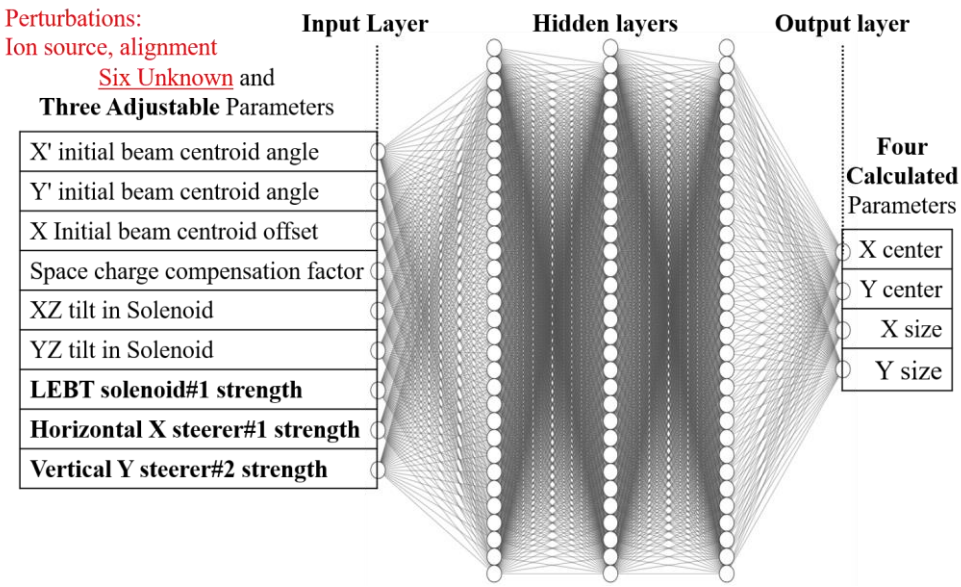

Figure 5. 2. The layout of the artificial neural network model for the proton injector test stand with beam dynamics simulation.

The total number of cases is 714,420 datasets in which 80% of the datasets is randomly extracted and put into training and the remaining 20% is used as test datasets. As demonstrated in Figure 5.2, input layer consists of nine variables input to the beam dynamics code, and output layer is composed of four variables as beam size and beam centroid position estimated at the beam profile monitor. This is a fully-connected feedforward neural network in which the input layer is connected to a dense layer consisting of several nodes, respectively, through the *ReLu* activation function and mean square error (MSE) as loss function [51].

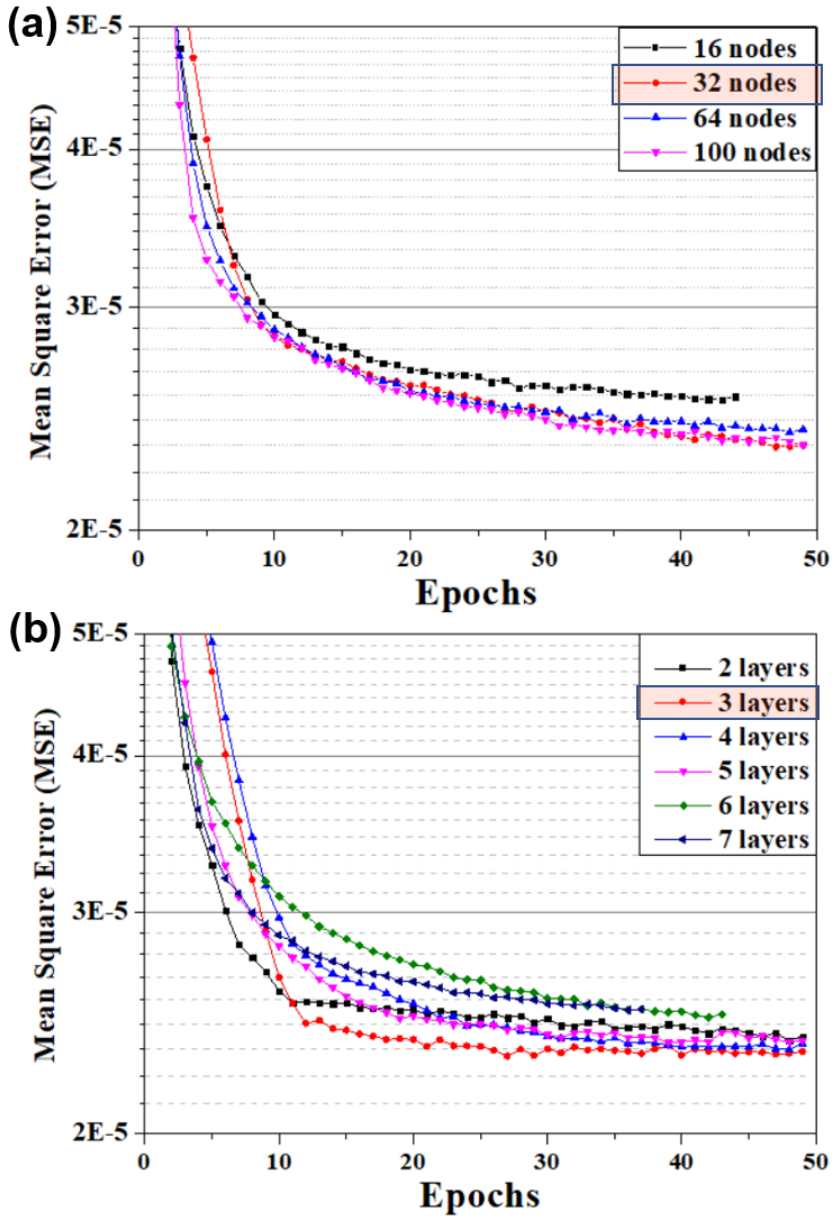

Figure 5. 3. Tuning of hyperparameters: (a) the number of nodes and (b) the number of layers.

Hyperparameter is a special constant to be set before the learning process begins. Hyperparameters are initially defined and not changed during the learning process. Hyperparameters include the number of nodes,

choice of activation function, loss function, optimizer, learning rate, and the number of epochs.

$$MSE = \sum_{i=1}^{n} \left(y_i - y_i^p\right)^2 / n \tag{5.1}$$

$$\theta_{t+1} = \theta_t - \frac{\eta}{\sqrt{\hat{v}_t + \epsilon}} \hat{m}_t \tag{5.2}$$

Mean square error (MSE) as in equation (5.1) is used as the loss function, and adaptive moment estimation (Adam) as in equation (5.2) is used as the optimizer. The learning rate was set to 0.0001 for the Adam optimizer to be a model with maximum performance within the limits of physical computing resources such as memory capacity and learning hours.

In order to optimize the performance of the artificial neural network (ANN) model, it is necessary to properly tune the hyperparameters. Among them, tuning is performed on the number of nodes and the number of layers that can be quantitatively evaluated. Figure 5.4 (a) shows the training history when the number of nodes assigned to each layer is changed while fixing other hyperparameters except for nodes. Figure 5.4 (b) shows the training history when only the number of layers is changed. As a result, it shows that it converges to the lowest prediction error within 50 epochs with 3 layers and 32 nodes each.

It takes short time to train this simple model, so the difference is negligible between stochastic gradient descent method and the other fast optimizers such as RMSprop and Adam. In addition, early-stop at 50 epochs seems sufficient, but training is to be done up to 200 epochs without the callback function because there is no tendency to overfit as appeared in Figure 5.5.

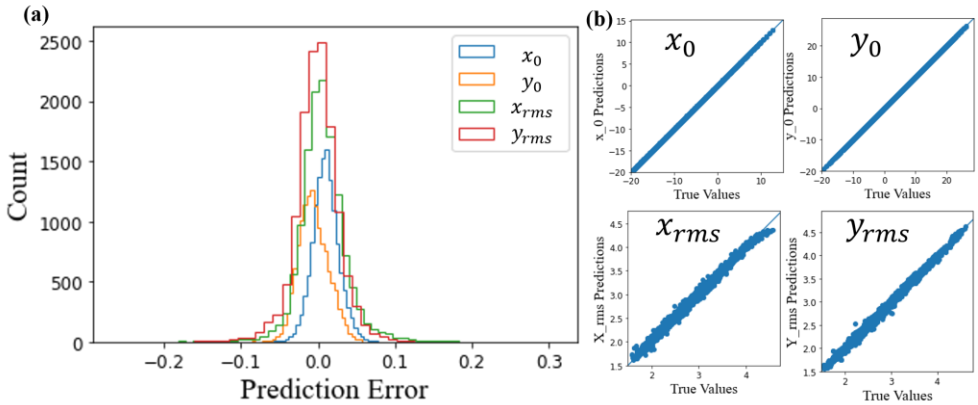

Figure 5. 4. (a) The distribution of prediction error, (b) Testing comparison of predicted values to test values.

The prediction values have good correlation with true values as illustrated in Figure 5. 4 (b). The prediction error, which expresses the difference between the test dataset and the predicted data, has a Gaussian distribution with a center close to zero and a full-width at half-maximum of less than 0.1 in Figure 5. 4 (a).

The same optimization problem, above mentioned in Table 5.2., is solved to validate an accuracy and experimental feasibility of the model. Beam dynamics code solves this problem by an iterative way, but the model does the regression problem directly by using trained patterns.

Table 5. 4. An example of comparison of beam tuning between neural network model and beam dynamics simulation.

	Computation Time	Steerer [mT·m]		Beam Centroid [mm]		Beam Size [mm]	
		X	Y	X	Y	X	Y
Neural Network	Immediately (~ 0 sec)	-0.105	0.124	-0.023	0.011	2.60	2.30
Beam Dynamics Code	Several times of one set (1~100 sec)	-0.106	0.124	0.000	0.000	2.64	2.33
Difference in percent		1.0%	0.0%	2.3% / (1 mm)	1.1% / (1 mm)	1.5%	1.3%

Table 5.4. shows the comparison of beam tuning results obtained by the model to the ones calculated by the beam dynamics code. The artificial neural network (ANN) model reconstructs nearly the same results with the beam dynamics ones. Furthermore, the ANN model immediately finds the solution in less than a second, even if it takes another long time to train the model. The results imply that an initial cost to train the beam dynamics model may be rewarded by saving the time to solve new optimization problem in a long term.

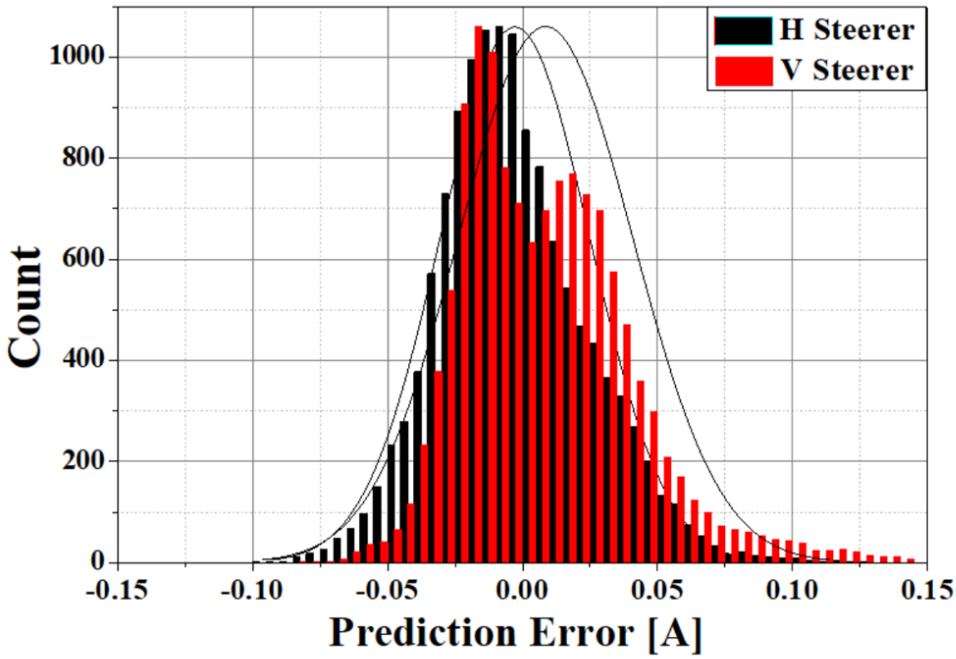

✓ (H, V) Steerer Error = (-0.03±0.03 A, 0.01±0.03 A)

Figure 5. 5. Prediction error of beam dynamic simulation-based artificial neural network model.

A huge number of labeled data obtained by beam dynamics simulation is trained on an ANN model, and prediction error is used to evaluate the performance of this model. Prediction error is defined as the difference between the output label already known as the correct answer and the prediction result when only the input is given to the ANN model. Prediction error tends to follow a gaussian distribution statistically by the law of large numbers, so the closer the mean and standard deviation are to 0, the more predictive the ANN model can be.

The performance of predicting the steerer value in the ANN model trained with about 700,000 beam dynamics simulation data is -0.03±0.03 A and 0.01±0.03 A.

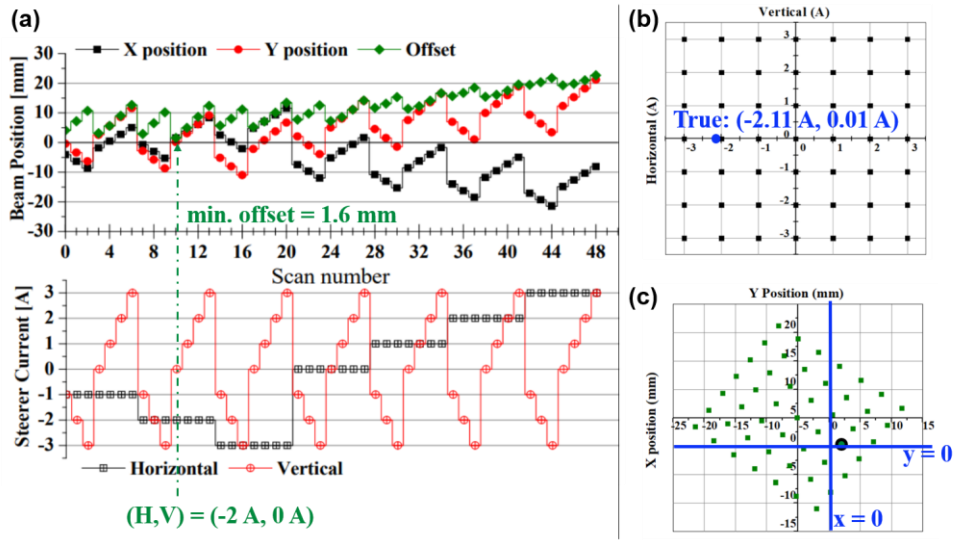

Figure 5. 6. An example of parametric scan with beam dynamic simulation: (a) steerer current scan vs. beam position, (b) scanned steerer current values, (c) calculated beam positions during the steerer scan.

Figure 5.6 (a) is an example of graphing the change in beam position and offset according to the change in the current value of the steerer when parametric scan is performed in the beam dynamics simulation. Figure 5.6 (b) shows the scanned steerer current values as dots in the two-dimensional coordinate system. The H steerer that applied the force in the horizontal direction to the beam was adjusted at 0.5 A intervals from -3 A to +3 A, and the V steerer in the vertical direction was adjusted at 0.5 A intervals from -3 A to +3 A for a total of (7 x 7 = 49) scans are performed. The beam positions measured from these steerer settings are shown in Figure. 5.6 (c). Here, the minimum offset, which is the closest distance from the center of the transverse plane, is 1.6 mm when the current of the horizontal steerer is -2 A and the current of the vertical steerer is 0 A.

5.3. Experimental Validation and Application on Beam Control Experiment

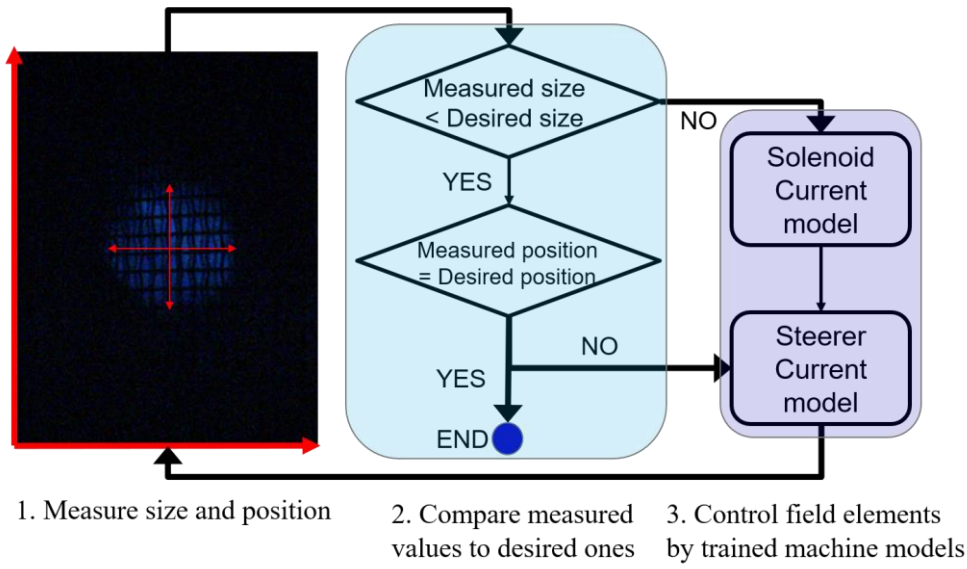

Figure 5. 7. Control workflow for the experimental utility of artificial neural network model.

For the experimental utility of the model and the methodology, we suggest a control workflow in the proton injector, to be validated in future application, as configured in Figure 5.7. The first step is to measure the beam parameters – beam size and beam position in this model. The measured data feed into the model to check if it is satisfying the desired beam parameters. In the stage, beam diagnostics data and operating parameters are stored and trained to the model. As a result of the solenoid and steerer model, the control variables are properly tuned.

This workflow is implemented by EPICS and its interface library - PyEpics and PyQt – and to be applied as an auto-tuning method in machine operation. Experimental data from beam diagnostics and control variable is

automatically acquired by EPICS based system, and finally the experiment-based ANN model performs well for fast optimization of beam parameters at the diagnostics plane.

Since the artificial neural network model proves that the beam offset is approximately proportional to the steerer current, when other variables are all fixed, the only things we want to know is kicking angle and strength over a unit magnetic force. These variables are closely related to the beam characteristics and the strength of beam focusing elements downstream. If this off-axis rotation through magnetic element is measured and the data is accumulated enough, the automatic tuning is to be faster than the previous one up to a beam monitoring frequency.

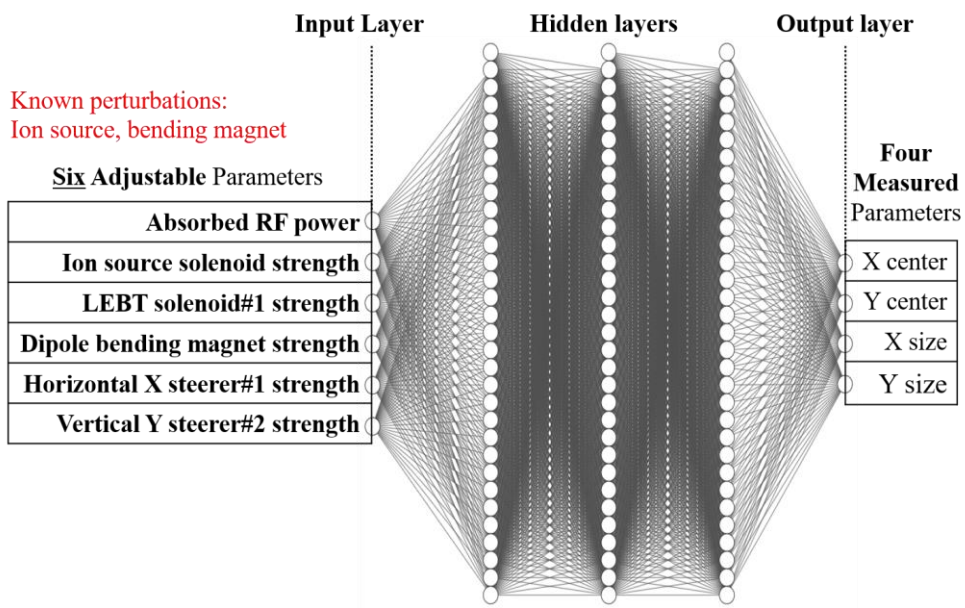

Figure 5. 8. The layout of the artificial neural network model for the proton injector test stand with experiments.

In order to perform beam tuning using an artificial neural network model in beam experiments, the layout was configured as shown in Figure

5.8. When operating an ion source, there are two control parameters that can be adjusted: absorbed RF power and solenoid strength. In addition, there are four control parameters that can be adjusted in low energy beam transport (LEBT) operation: LEBT solenoid#1 magnet strength, dipole bending magnet strength, horizontal steerer strength, and vertical steerer strength. According to these control variables, data measured on the beam profile downstream of the LEBT solenoid#1 are collected. The captured images can be analyzed by the method introduced in Chapter 3.3 to obtain the beam center and beam size, and these values are assigned as labels to the output layer and used to train the ANN model.

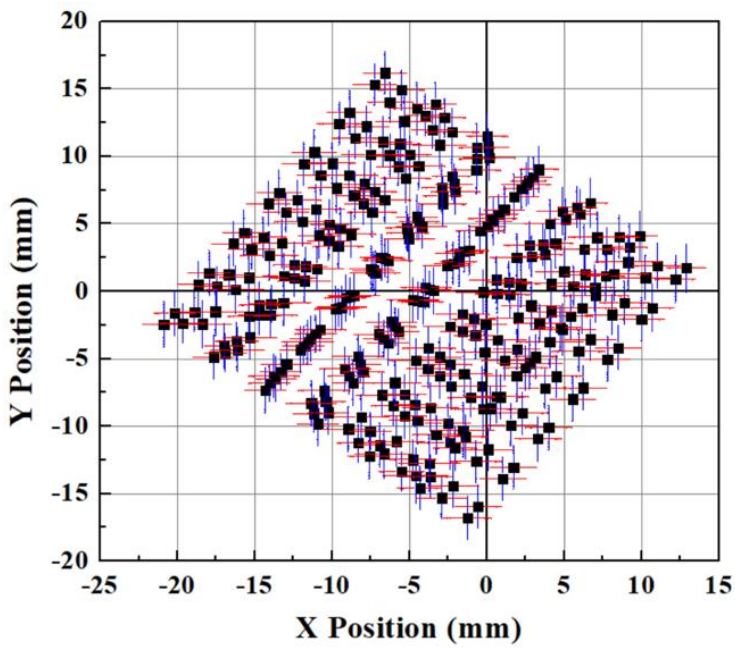

Figure 5. 9. Parametric scan data for the training of experimental

data-based artificial neural network model.

Figure 5.9 shows the measurement result of the beam position measured by the beam profile monitor along with the error bar according to various experimental conditions.

The control parameters are the RF power of the ion source, and the beam solenoid magnet, bending magnet, and steering magnets (steerers), which are operating parameters of low energy beam transport (LEBT). The property of the control variable and the rate of change determine the change in the beam position. In order to make a more accurate ANN model, more labeled data should be acquired and applied to model training.

In actual machine control, an operator is subject to unknown physics and parameters, which make hard to employ traditional beam dynamics code as an automated optimization tool. The operator generally puts the present setting values and measured beam data on the code, or the data are done automatically by some programs, in a repetitive way. This process may have slowly improved results, but lessons are not probably learned. On the contrary, an ANN model-based system is more flexible to accumulate all the on-line monitoring data and to find meaningful patterns or formula hidden in large parameter spaces. The *trained* experience may be utilized for the fast optimization whenever the beam condition changes in a periodic way or not. The artificial neural network model we presents is trained and validated by these extensive sets of calculation, where the model has good prediction to the changes within pre-defined parameters. This model provides initial solution for patterning how a beam reacts to unknown variables and controllable elements such as solenoid and steerer.

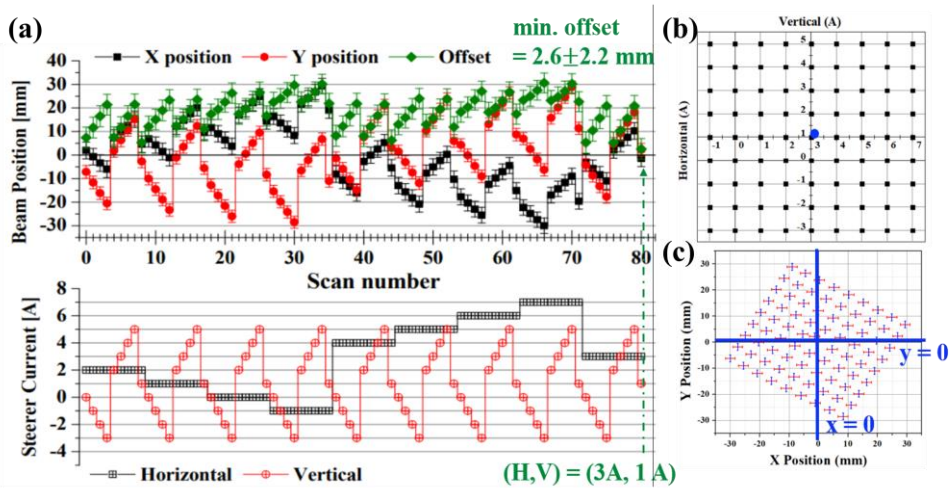

Figure 5. 10. An example of parametric scan with experimental data: (a) steerer current scan vs. beam position, (b) scanned steerer current values, (c) measured beam positions with statistical error during the steerer scan.

Figure 5.10 (a) is an example showing the position and offset of the beam according to the change in the current value of the steerer when parametric scan is performed in beam tuning experiments. Figure 5.10 (b) shows the steerer current values used in the scan experiment as dots on the X-Y coordinates. The so-called H-steerer that applied the force in the horizontal direction to the beam was adjusted at 1 A intervals from -1 A to 7 A, and the so-called V-steerer in the vertical direction was adjusted at 1 A intervals from -3 A to 5 A. The beam positions measured from the steerer scan for a total of 9 × 9 = 81 cases are shown in Figure 5.11 (c). The minimum offset, which is the closest distance from the center of the transverse plane, is 2.6±2.2 mm when the current of the H-steerer is 3 A and the current of the V-steerer is 1 A.

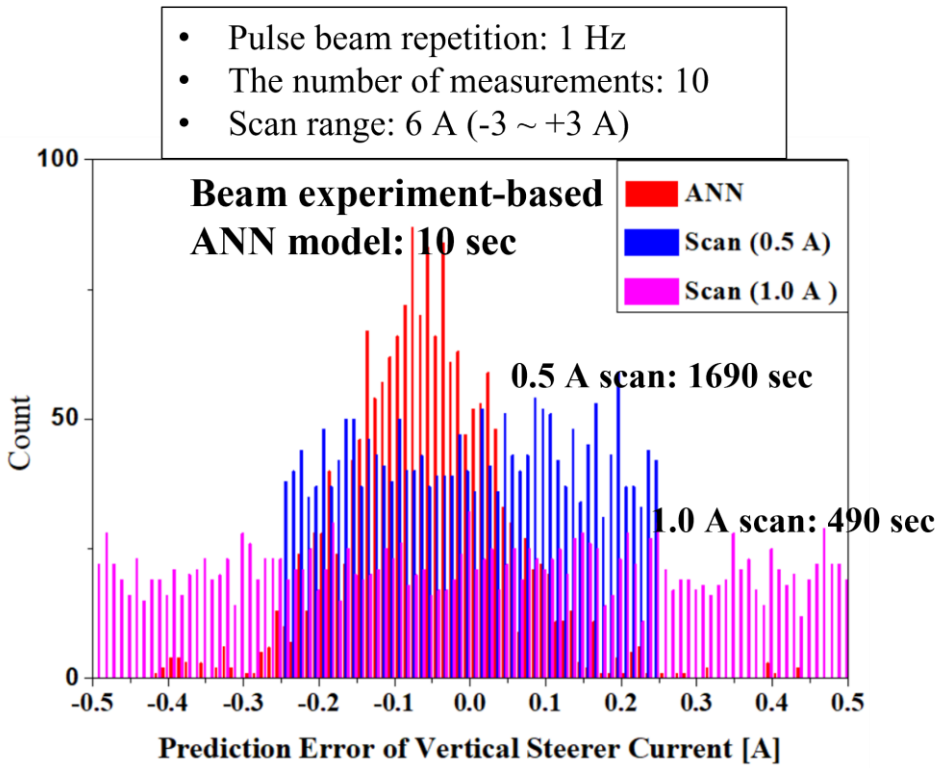

Figure 5. 11. Comparison of ANN model to parametric scan in terms of prediction error distribution and tuning time.

Figure 5.11 compares the performance of the methods using the ANN model to using parametric scan in the steerer tuning experiment.

The performance is compared in terms of prediction error of steerer current value and in terms of time consumed. First, the ANN model shows a prediction error distribution close to the gaussian model, and the mean and standard deviation for H-steerer and V-steerer are (-0.05±0.10 A, -0.06±0.10 A). On the other hand, in the case of the parametric scan method, it showed a relatively uniform error distribution from -0.25 A to +0.25 A at the 0.5 A interval, and a relatively flat error distribution from -0.5 A to +0.5 A at the 1.0 A interval.

The measurement was repeated 10 times under one operating condition, and the pulse beam repetition rate was 1 Hz. It takes 10 seconds to obtain the beam position information and prediction error derived from the ANN model. On the other hand, when scanning current values from -3 A to +3 A for two steerer magnets, it takes 1690 sec at 0.5 A interval and 490 sec at 1.0 A interval.

Combining and comparing the above results, the ANN model produces more accurate results in terms of prediction error compared to the parametric scan method, and has a 49 times faster tuning speed.

Chapter 6. Conclusion and Future Work

6.1. Conclusive Summary of the Study

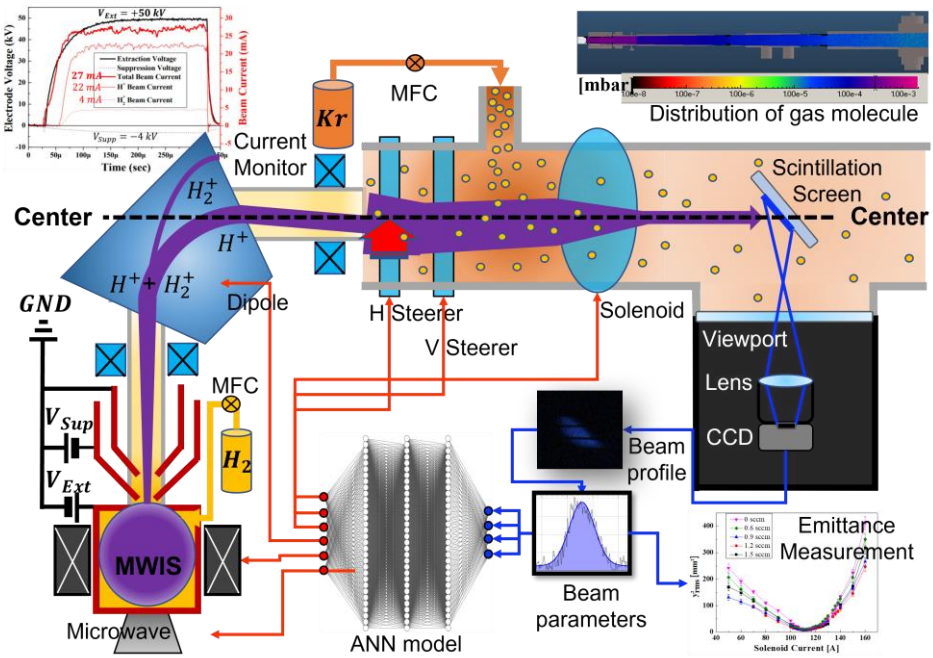

Figure 6. 1. Overview of the study in the proton injector test stand: Firstly, numerical analysis and injection technique on residual gas. Secondly, artificial neural network (ANN) model for systematic beam tuning.

Two aspects were studied to improve low-energy beam transport. Firstly, the self-neutralization phenomenon by residual gas is used to cancel the strong space charge effect. Residual gas can promote self-neutralization by causing ionization, and conversely, it can cause charge exchange to blow beam quality through beam loss and halo formation. To optimize the self-neutralization regime with gas injection, a space charge neutralization model for a steady-state proton beam is established and calculated. A vacuum

system is designed and installed to lower the partial pressure of hydrogen and increase the partial pressure of krypton, and numerical analysis is performed on gas molecules. Based on the results and beam dynamics analysis, the neutralization factor is derived along the low energy beam transport line, which is more quantitative than the one using single gas pressure in previous studies [12, 52]. The emittance growth is estimated in beam dynamics simulation with space charge model.

Beam emittance measurements in the low energy beam transport section are performed using a scintillating screen-based beam profile monitor and a solenoid scan method. Numerical results and measurement results showed similar trends, but the beam emittance rather increased when krypton was injected over 1.5 sccm. This can be partially explained by the beam loss rate measured by the beam current monitor. It is presumed that this is due to the adverse effect of increasing halo formation as beam losses increase.

With novel approach to obtain the distribution of space charge neutralization by applying gas pressure distribution, emittance growth and its suppression by additional gas injection are well explained numerically and experimentally. Beam emittance growth is successfully suppressed lower than 0.3 π mm mrad, meeting RFQ matching requirement.

Secondly, another aspect to improve proton injector is an accurate and fast tuning method. In general, beam current is used as an index to evaluate beam matching between low energy beam transport and RF accelerator. However, the transmission ratio of beam current is only a direct result of matching. In order to analyze the process and the factors of mismatch and to improve low energy beam transport, it is necessary to measure and optimize beam parameters. That is, for beam matching, not only low emittance, but also Twiss parameters and beam center must satisfy the input requirements of the RF accelerator. A beam profile monitor is used

to measure beam size and position as beam parameters. An artificial neural network (ANN) model is developed and applied to predict the set values of magnets required for optimizing beam parameters according to the change of conditions of the ion source extraction system and low energy beamline.

In the beam dynamics simulation, some error factors are introduced as input variables, and the data generation process for calculating beam parameters according to the strength of control magnets is performed for a combination of many input variables. In order to make a high-accuracy prediction model with the generated large dataset, hyperparameters are tuned, and the performance of the ANN model is evaluated through statistics on prediction error.

To compare the performance with the existing parametric scan, the ANN model is compared in terms of prediction error distribution and tuning speed, respectively. ANN model based on beam experimental data produces more accurate results in terms of prediction error compared to the parametric scan method, and shows 49 times faster tuning speed.

ANN-based beam tuning method reflecting operation conditions, such as RF power and magnet strength, was developed from beam dynamics simulation and beam experiment data, and it was applied to overcome the inefficiency and the inaccuracy of traditional parametric scan method in low energy beam transport. With the features of fast response time and the enhanced accuracy, the developed method can be expanded by using various beam diagnostic data from the accelerator and utilized as a framework for autonomous operation with minimum intervention of the operator.

6.2. Conclusive Summary of the Study

The study can serve as basis for systematic analysis on space charge neutralization and more accurate beam behavior prediction in the downstream. The emittance growth suppression technique through residual gas injection can also be applied to other proton injectors like 100-MeV linear accelerator in the KOMAC. Since radio-frequency quadrupole requires ultra-high vacuum, and the ion source must maintain the purity of hydrogen, it is necessary to design an appropriate residual gas pressure distribution through numerical analysis for gas molecules. We propose a method to form a high partial pressure only during beam extraction by injecting residual gas through the pulse valve. Other common methods are conductance control through orifice structures, differential pumping, etc., which can be aided by the numerical analysis on gas molecules.

On the other hand, besides suppressing emittance growth, it is also necessary to study the design of the ion source and extraction system that makes the initial emittance low. In this study, low energy beam transport was studied under the extraction conditions of a beam with low emittance and small divergence passing through a dipole bending magnet. As a follow-up study, it is necessary to design an upgrade method such as a five electrode system and double solenoid magnets to obtain an initially low emittance beam, and to study the optimal conditions by extensively performing an emittance scan downstream of the ion source.

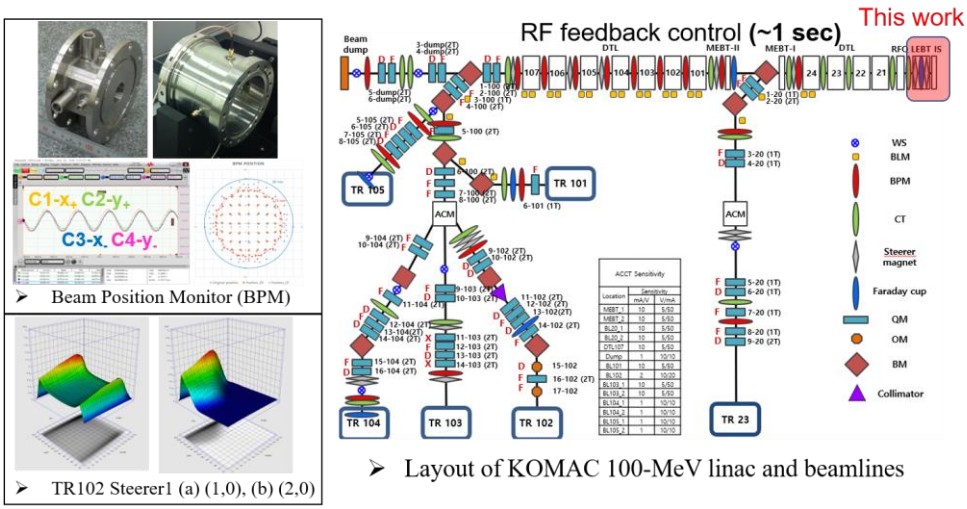

Figure 6. 2. The layout of beam diagnostics and beamline in the KOMAC.

Deep learning is expected to be nicely applied in high energy beamlines as well as low energy section. There are many beam position monitors around the drift tubes of the linear accelerator and other beamline components. To minimize beam loss in beam transport, the relationship between these diagnostics and the electromagnetic elements controlling the beam must be quantified and actively exploited as a feedback control method. Another application case is TR102 target room, where large-area-low-dose beam irradiation experiments are conducted in the KOMAC. It is necessary to quickly and precisely prepare a beam that meets requirements of users. It can be seen in Figure 6. 1 that changing the steerer strength near the TR102 changes the dose distribution. However, there are numerous electromagnets before the steerer, and the beam condition may change irregularly depending on the state of the accelerator. These beam tuning challenges may be more complex than low energy beam transport, finding optimal solutions in a wider parameter space. Therefore, future works will be dedicated to expand the systematic tuning method developed in the study to wider applications in the field of accelerator control.

Bibliography

[1] The European Technical Working Group on ADS, “A European Roadmap for Developing Accelerator Driven Systems (ADS) for Nuclear Waste Incineration”, ENEA, (2001)

[2] A. Chance, N. Chauvin, and R. Duperrier, “THE SOLMAXP CODE”, *Proceedings of 3rd* International Particle Accelerator Conference (New Orleans, Louisiana, USA, 2012)

[3] A. BenIsmail, R. Duperrier, D. Uriot, and N. Pichoff, “Space charge compensation studies of hydrogen ion beams in a drift section”, *Physical Review Special Topics – Accelerators and Beams* **10**, 070101 (2007)

[4] A. L. Edelen, S. G. Biedron, B.E. Chase, D. Edstrom, S.V. Milton, and P. Stabile, “Neural Networks for Modeling and Control of Particle Accelerators” IEEE *Transaction on Nuclear Science* **63**, 2 (2016)

[5] D. De Bruyn, H. Ait Abderrahim, P. Baeten, and P. Leysen, “The MYRRHA ADS Project in Belgium Enters the Front End Engineering Phase”, NEA/NSC/R (2015)2

[6] H. Podlech, K. Kumpel, C. Lorey, P. Schneider, N. Petry, A. Schempp, C. Zhang, and A. Bechtold, “The MYRRHA-RFQ – Status and First Measurements”, *8th Proceeding of International Particle Accelerator Conference* (Copenhagen, Denmark, 2017)

[7] J. Knaster et al., “Overview of the IFMIF/EVEDA project”, *Nuclear Fusion* **57**, 102016 (2017)

[8] R. C. Baumann, “Radiation-induced soft errors in advanced semiconductor technologies”, *IEEE Transactions on Device and Materials Reliability* **5** (2005) 305-316

[9] JESD89A, “Measurement and Reporting of Alpha Particle and Terrestrial Cosmic Ray-Induced Soft Errors in Semiconductor Devices”, JEDEC (2006)

[10] Dario Bisello, Andrea Candelori, Natalia Dzysiuk, Juan Esposito, “Neutron production targets for a new Single Event Effects facility at the 70 MeV Cyclotron of LNL-INFN”, Physics Procedia **26** (2012) 284-293

[11] E. W. Blackmore, “Improved Capabilities for Proton and Neutron Irradiations at TRIUMF”, *IEEE Radiation Effects Data Workshop* (Monterey, CA, USA, 2003)

[12] N. Chauvin, O. Delferriere, R. Duperrier, R. Gobin, P. A. P. Nghiem, and D. Uriot, “Transport of intense ion beams and space charge compensation issues in low energy beam lines", Review of Scientific Instruments **83**, 02B320 (2012).

[13] S. Artikova, K. Ikegami, T. Shibata, and A. Takagi, “Space Charge Neutralization Studies with H^- Beam in Low Energy Beam Transport Test Stand”, *7th Proceeding of International Particle Accelerator Conference* (Busan, Korea, 2016)

[14] C.A. Valerio-Lizarraga, **“**Emittance growth due to space charge compensation and beam intensity instabilities in negative ion beams”, Physical Review Accelerators and Beams **21,** 030101 (2018)

[15] E. Fol, J. M. Coello de Portugal, and R. Tomas, “Application of Machine Learning to Beam Diagnostics”, *Proceedings of 7th International Beam Instrumentation Conference* (Shanghai, China, 2018).

[16] G. Azzopardi, A. Muscat, G. Valentino, S. Redaelli, and B. Salvachua, **“**Operational results of LHC collimator alignment using machine learning”, *10th International Particle Accelerator Conference* (Melbourne, Australia, 2019)

[17] M. Debongnie, F. Bouly, M. Baylac, T. Junquera, N. Chauvin, D. Uriot, and A. Gatera, “MODELIZATION OF AN INJECTOR WITH MACHINE LEARNING”, *10th International Particle Accelerator Conference* (Melbourne, Australia, 2019)

[18] Y. S. Cho, H. J. Kwon, J. H. Jang, H. S. Kim, K. T. Seol, D. I. Kim, Y. G. Song, I. S. Hong and Y. H. Kim, “The PEFP 20-MeV Proton Linear Accelerator”, *Journal of the Korean Physical Society* **52** (2008) 721-726

[19] Hyeok-Jung Kwon, Han-Sung Kim, Dae-Il Kim, Ji-Ho Jang and Yong-Sub Cho, “Beam Emittance Measurement and Simulation of the PEFP Front End Accelerator”, *Journal of the Korean Physical Society* **56** (2010) 1998-2001

[20] Mohamed E. Abdelaziz and Ahmed M. Ghander, “A Study of Duoplasmatron Ion Source with an Expansion Cup”, *IEEE Transactions on Nuclear Science* (1967) 46-52

[21] Daniel C. Faircloth, "Ion sources for high-power hadron accelertors",

CAS-CERN Accelerator School: High Power Hadron Machine (2013)

[22] Bernhard Wolf, “Handbook of Ion Sources”, *CRC Press* (1995)

[23] G. Arbique, T. Taylor, M. H. Thrasher, and J. Wills, “Multi-beamlet injection to the RFQ1 accelerator-a comparison of ECR and duoPIGatron proton sources” *IEEE Particle Accelerator Conference* (San Francisco, CA, USA, 1991)

[24] Ian G. Brown, “The Physics and Technology of Ion Sources, Second Edition”, WILEY-VCH (2004).

[25] Z. Q. Xie, “State of the Art of ECR Ion Source”, *Proceedings of the 1997 Particle Accelerator Conference* (Vancouver, BC, Canada, 1997)

[26] Luigi Celona, “Microwave Discharge Ion Sources”, *CAS-CERN Accelerator School : Ion Sources* (2014) 421-441.

[27] O. Tuske, N. Chauvin, O. Delferriere, J. Fils, and Y. Gauthier, “Commissioning of the ECR ion source of the high intensity proton injector of the Facility for Antiproton and Ion Research (FAIR)”, *Review of Scientific Instruments* **89**, 052303 (2018)

[28] Helmut Wiedemann, “Particle Accelerator Physics” Springer (2015) 213-251

[29] D. Uriot and N. Pichoff, “TraceWin manual”, CEA/SACLAY – DRF/Irfu/DACM (2021)

[30] R. Keller, “Ion-Source and Low-Energy Beam-Transport Issues for H- Acclerators”, *Proceedings of the 1999 Particle Accelerator Conference* (New York, USA, 1999)

[31] Prabir K. Roy, “A Multi-Pinhole Faraday cup Device for Measurement of Discrete Charge Distribution of Heavy and Light Ions”, *IEEE Transactions on Nuclear Science*, **63** (2016) 854-860

[32] D. Kim, J. J. Dang, H. J. Kwon, S. H. Lee, H. S. Kim, K. J. Chung, and Y. S. Hwang, “Design and Installation of A Prototype Multi-pinhole Faraday Cup”, *Transactions of the Korean Nuclear Society Virtual Spring Meeting* (2020)

[33] Tom Mitchell, “Machine Learning” McGraw Hill (1997)

[34] Andy Thomas, “An introduction to neural networks for beginners”

[35] E. Fol, R. Tomas, G. Franschetti, and J. Coello de Portugal, “Application of Machine Learning to Beam Diagnostics” *39th Free Electron Laser Conference* (Hamburg, Germany, 2019)

[36] Xiaobiao Huang, Jeff Corbett, James Safranek, Juhao Wu, “An algorithm for online optimization of accelerators”, *Nuclear Instruments and Methods in Physics Research A* **726** (2013) 77-83

[37] M. Mazzaglia ***et al.***, “Improvement of the characterization of the proton source for the European Spallation Source by means of optical emission spectroscopy”, *Physical Review Accelerators and Beams* **22**, 053401 (2019).

[38] Snejana Iordanova and Tsvetelina Paunska, "A collisional radiative model of hydrogen plasma developed for diagnostic purposes of negative ion sources", *Review of Scientific Instruments* **87**, 02B110 (2016)

[39] U. Fantz, H. Falter, P. Franzen, D. Wünderlich, M. Berger, A. Lorenz, W. Kraus, P. McNeely, R. Ried[1] and E. Speth, "Spectroscopy—a powerful diagnostic tool in source development", *Nuclear Fusion* **46**, S297 (2006).

[40] NIST atomic spectroscopy database, http://www.nist.gov/pml/data/asd.cfm

[41] M. Eugene Rudd, Y-K. Kim, D. H. Madison, and J. W. Gallagher, "Electron Production in Proton Collisions: Total Cross Sections", *Reviews of Modern Physics* ***57***, 4 (1985) 965-994

[42] V. S. Nikolaev, "Calculation of the Effective Cross Sections for Proton Charge Exchange in Collisions with Multi-Electron Atoms", *Soviet Physics JETP* **24** (1967) 847-857

[43] B. G. Lindsay and R. F. Stebbings, "Charge transfer cross sections for energetic neutral atom data analysis", Journal of Geophysical Research **110,** A12213 (2005)

[44] M. D. Gabovich, "Ion-beam plasma and the propagation of intense compensated ion beams," Soviet Physics Uspekhi **20** (1977)

[45] I. A. Soloshenko, "Transportation of intensive ion beams," *Review of scientific instruments* **69** (1998) 1359–1366,

[46] D. Winklehner, D. Leitner, D. Cole, G. A. Machicoane, “Space-charge compensation measurements in electron cyclotron resonance ion source low energy beam transport lines with a retarding field analyzer”, *Review of Scientific Instruments* **85**, 02A739 (2014)

[47] R. Kersevan and J.-L. Pons “Introduction to MOLFLOW+: New graphical processing unit-based Monte Carlo code for simulating molecular flows and for calculating angular coefficients in the compute unified device architecture environment”, *Journal of Vacuum Science and Technology A* **27**, 1017 (2009)

[48] Paolo Chiggiato, “Outgassing properties of vacuum materials for particle accelerators”, *Proceedings of the 2017 CERN-Accelerator-School course on Vacuum for Particle Accelerators* (Glumslov, Sweden, 2017)

[49] Anuraag Misra, A. Goswami, P. Sing Babu, S. Srivastava, and V. S. Pandit, “Studies on space charge neutralization and emittance measurement of beam from microwave ion source”, *Review of Scientific Instruments* **86**, 113301 (2015).

[50] Hyeok-Jung Kwon, “Study on the Microwave Ion Source of the 100-MeV Proton Linac”, *Journal of the Korean Physical Society* **69**, 6 (2016) 967-970.

[51] D.H. Kim, S. Lim, K.J. Chung, Y.S. Hwang ***et al.***, "Validation of Neural Network Model Based on Beam Dynamics Simulation for an Automated Control in High-Intensity Proton Injector", *Journal of the Korean Physical Society* **78** (2021) 1185-1190

[52] N. Chauvin ***et al.***, “Deuteron beam commissioning of the linear IFMIF prototype accelerator ion source and low energy beam transport" *Nuclear Fusion* **59**, 106001 (2019).

Abstract in Korean

고출력 양성자 입사기에서 저에너지 빔 수송 향상에 대한 연구

김 동 환
에너지시스템공학부 원자핵공학전공
서울대학교 대학원

고출력 양성자 가속기는 잘 정립된 기술과 연속 운전성을 기반으로 하여 고성능 고속 중성자원 개발에 주로 응용된다. 그 중에서 양성자 입사기는 높은 전류의 빔을 얻기 위한 중요한 기반이다. 이 장치는 이온원에서 형성된 초기 빔을 최소한의 손실로 수송하고, 고주파 사중극과 같은 후속 가속관이 요구하는 입력 빔 파라미터를 정합시키는 역할을 수행한다.

고전류 빔은 비선형적인 전기장 성분을 포함하여 강한 공간 전하 효과를 일으키기 때문에, 수송 과정에서 빔 크기와 에미턴스가 상승하는 문제가 있다. 빔 크기를 줄이기 위해 솔레노이드 집속 렌즈를 이용하는데, 이는 오히려 구면 수차를 일으키며 에미턴스를 보존시키지 못한다. 그리고 전자석과 같은 빔 수송 요소는 수송관의 정렬 오차를 일으킨다. 특히, 솔레노이드 전자석은 빔을 횡방향으로 회전시키는 특성이 있기 때문에 정렬 오차와 더불어 빔 중심 위치 제어를 더욱 어렵게 만든다.

이 연구는 고출력 양성자 입사기의 저에너지 빔 수송 성능 향상을 위한 기법 개발을 목표로 하고, 입사기 시험 시설을 구축한다. 성능 개선을 실험적으로 확인하기 위해 섬광판과 CCD 카메라를 이용한 빔 프로파일 모니터를 주요 진단 장치로 이용한다. 저에너지 빔 수송 성능의 핵심 요소 두 가지는 낮은 빔 에미턴스와 빠르고 정확한 빔 튜닝 방법이다. 이를 위해 잔류 분자 해석 방법과 기계 학습 기법을 각각 도입한다.

첫 번째 결과로, 잔류 분자 해석을 기반으로 한 비활성 기체 주입 기법을 통해 빔 에미턴스 성장을 막아 낮은 빔 에미턴스를 측정한다. 고전류 빔의 높은 공간 전하 포텐셜은 빔이 진행함에 따라 빔 에미턴스를 상승시키는 문제가 있다. 이를 상쇄시키는 자연스러운 과정 중 하나는, 양성자 입사기의 경우 수소 이온원에서 흘러나온 수소 분자와, 미량으로 유입되어 평형을 이루고 있는 공기 분자가 양성자 빔과 충돌하면서 일부 이온화가 진행되고, 발생된 전자가 빔의 공간 전하 퍼텐셜을 상쇄시키는 자기 중성화(self-neutralization)이다. 빔라인의 잔류 기체 분자의 밀도가 일정 수준일 때, 빔 손실 효과에 대비해 최적의 에미턴스 상승 억제 효과를 낼 수 있음을 실험적으로 확인한다. 3 차원 잔류 분자 거동 해석을 통해 빔 수송관에서 수소 분자와 공기 분자의 부분 압력을 낮추고, 비활성 기체 분자의 부분 압력을 높이는 시나리오의 효과를 계산해보고, 실험에서 크립톤 가스 1.2 sccm 주입 시 최대 약 23%의 빔 에미턴스 개선 효과를 얻었다.

두 번째 결과로, 기계 학습 기법 중 인공 신경망 모형을 기반으로 빔 튜닝의 속도와 정확도를 개선하였다. 빔 인출, 집속, 그리고 편향과 같이 빔 수송 과정에 관여되는 요소들 사이에는

측정하기 어려운 정렬 오차 등의 미지수들이 존재한다. 이 오차를 보상해주기 위해 편향 전자석을 사용한다. 이 과정에서 빔 수송을 최적화하기 위해서 여러 전자석 설정 값에 대해 측정되는 빔의 변화 규칙을 관찰하고 그 자료들을 활용할 필요가 있다. 이러한 비선형적인 관계를 측정 자료를 기반으로 해석하기 위해 다층 퍼셉트론 모형을 이용한다. 먼저 예측 모형을 효율적으로 훈련시키고 그 실용성을 대해 검증하기 위해 빔 동역학 기반의 계산을 수행한다. 저에너지 빔 수송계에서 일어날 수 있는 여러 가지 오차 요인과 미지수들의 변화에 따라 특정 위치에서의 빔 크기와 빔 위치를 계산한 결과를 얻는다. 이를 바탕으로 충분한 측정 자료로부터 정확도가 높은 예측 모형을 도출할 수 있음을 확인하고, 실제 빔 진단과 빔 제어 실험에 적용한다. 본 연구에서 개발한 인공신경망 모형은 전자석 값을 일정 간격으로 건너뛰어 설정하며 빔 위치 변화를 측정하는 기존의 스캔 방법에 비해 49 배 이상 빠른 속도로 더 정확한 빔 튜닝 성능을 보인다.

본 연구는 고출력 양성자 입사기의 중요 성능 요소인 빔 에미턴스의 성장 억제와, 빠르고 정확한 빔 수송 제어 기법 개발에 기여하였다. 이것은 가속기 빔 동역학 연구에 빔진단 자료의 활용성을 높여 다양한 조건의 빔라인에서 빔 에미턴스 평가와 향상에 적용시킬 수 있다. 그리고 저에너지 빔 수송 계통보다 제어 변수가 더 많고 복잡한 고에너지 가속단과 빔라인에 확장 적용함으로써 빔 튜닝 효율성을 크게 개선할 가능성이 있다. 궁극적으로는 운전자의 개입을 최소화하는 가속기 자율 운전의 기반 기술로 발전시킬 수 있다.

핵심어: 양성자 입사기, 저에너지 빔 수송, 빔 에미턴스,
자기 중성화, 빔 튜닝, 인공 신경망

학번: 2015-21312